Applications of LaBr$_3$ detectors: Internal fields and g-factor measurements

Timothy J. Gray

A thesis submitted for the degree of
Bachelor of Science with Honours in Physics of
The Australian National University

October, 2016

Declaration

This thesis is an account of research undertaken between February 2016 and October 2016 at The Department of Physics, Faculty of Science, The Australian National University, Canberra, Australia.

Except where acknowledged in the customary manner, the material presented in this thesis is, to the best of my knowledge, original and has not been submitted in whole or part for a degree in any university.

Timothy J. Gray

October, 2016

Abstract

Recent developments have made $LaBr_3$ γ-ray scintillation detectors available. These offer better timing resolution than germanium (HPGe) detectors, but with better energy resolution than scintillators such as Barium Fluoride (BaF_2) and Sodium Iodide (NaI). The combination of excellent time resolution and good energy resolution opens up new research opportunities. One such application is to use $LaBr_3$ detectors for the measurement of the high frequency precessions of short-lived isomers in strong internal fields, in beam, using Time Differential Perturbed Angular Distribution (TDPAD) methods. This thesis reports the first cases of applying $LaBr_3$ detectors in this way.

Experiments were conducted at the ANU Heavy Ion Accelerator Facility to determine the limits of $LaBr_3$ detectors in this context. Precessions have been successfully observed in states with lifetimes ranging between ~ 10 ns and ~ 3 μs, with precession periods ranging from 40 ns to 3 ns (well below the time resolution of HPGe detectors).

TDPAD techniques can be used to determine nuclear g factors by directly observing the precession of the nucleus in a magnetic field. Moreover, they are a powerful tool to probe the magnetic structure of ferromagnetic materials and the recoil implantation process.

As the primary example, the case of the internal field of Cd in gadolinium was chosen. This case is of interest as it relates to a particular g-factor measurement of the 10^+ state in ^{110}Cd which was smaller than expected [RSA95]. To clarify this discrepancy, the hyperfine fields of ^{107}Cd implanted into gadolinium have been studied by TDPAD with $LaBr_3$ detectors. A pulsed 48-MeV beam from the ANU 14UD Pelletron accelerator was employed together with the ^{98}Mo(^{12}C, 3n)^{107}Cd reaction. Insight into the implantation process and an explanation of the anomalous $g(10^+)$ measurement was found.

The limits of the present system were determined to be not with the $LaBr_3$ detectors, but with the beam-pulse resolution and stability. Future developments are in progress to implement sub-nanosecond beam-pulsing, and there is potential to resolve sub-nanosecond precession periods using $LaBr_3$ detectors.

Acknowledgements

There are many people who were integral to the completion of this work. First and foremost, my supervisor Andrew Stuchbery: thanks for all the insight, explanations, and time spent making sure the project was a success. Also huge thanks to Matt Reed – your input throughout the entire process is much appreciated. I wouldn't have been able to even start data analysis without the help of Tibor Kibedi, much gratitude for the time spent getting me set up with your sorting program `tsort`.

Thanks go to Justin Heighway for his help with target preparation, and Steve Battisson for making the Mu-metal shielding that proved very valuable.

Everyone who helped with the various experiments also: Aqeel Akber, Jackson Dowie, Tom Palazzo, Ben Coombes, Michell de Vries, Tomas Eriksen, A.J. Mitchell, Matt Gerathy, and Tamas Tornyi. The experiments would not have been possible without your help.

Contents

Declaration **iii**

1 Introduction **1**
- 1.1 The case of Cd in gadolinium . . . 2
- 1.2 $LaBr_3$ scintillator detectors . . . 3

2 Theoretical Background **5**
- 2.1 Multipole expansion of the field of the nucleus . . . 5
- 2.2 Nuclear Transitions . . . 6
  - 2.2.1 Multipole Radiation . . . 6
  - 2.2.2 Angular Distributions . . . 7
  - 2.2.3 Mixed Multipole Angular Distributions . . . 8
  - 2.2.4 Spin alignment in nuclear reactions . . . 9
- 2.3 Extranuclear perturbations . . . 10
  - 2.3.1 Magnetic Dipole Interactions . . . 10
  - 2.3.2 Electric Quadrupole Interactions . . . 11
- 2.4 Hyperfine Magnetic Fields . . . 12
  - 2.4.1 Orbital Field . . . 12
  - 2.4.2 Spin-dipolar Field . . . 12
  - 2.4.3 Contact Field . . . 12
- 2.5 Perturbed Angular Distribution Methods . . . 13
  - 2.5.1 Time Integral Perturbed Angular Distribution . . . 14
  - 2.5.2 Time Differential Perturbed Angular Distribution . . . 14
  - 2.5.3 Implantation and Perturbed Angular Distributions . . . 16

3 Experimental Background **19**
- 3.1 Scintillation Detectors . . . 19
  - 3.1.1 Un-activated inorganic scintillators . . . 19
  - 3.1.2 Activated inorganic scintillators . . . 20
  - 3.1.3 Energy measurement . . . 21
  - 3.1.4 Time measurement . . . 21
- 3.2 Semiconductor Diode Detectors . . . 21
  - 3.2.1 Energy measurement . . . 22
  - 3.2.2 Timing Measurement . . . 22

4 Experimental Methods **23**
- 4.1 Experimental Setup . . . 23

4.2 Electronic Setup 24
4.2.1 Description of Electronics Modules 24
4.2.2 Setup for TDPAD measurement 26
4.3 Data Acquisition 28

5 Data Analysis 29
5.1 Event by event data 29
5.2 TAC spectra alignment 30
5.3 Time and energy calibrations 30
5.4 Ratio function 32
5.5 Autocorrelation functions 33
5.6 Fourier transforms 34
5.7 Error Analysis 35
5.7.1 Ratio Function 35
5.7.2 Autocorrelation Function 36

6 Preliminary Experiments 37
6.1 Ge in iron 37
6.1.1 Target 37
6.1.2 ^{69}Ge in iron 38
6.1.3 ^{67}Ge in iron 39
6.1.4 Discussion 40
6.2 ^{54}Fe in nickel 43
6.2.1 Target 43
6.2.2 Results 44

7 ^{107}Cd in gadolinium 49
7.1 Target 49
7.2 Excitation Function 49
7.3 Results 51
7.3.1 Angular Distribution 52
7.4 Discussion 53
7.4.1 ^{107}Cd in gadolinium 53
7.4.2 ^{110}Cd 10^+ level g factor 57

8 ^{111}Sn in gadolinium: g-factor measurement 59
8.1 Measurement 59
8.2 Results 60
8.3 Discussion 61

9 Conclusion 65

Appendices 67

A Autocorrelation Functions 69
A.1 Discrete autocorrelation function 71
A.2 Autocorrelation simulations 72

B Angular Momentum Algebra 75
B.1 Coupling two angular momenta and Clebsch-Gordan coefficients 75

B.1.1 Wigner 3-j symbols 76
B.2 Coupling three angular momenta and Racah coefficients 76

List of Figures

2.1 A representation of a γ-ray transition between two nuclear states 6
2.2 A schematic of angular distribution methods 14
2.3 Recoil implantation and perturbed angular distributions 17

3.1 Energetic band structure of an activated scintillator 20
3.2 Comparison of HPGe and $LaBr_3$ detector energy resolution 22

4.1 Diagram showing the TDPAD detector setup 24
4.2 ANU Hyperfine Spectrometer 25
4.3 Electronics diagram for TDPAD measurement 27

5.1 An illustration of the background subtraction process 31
5.2 Partial level scheme for ^{68}Ge 32
5.3 The summed time spectra showing oscillations and exponential decay . . . 33

6.1 Energy spectrum for the ^{nat}Fe(^{16}O, 2pn) reaction 38
6.2 Time spectra gating on the 398-keV transition in ^{69}Ge 39
6.3 Ratio function for the 398-keV transition in ^{69}Ge 39
6.4 Autocorrelation for the 398-keV transition in ^{69}Ge 40
6.5 Time spectra for the 734-keV transition ^{69}Ge 41
6.6 A previous measurement of the $\frac{9}{2}^+$ isomer lifetime in ^{67}Ge 41
6.7 Ratio function for the 734-keV transition in ^{67}Ge 42
6.8 Autocorrelation for the 734-keV transition ^{67}Ge 42
6.9 Variation of spontaneous magnetization with temperature 43
6.10 Partial level scheme for ^{54}Fe 44
6.11 Energy spectrum for ^{54}Fe 44
6.12 Prompt peak used for alignment in the case of ^{54}Fe 45
6.13 Time spectra for the four cascading transitions from the 10^+ isomer. 46
6.14 Ratio functions for the four cascading transitions from the 10^+ isomer of ^{54}Fe. 46
6.15 Autocorrelation functions for the four cascading transitions from the 10^+ isomer of ^{54}Fe. 47
6.16 Fourier transforms of the autocorrelation functions formed for ^{54}Fe 48

7.1 Stopping power calculation for Cd in gadolinium 50
7.2 Partial level scheme of ^{107}Cd 50
7.3 Excitation function for ^{107}Cd 51
7.4 Energy spectrum for ^{107}Cd 52
7.5 Energy spectrum for ^{107}Cd showing the 1633-keV peak 52

7.6 The prompt peaks used to align the spectra for ^{107}Cd 53
7.7 Time spectra for the 640-keV transition in ^{107}Cd 53
7.8 Ratio function for the 640-keV transition in ^{107}Cd 54
7.9 Angular distributions for two transitions in ^{107}Cd 54
7.10 Simulated ratio functions due to electric field gradients 55
7.11 Simulated ratio function due to a continuous spread of hyperfine field strengths 56
7.12 The ratio function for the 640-keV transition in ^{107}Cd with a fitted curve . 56

8.1 Energy spectrum showing the $\frac{11}{2}^-$ isomer in ^{111}Sn. 60
8.2 Time spectra for the $\frac{11}{2}^-$ isomer in ^{111}Sn 60
8.3 Ratio function for the $\frac{11}{2}^-$ isomer in ^{111}Sn 61
8.4 Autocorrelation function for the $\frac{11}{2}^-$ isomer in ^{111}Sn 61
8.5 Partial decay scheme of ^{111}Sn 62
8.6 Energy spectrum showing the 1084-keV transition used to align the spectra 62
8.7 Prompt-peak time spectrum used to align the spectra for ^{107}Cd 63

A.1 Simulated cos(x) function with Gaussian noise 71
A.2 Autocorrelation function showing a single oscillation 72
A.3 Simulated data with two harmonic components and Gaussian noise 73
A.4 Autocorrelation function showing the two original frequencies 73

B.1 The coupling of two angular momenta $\boldsymbol{j_1}$ and $\boldsymbol{j_2}$ to form $\boldsymbol{j}$ 75
B.2 Two coupling schemes for three angular momenta 77

List of Tables

3.1 Comparison of scintillator materials 21

4.1 ADC allocations for the measurement 28

8.1 A comparison of magnetic moments for analogous $h_{\frac{11}{2}^{-}}$ states in the odd Cd and Sn isotopes. 63

1

Introduction

The magnetic moment of a nuclear state is one of its fundamental properties. It describes how the nucleus behaves in magnetic fields and provides a sensitive tool for assessing the accuracy of the various models of nuclear structure.

The g factor of a nuclear state is a proportionality constant that relates the magnetic moment of the state to its angular momentum. It is defined as

$$g = \frac{\mu}{\mu_N} I, \tag{1.1}$$

where μ_N is the nuclear magneton (defined in Section 2.1), and I is the angular momentum of the state. Depending on the method, experiments may determine either the magnetic moment or g factor.

The technique primarily examined in this work is *Time Differential Perturbed Angular Distribution* (TDPAD). This enables magnetic moments of long-lived nuclear states to be determined via a measurement of a g factor. The measurement uses the principle of nuclear precession; that is a nucleus in the presence of a magnetic field will precess about the axis of the field at the *Larmor frequency*, given by

$$\omega_L = -gB\frac{\mu_N}{\hbar}. \tag{1.2}$$

The Larmor frequency provides the experimental link; this is a quantity which can be observed, thus, if the magnetic field strength is known, the g factor can be evaluated.

For the purposes of this work, the experiments are conducted by implanting a nucleus of interest into a ferromagnetic host. This means that the relevant magnetic field is the *internal hyperfine field* at the implantation site, denoted by B_{hf}. These fields can be orders of magnitude larger than the externally applied field that magnetizes the host, meaning smaller g factors can be measured as the precession frequency is higher, or g factors of shorter-lived states can be measured through observations of the precession period within the lifetime of the state.

1.1 The case of Cd in gadolinium

The particular case examined in this work is Cd implanted into gadolinium (by convention the chemical symbol is used for the impurity whilst the host material is written in full). The interest of this case stems from the g-factor measurement made in [RSA95]. The 10^+ isomer (mean life $\tau = 703(35)$ ps [Juu+94; KAK98; Pii+93; Har+01]) in ^{110}Cd was studied, and a g factor of $g(10^+) = -0.09(3)$ was determined [RSA95]. However, this value is much smaller than expected by models or other experiments. There is a well known $\frac{11}{2}^-$ state with a $g = -0.189(2)$ in ^{107}Cd, as well as other well known $\frac{11}{2}^-$ state g factors in the odd Cd isotopes [Ber+74; Hag+74; Rag89]. The fact that the isomer in ^{110}Cd is expected to be a $\nu(h_{\frac{11}{2}})^2$ state[1] whilst the isomer in ^{107}Cd is a $\nu(h_{\frac{11}{2}})$ state, together with the theorem

$$g(j) = g(j^2)_J, \tag{1.3}$$

means that $g(10^+)$ and $g(\frac{11}{2}^-)$ should be similar [Law80]. In Equation 1.3, $g(j)$ denotes the g factor of a single nucleon in the orbit j and $g(j^2)_J$ denotes the g factor of two nucleons coupled to spin J in the same orbit. This work is an investigation into the possible causes of the discrepancy in the measured values.

The method used to make the measurement in ^{110}Cd is a *Time Integral Perturbed Angular Distribution* method. This is explained in detail in Section 2.5.1, however it is important to note that when used in an implantation experiment, different nuclei can be implanted onto different “sites” in the host material, which can have different field strengths. In the integral method, what is observed is an average over all these different sites and field strengths. This can result in incorrect measurements if it is assumed that all nuclei are implanted onto full-field sites. It is this concern that motivated the present work as the ^{110}Cd $g(10^+)$ measurement was an integral measurement.

To gain insight into the implantation process for the specific case of Cd in gadolinium, a longer lived isomer with a well known g factor can be used to probe the internal magnetic structure. An ideal probe is the $\frac{11}{2}^-$ isomer in ^{107}Cd. The TDPAD method is applicable since the isomer is long lived, and allows the different field sites present to be evaluated, as will be described below.

---

[1] This is standard nuclear structure notation, denoting that the excitation of a neutron (ν) or proton (π) with orbital angular momentum l being given in standard spectroscopic notation (s, p, d,...) and the total angular momentum $j = l + s$ expressed as a subscript. The exponent of 2 denotes that there are two neutrons forming the excitation.

1.2 LaBr$_3$ scintillator detectors

TDPAD techniques are valuable tools that can be used to determine g factors, and probe the magnetic structure of ferromagnetic materials and the implantation process. However, one of the limiting factors is the timing resolution of the detectors, which limits the minimum period of any precessions that can be measured (or correspondingly the maximum Larmor frequency). This can be a serious limitation in the case of shorter lived states with large g factors, or large hyperfine field strengths.

LaBr$_3$ detectors are a recent development in detector technology that are favourable in several respects when applied with the TDPAD technique. They have better timing and energy resolution than NaI detectors (which have been typically used for TDPAD measurements). Whilst the energy resolution of LaBr$_3$ detectors is not as good as the solid state HPGe detectors, their timing resolution is superior. FWHM timing resolution for HPGe detectors is typically ~ 10 ns, whilst LaBr$_3$ detectors can easily achieve resolutions of ~ 300 ps. The combination of good timing and energy resolution means that LaBr$_3$ detectors are ideal for in-beam TDPAD experiments, and enable measurements to be made that were not previously possible. In-beam measurements prepare the states of interest using a particle accelerator, and consequently allow a wider variety of states to be probed. This work is the first instance where LaBr$_3$ detectors have been applied to measuring magnetic moments with the TDPAD technique as an in-beam measurement.

2

Theoretical Background

Nuclear physics concerns the study of the nucleus and its properties. In specific, nuclear structure examines the energetic structure of nuclei – the excited states, their properties, transitions between them, and models developed to explain these observations. The properties of interest include excitation energies, lifetimes, angular momentum (spin), parity, and magnetic dipole and electric quadrupole moments. The transitions between excited states typically involve the emission of a single γ ray, however, processes such as internal conversion, double-γ, and pair production are also possible. Nuclei are understood by a wide variety of models, for example the shell model, vibrational models, and deformed rotor models are just a few of the more common ones.

This work will focus primarily on the measurement of g factors or equivalently magnetic dipole moments.

2.1 Multipole expansion of the field of the nucleus

The electromagnetic field produced by any distribution of electric charges and currents can be described by a combination of electric and magnetic *multipole fields* – electric and magnetic monopoles, dipoles, quadrupoles, octupoles, and so forth. This is a powerful and instructive way to describe nuclear properties [Kra88].

Each multipole moment has a particular parity, determined by the order (L, number of poles 2^L) and type (electric or magnetic). For electric multipole moments, the parity is $(-1)^L$, and for magnetic moments, the parity is $(-1)^{L+1}$. When using a multipole expansion to describe a nucleus, the parity of each non-zero multipole moment must be 1. Hence the only non-zero moments are the electric monopole, magnetic dipole, electric quadrupole, and so on. Since higher order multipole moments quickly become negligible, these three are the only ones considered.

The electric monopole moment is simply the net charge of the nucleus Ze. The magnetic dipole moment however forms a valuable link from theory to experiment. Theoretical models predict values for the magnetic dipole moment, and correspondingly, it can be measured experimentally.

The g factor, or *gyromagnetic ratio* g, is defined by

$$\mu = gj\mu_N, \tag{2.1}$$

where μ is the magnetic dipole moment, j the total angular momentum of the relevant state, and μ_N the *nuclear magneton* – a constant defined analogous to the Bohr magneton,

$$\mu_N = \frac{e\hbar}{2m_p}, \tag{2.2}$$

where m_p is the rest mass of the proton. A familiar classical magnetic dipole is a current carrying loop – charges moving in a circle. Thus the magnetic moment of a nucleus is closely linked to the internal motion of its charges.

2.2 Nuclear Transitions

An initial excited nuclear state $|i\rangle$ has associated energy (E_i), angular momentum ($\boldsymbol{J_i}$, magnitude j_i, projection m_i), and parity (π_i). It can decay internally to a less excited state $|f\rangle$ (E_f, $\boldsymbol{J_f}$, j_f, m_f, π_f) via a γ-ray transition. By conservation of energy, $\hbar\omega = E_i - E_f$ for the emitted photon. However, angular momentum and parity must also be conserved, so the photon must carry away angular momentum $\boldsymbol{J} = \boldsymbol{J_i} - \boldsymbol{J_f}$, with $|\boldsymbol{J}| = L$, and its projection $m = m_i - m_f$. Moreover, the parity π of the radiation must fulfill $\pi \times \pi_i = \pi_f$.

2.2.1 Multipole Radiation

The process of γ-ray emission can also be viewed as an electromagnetic field carrying away the relevant energy, angular momentum, and parity. By solving Maxwell's equations with the relevant boundary conditions, and taking a multipole expansion, the outgoing radiation can be expressed as a combination of electric and magnetic multipole fields. These are denoted by σL, where $\sigma \in \{E, M\}$ representing electric or magnetic character, and L is

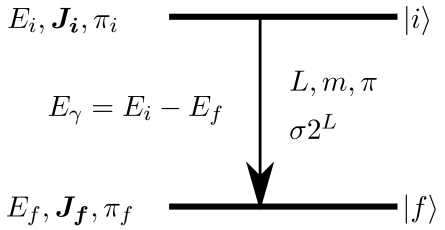

Figure 2.1: A transition between initial and final states $|i\rangle$ and $|f\rangle$ proceeds by a γ-ray emission carrying away relevant energy E_γ, angular momentum L, and parity π.

the *multipolarity* of the transition, the total angular momentum carried away by the field, and 2^L is the number of charges in the classical analogue. For example, $\sigma L = E2$ denotes an *electric quadrupole* radiation, since $2^2 = 4$. The parity of the fields is as follows: for *electric* $(-1)^L$ and for *magnetic* $(-1)^{L+1}$.

In the quantum mechanical formalism, a *multipole operator* can be defined to act on an initial state $|i\rangle$, changing it to a final state $|f\rangle$ whilst emitting a photon of the appropriate energy, parity, and multipolarity. Thus, the matrix elements of the multipole operator are

$$m_{fi}(\sigma L) = \langle f|\, m(\sigma L)\, |i\rangle\,. \tag{2.3}$$

Considering now a particular transition, it becomes clear that physical arguments impose restrictions on the kind of emission that is possible. For example, $\boldsymbol{J} = \boldsymbol{J_i} - \boldsymbol{J_f}$, meaning that

$$|j_i - j_f| \leqslant L \leqslant j_i + j_f. \tag{2.4}$$

Parity must also be conserved, so

$\Delta\pi =$ no: even electric, odd magnetic

$\Delta\pi =$ yes: odd electric, even magnetic.

As an example, consider a transition between an initial state $|i\rangle$ with $j^\pi = 4^+$ to a final 2^+ state. Since $2 \leqslant L \leqslant 6$, and there is no parity change, only $E2, M3, E4, M5$, and $E6$ transitions are possible. Of these, E2, the lowest multipolarity is by far the most dominant [Ham75; MY76].

2.2.2 Angular Distributions

Consider a γ-ray transition of angular momentum L between states of spin j_i and j_f. Note that there are $2j_i + 1$ possible m_i substates for the initial state, and $2j_f + 1$ possible final substates m_f. Each $m_i \rightarrow m_f$ transition has its own characteristic spatial distribution, given by

$$Z_{Lm}(\theta) = \frac{(-1)^{m-1}}{4\pi} \sum_k \langle L1L-1|k0\rangle \langle LmL-m|k0\rangle\, P_k(\cos\theta), \tag{2.5}$$

where θ is the angle between the emitted radiation and the quantization axis, and $P_k(\cos\theta)$ is the Legendre polynomial of order k [MY76]. To predict what the angular distribution of observed γ rays will be, the population of each m_i substate $P(m_i)$ must therefore be known, as well as the relative probability for an $m_i \rightarrow m_f$ transition $G(m_i, m_f)$. Thus, the angular distribution is given by

$$W_L(\theta) = \sum_{m_i, m} P(m_i) G(m_i, m_f) Z_{Lm}(\theta). \tag{2.6}$$

Using the Wigner-Eckart theorem [Mes66; Sie66; Ros57], the matrix elements of the transition can be expressed as

$$\langle j_f m_f | \, m(\sigma L) \, | j_i m_i \rangle = \langle j_i m_i L m | j_f m_f \rangle \, \langle j_f || \, m(\sigma L) \, || j_i \rangle \,, \tag{2.7}$$

where $\langle j_i m_i L m | j_f m_f \rangle$ is a Clebsch-Gordan coefficient (see Appendix B). Conceptually, the theorem expresses the transition as the product of a 'geometric' part (the Clebsh-Gordan coefficient) and a 'nuclear' part (called the reduced matrix element), which does not depend on either m_i, m_f, or m. Calculating the relative probability $G(m_i, m_f)$, the reduced matrix elements cancel, and

$$G(m_i, m_f) = | \, \langle j_i m_i L m | j_f m_f \rangle \, |^2. \tag{2.8}$$

This gives the following expression for the angular distribution:

$$\begin{aligned}
W_L(\theta) &= \frac{(-1)^1}{4\pi} \sum_k \langle L 1 L-1 | k 0 \rangle \, P_k(\cos\theta) \\
&\quad \times \sum_{m_i, m} (-1)^m P(m_i) \, \langle L m L-m | k 0 \rangle \, | \, \langle j_i m_i L m | j_f m_f \rangle \, |^2 && (2.9) \\
&= \frac{(-1)^1}{4\pi} \sum_k \langle L 1 L-1 | k 0 \rangle \, P_k(\cos\theta) \\
&\quad \times \sum_{m_i} (-1)^{j_f - m_i} (2j_f + 1) \, \langle j_i m_i j_i - m_i | k 0 \rangle \, W(j_1 j_1 L L; k j_f) P(m_i) && (2.10) \\
&= \sum_k \rho_k(j_i) F_k(j_f L j_i) P_k(\cos\theta), && (2.11)
\end{aligned}$$

where the *statistical tensor* $\rho_k(j_i)$ describes the alignment of the initial state, and is given by

$$\rho_k(j_i) = \sqrt{2j_i + 1} \sum_m (-1)^{j-m} \, \langle j m j - m | k 0 \rangle \, P(m), \tag{2.12}$$

for $k = 0, 1, 2, ..., 2j$. The *F-coefficient*, $F_k(j_f L j_i)$, describes the angular momentum coupling of the transition and is defined as

$$F_k(j_f L j_i) = (-1)^{1 + j_i - j_f} \sqrt{2j_i + 1} (2L + 1) \, \langle L 1 L - 1 | k 0 \rangle \, W(j_i j_i L L; k j_f). \tag{2.13}$$

More detailed and general derivations can be found in references [Ham75; MY76; Cer74; Sie66]

2.2.3 Mixed Multipole Angular Distributions

The formula above assumes that the transition of interest has only a single multipolarity. In general, γ-ray transitions will have a mixed multipole character – for example a $2^+ \rightarrow 2^+$ transition will have major $M1$ and $E2$ γ-ray components. The formalism of angular distributions accounts for mixed multipolarity transitions by using the a modified definition of the F-coefficients, namely

$$F_k(j_f L L' j_i) = (-1)^{1+j_i-j_f} \sqrt{(2j_i+1)(2L+1)(2L'+1)}\, \langle L1L'-1|k0\rangle\, W(j_i j_i L L'; k j_f). \tag{2.14}$$

In this case the angular distribution is expressed as

$$W(\theta) = \sum_k \rho_k(j_i) A_k(j_i L L' j_f) P_k(\cos\theta), \tag{2.15}$$

with the A coefficients (also known as *generalised F-coefficients*) defined by

$$A_k(j_i L L' j_f) = \frac{1}{1+\delta^2}\left(F_k(j_f L L j_i) + 2\delta F_k(j_f L L' j_i) + \delta^2 F_k(j_f L' L' j_i)\right), \tag{2.16}$$

and δ is the *mixing ratio* of the two multipolarities, defined by the ratio of the absolute transition amplitudes

$$\delta(LL') = \frac{\gamma(L')}{\gamma(L)}. \tag{2.17}$$

These are typically normalised so that $F_0(j_f L L' j_i) = \delta_{LL'}$, $\rho_0(j_i) = 1$, and hence $A_0(j_i L L' j_f) = \delta_{LL'}$, where $\delta_{LL'}$ is the Kronecker delta symbol. Parity conservation requires that k is even, and the properties of F_k mean that $k < 2L_{max}$, where L_{max} is the larger of L and L'. [Sie66; SR02].

2.2.4 Spin alignment in nuclear reactions

The final piece of information concerning angular distributions is the alignment produced by a nuclear reaction. Of course, if the population of the magnetic substates is uniform ($P(m_i) = 1/(2j_i+1)$ for all m_i), only an isotropic distribution will be observed. However, if the state of interest is populated using a suitable nuclear reaction (as it will be for the TDPAD technique), an “oblate alignment” of the substate population can be created. It is typical to assume a Gaussian distribution of $P(m_i)$:

$$P(m_i) = \frac{\exp(-m_i^2/2\sigma^2)}{\sum_{m_i'=-j_i}^{j_i} \exp(-m_i'^2/2\sigma^2)}. \tag{2.18}$$

Here σ is a parameter describing the degree of orientation, and typically for heavy-ion induced fusion-evaporation reactions, $\sigma/j_i \approx 0.3$. This expression for $P(m_i)$ allows $\rho_k(j_i)$ to be calculated if σ is known. Here the beam axis is the z-axis, and the nuclear angular momentum is aligned in the plane perpendicular to the beam axis. There is symmetry about the beam axis in the cases discussed here, so $P(m_i) = P(-m_i)$.

Thus, once the multipolarity (and mixing ratio) of a transition is known, the alignment can be estimated, and the angular distribution of the transition found. The characterizing parameters of this information are the A_k coefficients. Since $k \leqslant 2L_{max}$, only the first few are the important – for transitions with multipolarity 2 (as will be considered in this work) the A_2 and A_4 coefficients characterize the angular distribution [Ham75; SR02].

2.3 Extranuclear perturbations

2.3.1 Magnetic Dipole Interactions

If an extranuclear perturbation is present at the (excited) nucleus but before the decay occurs, the effect of this on the angular distribution can be calculated. The formalism of γ-γ angular correlations will be used to introduce the effect of the *perturbation factor* $G_{k_1k_2}^{N_1N_2}(t)$, which modifies the alignment of the initial state, and hence ρ_k. The perturbation factors completely characterize the effect of the extranuclear perturbation on the orientation of the initial state. They are formed by taking the Hamiltonian of the interaction, finding the unitary time-evolution operator associated, acting that on the initial density matrix, and then converting back to a spherical tensor notation.

For a static magnetic field, the Hamiltonian describing the interaction is simply

$$K = -\boldsymbol{\mu} \cdot \boldsymbol{B} = \mu_z B, \tag{2.19}$$

(when $\boldsymbol{B}$ is oriented along the z-axis). Using the m-basis, the Hamiltonian is diagonal and the energy eigenvalues are

$$E_m = -B\mu\frac{m}{j}. \tag{2.20}$$

The Larmor frequency ω_L is defined by the splitting of the m-substates:

$$\omega_L = \frac{E_{m+1} - E_m}{\hbar} = -\frac{B\mu}{j\hbar} = -\frac{g\mu_N B}{\hbar}. \tag{2.21}$$

The unitary operator $\Lambda(t)$ associated with the perturbation is then given by

$$\langle jm| \Lambda(t) |jm'\rangle = \exp(-i\omega_L mt)\delta_{mm'}. \tag{2.22}$$

The perturbation factor is generally

$$\begin{aligned} G_{k_1k_2}^{N_1N_2}(t) = \sqrt{(2k_1+1)(2k_2+1)} \sum_{m_am_b} (-1)^{m_a-m_b} \begin{pmatrix} j & j & k_1 \\ m'_a & -m_a & N_1 \end{pmatrix} \begin{pmatrix} j & j & k_2 \\ m'_b & -m_b & N_2 \end{pmatrix} \\ \times \langle m_b| \Lambda(t) |m_a\rangle \langle m'_b| \Lambda(t) |m'_a\rangle^*, \end{aligned} \tag{2.23}$$

where the Wigner 3-j symbols have been used (see Appendix B). For $\Lambda(t)$ as in equation 2.22, this becomes

$$
\begin{aligned}
G_{k_1k_2}^{N_1N_2}(t) &= \sqrt{(2k_1+1)(2k_2+1)}\sum_{m_a}\begin{pmatrix} j & j & k_1 \\ m'_a & -m_a & N_1 \end{pmatrix}\begin{pmatrix} j & j & k_2 \\ m'_a & -m_a & N_2 \end{pmatrix} \\
&\quad \times \exp(-i\omega_L t(m_a - m'_a)) \qquad (2.24)\\
&= \sqrt{(2k_1+1)(2k_2+1)}\exp(-i\omega_L t N_1) \\
&\quad \times \sum_{m_a}\begin{pmatrix} j & j & k_1 \\ m'_a & -m_a & N_1 \end{pmatrix}\begin{pmatrix} j & j & k_2 \\ m'_a & -m_a & N_2 \end{pmatrix}\delta_{N_1N_2}, \qquad (2.25)
\end{aligned}
$$

because of the condition $N_1 = m_a - m'_a = N_2$ that is imposed by the 3-j symbol. Then using the orthogonality of the 3-j symbols, note that

$$G_{k_1k_2}^{N_1N_2}(t) = \exp(-iN_1\omega_L t)\delta_{N_1N_2}\delta_{k_1k_2}. \qquad (2.26)$$

This gives the time-dependent angular distribution as

$$
\begin{aligned}
W(\theta,\phi,t) &= \sum_{k_1k_2,N_1N_2} A_{k_1k_2}G_{k_1k_2}^{N_1N_2}(t)Y_{k_1N_1}^*(\beta,\alpha)Y_{k_2N_2}(\theta,\phi) \qquad (2.27)\\
&= \sum_{k,N} A_{kk}\exp(-iN\omega_L t)Y_{kN}^*(\beta,\alpha)Y_{kN}(\theta,\phi), \qquad (2.28)
\end{aligned}
$$

where the orientation of the magnetic field is given by the angles α, β and the angle of the emitted radiation is given by θ, ϕ. When the magnetic field is oriented perpendicular to the observation plane, this simplifies further to

$$W(\theta,t) = \sum_k A_{kk}P_k(\cos(\theta - \omega_L t)), \qquad (2.29)$$

that is, the angular distribution precesses with the nucleus at the Larmor frequency ω_L. To connect back to the formalism of angular distributions, A_{kk} is simply replaced by $\rho_k A_k$, as defined in Section 2.2.2 [Sie66; Cer74].

2.3.2 Electric Quadrupole Interactions

Along with the magnetic hyperfine interaction there can be an electric quadrupole interaction in non-cubic metals such as gadolinium. The magnetic precession frequency has been defined as

$$\omega_L = -gB_{hf}\frac{\mu_N}{\hbar}. \qquad (2.30)$$

An electric field gradient (EFG) V_{zz} interacting with the nuclear quadrupole moment Q gives rise to an “interaction” frequency of

$$\omega_E = \frac{eQV_{zz}}{4\hbar j(2j-1)}, \tag{2.31}$$

for a state of angular momentum j. The electric field gradient V_{zz} is often given in units of 10^{17} V/cm^2. In gadolinium the largest value observed is $V_{zz}(Gd) \sim 19 \times 10^{17}$ V/cm^2. For Cd in gadolinium $V_{zz} \sim 1 \times 10^{17}$ V/cm^2. Note that ω_E depends strongly on j, becoming smaller as j increases [Chr83].

2.4 Hyperfine Magnetic Fields

The (magnetic) hyperfine field of a nucleus in a particular solid material is the field produced at the site of the nucleus by the electrons of the material [GE96]. In ferromagnetic metals, this is a useful phenomenon that allows g-factor measurements to be made by using the hyperfine field. Conversely, known g factors can be used to probe the magnetic structure of a ferromagnetic metal.

The internal hyperfine field at dilute impurities has three contributing factors, the *orbital*, *spin-dipolar*, and *contact* fields, each from various interactions between the nucleus and electrons around it.

2.4.1 Orbital Field

The orbital field is the result of the orbital motion of the electrons bound to the nucleus, forming a current loop. For any paired electrons, the effect cancels and thus only unpaired electrons need to be considered. Consequently for a non-magnetic impurity the net effect is vanishing, due to the filled d- or f-shells. The orbital field is also of only minor significance in transition metals as a result of orbital momentum quenching [KM86; Lee88].

2.4.2 Spin-dipolar Field

The spin-dipolar field is a result of the spin-magnetization of atomic, non-s electrons that are external to the nucleus. However, this vanishes for host metals with cubic symmetry [Mar58; Lee88]. Thus for the cases considered with iron or nickel hosts, the spin-dipolar contribution is not relevant. For the case of a gadolinium host, the crystal structure is hexagonal close-packed meaning non-negligible spin-dipolar fields may be present.

2.4.3 Contact Field

The contact field is the major contribution to the magnetic hyperfine field in the cases considered here. In general, the contact field is a result of the interaction between an s-electron and the nucleus due to their wavefunction overlap. The contact field is produced by the Fermi contact interaction. However, the localized s-shells are all filled with paired electrons, meaning that the net contact field vanishes in most situations. Nonetheless in the case of an (even very small) unbalanced spin density of the s-electrons, significant hyperfine fields can be produced.

The contact field is reduced to two contributions that can produce such an imbalance: the *Core Polarization* (CP) and *Conduction Electron Polarization* (CEP) fields

Core Polarization Field

The core polarization field is a result of the exchange interaction between an unfilled (outer) atomic shell and an inner s-electron of the same nucleus. The polarization creates a large hyperfine field at the nucleus, and consequently is the major contributing factor for many cases. For example, for transition metal impurities such as iron, the unpaired d-electrons cause large core-polarization effects (and hence hyperfine fields) irrespective of the host material. Core polarization can produce hyperfine fields in the opposite direction to the magnetization of the host (i.e. to the polarizing external field, depending on the degree of filling of the outer shell). This is indicated by a negative B_{hf} value.

Conduction Electron Polarization Field

The conduction electron polarization field is a similar effect but as a result of the polarization of outer s-electrons. These electrons become unbound from the nucleus, and join the conduction band. Because of the s-d exchange interaction, they become polarized and generate a contact field with the impurity nucleus [Lee88]. The conduction electron polarization effect is most sensitive to the host environment.

These hyperfine interactions are useful in the context of nuclear physics to produce fields which are orders of magnitude larger than would otherwise be available. A small, external, static magnetic field magnetizes the ferromagnetic host, and the large hyperfine fields produced allow us to probe the magnetic structure of the nucleus in ways that would otherwise not be feasible. For example, the hyperfine fields for Cd and Sn in gadolinium are of the order of 30 T and in the opposite direction to the polarizing field.

2.5 Perturbed Angular Distribution Methods

The frequency of a nucleus precessing in a magnetic field B is given by the Larmor precession frequency:

$$\omega_L = -gB\frac{\mu_N}{\hbar}. \tag{2.32}$$

Since nuclear transitions can be anisotropic, and the angular distribution precesses with the nucleus, it is possible to measure ω_L through γ-ray spectroscopy. This determines the relationship between g and B. Depending on the lifetime of the state, two classifications of techniques can be used – *time integral* and *time differential* perturbed angular distribution techniques.

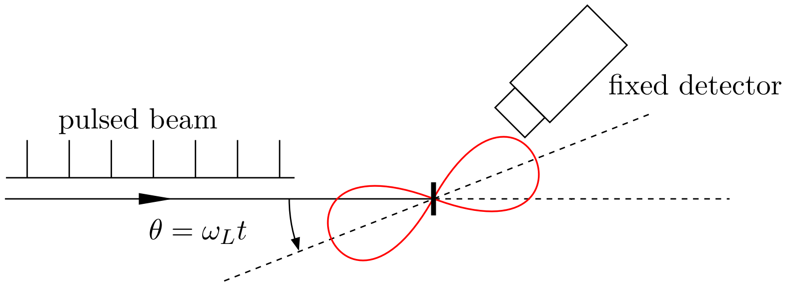

Figure 2.2: A schematic of angular distribution methods. The angular distribution (red) rotates at the Larmor frequency ω_L. A fixed detector measures the oscillations in intensity of the γ ray depopulating the isomer of interest excited by the pulsed beam.

Typically for time differential methods a pulsed beam will be used to populate the excited state, with γ rays time correlated with each pulse [Cer74].

2.5.1 Time Integral Perturbed Angular Distribution

If the lifetime of the initial state τ is small compared the precession period π/ω_L, it is impossible to determine ω_L by a direct observation of the frequency. However by averaging over the lifetime of the state an indirect measurement can be made:

$$\omega_L = -gB\frac{\mu_N}{\hbar} \tag{2.33}$$

$$\omega_L\tau = -gB\frac{\mu_N}{\hbar}\tau \tag{2.34}$$

$$\Delta\theta \approx -gB\frac{\mu_N}{\hbar}\tau, \tag{2.35}$$

where $\Delta\theta$ is the average precession angle, which can be measured. If the lifetime of the state and B are known, the g factor can be measured.

2.5.2 Time Differential Perturbed Angular Distribution

If the lifetime of the excited state is long compared to the precession period ($\pi/\omega_L < \tau$), a time spectrum can be measured. The time between each beam pulse and the γ-ray detection event is noted, and a histogram of the recorded times is formed. The intensity of emitted γ rays obeys

$$I(\theta, t) = I_0 e^{-t/\tau} W(\theta, t). \tag{2.36}$$

The spectrum obtained shows the exponential decay convolved with the time-dependence of the angular distribution for a particular θ value, where θ is the angle between the detector and beam axis. To remove the exponential component, a ratio function is formed with two detectors separated by $\pi/2$ radians:

$$R(\theta,t) = \frac{I(\theta,t) - I(\theta+\pi/2,t)}{I(\theta,t) + I(\theta+\pi/2,t)}. \tag{2.37}$$

Substituting in equations 2.36 and 2.29, it is found, taking only terms with $k \leqslant 4$, that

$$R(\theta,t) = \frac{A_{22}[P_2(\cos(\alpha)) - P_2(\cos(\alpha+\pi/2))] + A_{44}[P_4(\cos(\alpha)) - P_4(\cos(\alpha+\pi/2))]}{A_{22}[P_2(\cos(\alpha)) + P_2(\cos(\alpha+\pi/2))] + A_{44}[P_4(\cos(\alpha)) + P_4(\cos(\alpha+\pi/2))]}, \tag{2.38}$$

using $\alpha = \theta - \omega_L t$ for convenience. Substituting in the explicit expressions for $P_2(\cos\theta)$ and $P_4(\cos\theta)$, it is found that

$$\begin{aligned} R(\theta,t) = & \Big[A_{22}\frac{3}{2}\left(\cos^2(\alpha) - \cos^2(\alpha+\pi/2)\right) \\ & + A_{44}\frac{1}{8}\Big(35[\cos^4(\alpha) - \cos^4(\alpha+\pi/2)] \\ & -30[\cos^2(\alpha) - \cos^2(\alpha+\pi/2)]\Big)\Big] \Big/ \\ & \Big[2 + A_{22}\frac{1}{2}\left(3[\cos^2(\alpha) + \cos^2(\alpha+\pi/2)] - 2\right) \\ & A_{44}\frac{1}{8}\Big(35[\cos^4(\alpha) + \cos^4(\alpha+\pi/2)] \\ & -30[\cos^2(\alpha) + \cos^2(\alpha+\pi/2)] + 6\Big)\Big]. \end{aligned} \tag{2.39}$$

Using the relations

$$\cos^2(x) = \frac{1}{2}\cos(2x) + \frac{1}{2}, \tag{2.40}$$

$$\cos(x+y) = \cos(x)\cos(y) - \sin(x)\sin(y), \tag{2.41}$$

note that

$$\cos^2(\alpha) - \cos^2(\alpha+\pi/2) = \cos(2\alpha), \tag{2.42}$$

$$\cos^4(\alpha) - \cos^4(\alpha+\pi/2) = \cos(2\alpha), \tag{2.43}$$

$$\cos^2(\alpha) + \cos^2(\alpha+\pi/2) = 1, \tag{2.44}$$

$$\cos^4(\alpha) + \cos^4(\alpha+\pi/2) = \frac{1}{8}\cos(4\alpha) + \frac{3}{8}. \tag{2.45}$$

This gives the following:

$$R(\theta,t) = \frac{((3/2)A_{22} + (5/8)A_{44})\cos(2(\theta - \omega_L t))}{2 + (1/2)A_{22} + (9/32)A_{44} + (35/32)A_{44}\cos(4(\theta - \omega_L t))} \tag{2.46}$$

$$\approx \frac{3A_{22}}{4 + A_{22}}\cos(2(\theta - \omega_L t)). \tag{2.47}$$

The approximation in the final step is that $|A_{44}| \ll |A_{22}|$, or equivalently that $A_{44}/A_{22} \approx 0$. Thus forming the ratio function allows us to not only identify the Larmor frequency but also estimate A_{22} (and A_{44}) [Cer74].

Limitations

The TDPAD method is powerful, but limited in its applicability in several respects. The requirement that the lifetime of the state is long in comparison to the precession period means that TDPAD is unsuitable for:

- short lifetimes
- low g factors
- small fields

Clearly, increasing the field strength can decrease the precession period and allow smaller g factors in states with shorter lifetimes to be measured. However, there is also a lower limit on the precession periods that can be measured – the timing resolution of the experimental setup. Both detector resolution and beam-pulse resolution contribute to this limit. If the combination of these creates an uncertainty that is of the same order as the precession period, then the Larmor frequency cannot be resolved.

In summary, if Δt is the timing resolution of the experimental system, the following relation holds:

$$\Delta t \lesssim \frac{\pi}{\omega_L} \lesssim \tau, \tag{2.48}$$

which describes the conditions necessary for TDPAD to be viable [Cer74].

2.5.3 Implantation and Perturbed Angular Distributions

Creating a large magnetic field with a macroscopic solenoid is difficult and even then the field is limited in magnitude. For example, fields produced with superconducting solenoids are typically of the order of 1-10 Tesla. However, hyperfine fields can be orders of magnitude larger, and significantly easier to produce (the magnetizing field needs to be comparatively small). Thus, using hyperfine fields in g-factor measurements is advantageous – lower g factors of shorter-lived states can be accessed.

To access the internal hyperfine field of a ferromagnetic host, an implantation process must occur. A beam of heavy ions is accelerated to create the state of interest in a fusion-evaporation reaction with the first layer of the target. The created nuclei recoil into the second layer, which is a ferromagnetic host magnetized by an external field. The recoiling nuclei stop and precess in the hyperfine field of the host, allowing the g-factor measurement to be made.

It is important to note however, that the implantation process does not necessarily have the same outcome from event to event. There are potentially several kinds of sites (substitutional, interstitial, damaged) on which the implanted nuclei can reside and precess. These sites can have different hyperfine fields, resulting in several frequencies being present in the observed precession [Bos+71; LRR91; Bos+70].

In cases of non-cubic symmetry such as gadolinium, the electric field gradient can also be a relevant consideration. It will be shown later that these interactions appear to play a small role in the present work, because they are much weaker than the magnetic interactions.

In many cases the TDPAD method allows us to resolve the distinct frequencies in the time spectra and ratio functions obtained. However, the integral method does not; what is found instead is an average over all sites and fields, and this "blind averaging" is a potential source of large systematic error.

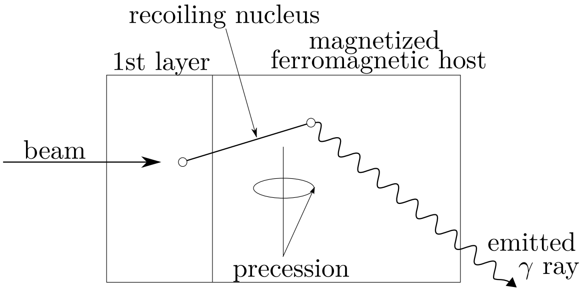

Figure 2.3: The beam and first layer of the target undergo a fusion-evaporation reaction. The products recoil into the second layer, a ferromagnetic magnetized foil. The nucleus stops, precesses under the hyperfine field, and then decays, emitting a γ ray. This is detected and allows the precession frequency to be determined.

3

Experimental Background

3.1 Scintillation Detectors

Scintillation detectors can be classified as either organic scintillators, or inorganic scintillators. The motivation for this project is to investigate the properties of $LaBr_3$ detectors, and so accordingly inorganic scintillators will be the focus.

3.1.1 Un-activated inorganic scintillators

Inorganic scintillators are comprised of a crystal lattice, the electronic structure of which forms the basis for their operation. The energy states available to electrons are represented in Fig. 3.1. There are three main bands – the valence band, in which the electrons are bound to nuclei, the conduction band, where the electrons have sufficient energy that they can flow freely through the semiconductor crystal, and between them, what is known as the “forbidden band”, a region of forbidden electronic energies.

A charged particle will excite a large number of electrons from the valence band to the conduction band as it passes through the detector. This process creates electron-hole pairs, between the positive holes in the valence band and the electrons in the conduction band. After some characteristic time the excited electrons will decay back to the valence band, emitting photons of the relevant energy. A photomultiplier tube detects the emitted photons and generates an electronic pulse correspondingly.

The energy of the re-emitted photons, however, is often of a shorter wavelength than visible light. This makes it difficult for a photomultiplier tube to detect. Additionally, if the re-emitted photon has an energy of more than the band gap, it can be *self-absorbed* by the

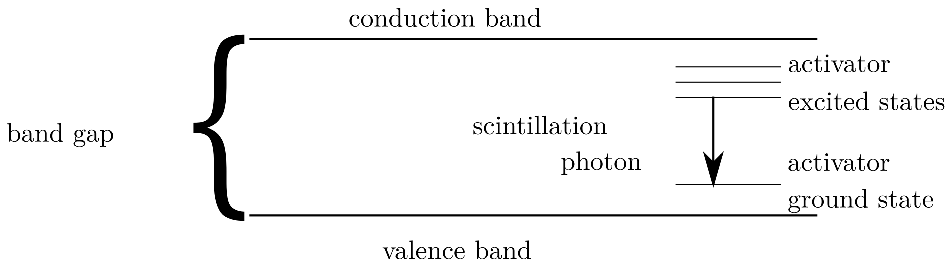

Figure 3.1: Energetic band structure of an activated scintillator [Kno00].

crystal, leading to a loss of efficiency. These two features mean that un-activated or pure scintillators often have a low light yield, and low energy resolution.

3.1.2 Activated inorganic scintillators

Inorganic scintillators such as $LaBr_3$ are doped with impurities known as *activators*. The activator is indicated in brackets; i.e. $LaBr_3$(Ce) denotes a $LaBr_3$ crystal doped with Cerium. The activators disrupt the band structure, creating allowed energetic levels which are in the forbidden band. These are denoted *activator sites* in Fig. 3.1.

In contrast to a pure scintillator, once the radiation is absorbed, the positive hole will drift to and ionize an activator site (the ionization energy of the activator sites is lower than that of a regular lattice site). The electron is free to move through the crystal in the conduction band, and will do so until it encounters an ionized activation site. When this occurs the activator site and electron form a neutral configuration. It is possible that this has its own set of excited levels, and the de-excitation of the configuration to its ground state can be in the visible region. The mean lifetime of the decay of these configurations is the characteristic physical phenomenon that determines the time resolution of the detector, since the migration times are typically much shorter.

This mechanism means that the emitted photons are of a different frequency to the absorbed ones (no self-absorption), and also that with careful choice of doping material, the emitted photons are in the visible spectrum. This leads to higher light yields and consequently better energy resolutions.

However, γ rays are not charged particles, and so cannot directly interact with the detectors in the manner described above. Instead, a γ-ray will interact with the detector crystal through one of three processes:

- Photoelectric effect
- Compton scattering
- Pair production

These interactions transfer energy from the γ ray to an electron, accelerating it through the detector crystal. This fast electron is the charged particle that is detected, as described above.

3.1.3 Energy measurement

The number of photoelectrons produced by a γ ray is, in essence by conservation of energy, proportional to the energy of the γ ray. Thus, counting the total number of photons produced allows an energy measurement to be made. The major source of error in this energy measurement is from the statistical fluctuations that are Poisson in nature. This means that the higher the number of photoelectrons produced per MeV of deposited energy for a particular crystal, the better the energy efficiency.

3.1.4 Time measurement

A timing measurement is made by “picking off” a constant fraction of the leading edge of the detector pulse. Thus the slope of the leading edge (determined by the lifetime of the de-excitation process τ) and the total number of photons per MeV, N determines the timing resolution. A good indicator of the time resolution is the ratio τ/N.

A comparison of common scintillator detectors is shown in Table 3.1

Material	N (ph/MeV)	τ (ns)	τ/N (ps MeV)	References
$LaBr_3$(Ce)	63000	23	0.37	[Ilt+06]
NaI(Tl)	38000	230	6.1	[HLM88]
CsI(Tl)	65000	680	11	[Val+93; Mos+97]
BaF_2	1400	0.6	0.4	[Lav+83; NBH97; Dor+93]

Table 3.1: A comparison of some common crystal scintillator materials and their efficiency and timing characteristics. A small τ/N gives an indication of a better time-resolution [Akb15].

3.2 Semiconductor Diode Detectors

Semiconductor diode detectors are a second class of detector that is often used in γ-ray spectroscopy. These are commonly found as *High Purity Germanium* (HPGe) detectors, and will be the focus of this section.

As in scintillator crystals, the electronic structure is characterized by conduction and valence bands, separated by an energy known as the *bandgap*. Similarly to the scintillator, a valence band electron can gain energy and be excited into the conduction band. If this occurs and an electric field is present, the electron-hole pair will drift in opposite directions, parallel to the applied field. This creates a current through the crystal, which can be measured and manipulated to form a pulse which corresponds to a detected particle. As described in Section 3.1.2, the γ ray interacts with electrons in the crystal which are the charged particles detected.

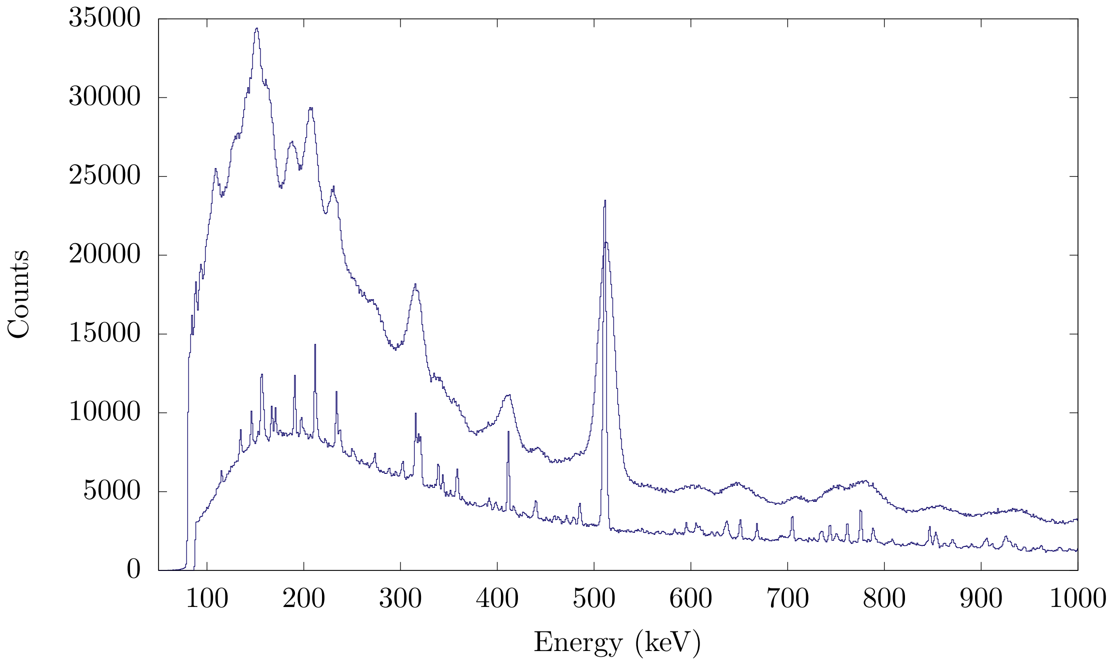

Figure 3.2: The HPGe spectrum (lower) has far superior energy resolution and peak to background ratios than the $LaBr_3$ scintillator spectrum (above). Many of the peaks in the $LaBr_3$ spectrum can be resolved into several separate components using the HPGe detector.

3.2.1 Energy measurement

The energy resolution of HPGe detectors is notably far superior to that of scintillators. This can be seen in Figure 3.2. The higher resolution is due to the fact that electron-hole pairs are detected directly as opposed to relying on a relaxation and photon emission process which introduces statistical spread in the linewidth of a single γ-ray energy.

3.2.2 Timing Measurement

In comparison to scintillator detectors, the time resolution of HPGe detectors is poor. The charge collection process is relatively slow, and this means that the pulses obtained have slow rise times, which has a negative effect on the timing characteristics of the detector [Kno00].

Moreover, there is a large degree of variability in the pulse shapes from event to event, that causes further losses in time resolution [Kno00; QMO69]. The timing resolution of HPGe detectors using conventional electronics is typically ~ 10 ns [MBP07; Cre+10]. Thus HPGe detectors are limited in their application to TDPAD measurements. For example the attempt by Regan et al. to measure the Larmor precession of ^{107}Cd in gadolinium ($T_L = \pi/\omega_L \sim 10$ ns) with HPGe detectors did not succeed [RSA95].

A more detailed discussion of the concepts introduced here can be found in [Kno00].

4

Experimental Methods

4.1 Experimental Setup

The experimental setup consisted of four scintillator detectors, located at ±45° and ±135° with respect to the beam line. A HPGe detector was positioned at $\sim 90°$ to the beam for a high energy-resolution reference, see Fig. 4.1. For preliminary experiments, detectors 2 and 3 were BaF_2 detectors, and coincidence events between detectors 1 and 4, and 2 and 3 were measured. However, this proved of limited value due to the lower efficiency and energy resolution of the BaF_2 detectors. Consequently, in later experiments detectors 2 and 3 were replaced with $LaBr_3$ detectors.

A magnetic field of $\sim$ 0.08 T was applied to the target in the vertical direction (i.e. perpendicular to the page in Figure 4.1). Mu-metal shielding of the scintillators was necessary to prevent stray fields from accelerating slow electrons in the first stages of the photomultipliers. Previous to implementing the shielding, the gain of the photomultiplier changed as the stray field changed direction. This effect could be seen from the changes of the energy spectra as the external magnetic field changed direction. Both the target chamber and the front half of the detectors were shielded, which eliminated the stray fields and minimized the consequent gain shifting.

The HPGe detector provided a high energy-resolution reference, which is invaluable in identifying contaminants that are unable to be resolved by the lower energy-resolution $LaBr_3$ detectors. The timing information from this detector was recorded but not used to determine precessions. It was, however, used to project γ-ray spectra corresponding to different time regions with respect to the beam pulse.

The target chamber and associated hardware is known as the Hyperfine Spectrometer. It consists of a high-vacuum chamber around the target that can be cooled to temperatures of $\sim$ 6 K. The target is held directly in front of the beam line, with magnetic coils above and below providing an external magnetic field to magnetize the ferromagnetic target layer

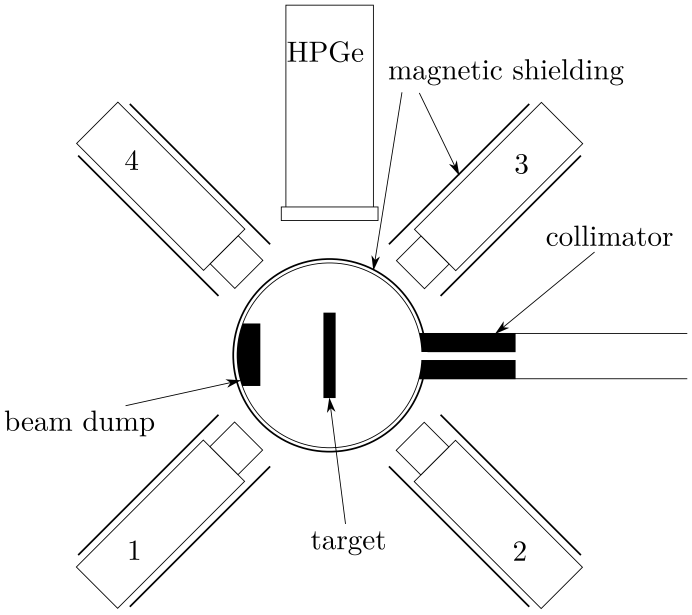

Figure 4.1: Detector setup for TDPAD measurement with four scintillators and one HPGe detector.

in the vertical plane. The direction of the magnetization can be reversed by changing the direction of the current flow in the magnet coils. There is a collimator that is towards the outside the chamber, and a lead beam dump which absorbs any beam past the target. Fig. 4.2 shows a cut-away view of the hyperfine spectrometer.

4.2 Electronic Setup

The electronics schematic is shown in Figure 4.3.

4.2.1 Description of Electronics Modules

In this section the function of the individual modules is described. The following section will describe their functions in the TDPAD measurement.

ORTEC Timing Filter Amplifier (TFA)

The Timing Filter Amplifier shapes the timing pulse from the HPGe detector in preparation for a Constant Fraction Discriminator. This can optimise the signal-to-noise ratio and help obtain better time resolution by shaping the signal to optimize time resolution at the expense of energy resolution.

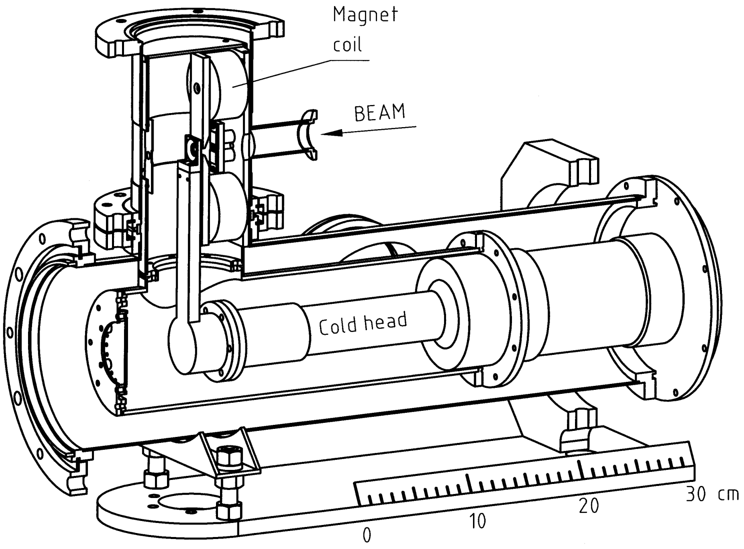

Figure 4.2: A cut-away view of the ANU Hyperfine Spectrometer, showing the target chamber, cooling system and magnetizing coils.

ORTEC Constant Fraction Discriminator (CFD)

The Constant Fraction Discriminator determines the precise time at which a constant fraction of the timing pulse is surpassed and returns a sharp logic pulse corresponding to this time. The CFDs can accept anode signals directly from the photomultiplier bases.

Phillips Scientific 755 OR

This logical OR gate returns a NIM logic pulse when any of the input signals have a NIM logic pulse.

ORTEC Gate and Delay Generator (GTDG)

The Gate and Delay Generator delays and shapes any incoming logic pulse by an adjustable delay time.

ORTEC 567 Time to Amplitude Converter (TAC)

The Time to Amplitude Converter functions as a stop-watch, starting on one pulse and stopping on another, returning a unipolar pulse, the height of which corresponds to the time between the start and stop. These modules form the basis of the timing circuits for this experiment – with sub-nanosecond precisions they are suitable for fast-timing measurements. The specification sheet quotes the time resolution FWHM as $< 0.01\%$ of the full scale $+5$ ps. The strobe triggers the output and resets the TAC to be ready for another start pulse after a start-stop cycle.

Phillips Scientific 711 Six-channel Discriminator

The discriminator gives a sharp NIM output pulse every time a fixed voltage level on the input is exceeded. It functions to clone the RF sync, which signals the arrival of a beam pulse.

4.2.2 Setup for TDPAD measurement

The arrangement of the electronics for data acquisition shown in Fig. 4.3 will now be described. The beam is pulsed with reference to a radio frequency (RF) signal, which is used as the stop on the TAC modules. There were four TAC modules used for the preliminary experiments – a Scintillator TAC (SC TAC), a Germanium TAC (GE TAC), a monitor or beam-γ TAC (BG TAC), and a γ-γ TAC (GG TAC) used to collect γ-γ coincidence data in the preliminary experiments.

The scintillator TAC starts whenever any of the four scintillator detectors detect a γ ray; a 755 OR module taking inputs from the four scintillators provides the start, and the stop input is from the RF pulse. The TAC module measures a time which corresponds to the time between the beam pulse and decay of the nucleus.

Similarly the germanium TAC measures equivalent information, taking its start from the HPGe detector and its stop from RF also.

The strobe pulses for each of these TACs are provided by any event – an OR gate taking inputs from every detector. This OR gate also provides the master gate (MG) trigger – a pulse which begins a time window during which the data acquisition system will record data. The veto pulse is a manual override to inhibit the master gate, stopping any data from being collected. The veto is active while the magnetic field is changing direction so that no data is collected during this time when the field direction is indeterminate.

The γ-γ TAC was only used in the preliminary experiments to collect timing information for coincidence events between detectors 1 and 4 and detectors 2 and 3. This starts on an event from either detector 2 or 3 (for the preliminary experiments, BaF_2 detectors), and stops on a pulse from either 1 or 4 ($LaBr_3$). However, in post-experimental analysis, it was clear that the rate of coincidences was too low to obtain any useful information, and so this was removed in the final experiment.

The monitor or beam-γ TAC served as a live monitor to determine the time and shape of the beam pulse with respect to the RF pulse. It starts on an event from detector 2, and stops on the RF pulse. The output is not recorded in the data acquisition system, but is sent to a `kicksorter` program, which displays a live histogram of the data in 4096 channels on the accelerator control panel. This allows the beam to be monitored and adjusted to keep the FWHM of the pulse as small as possible. The location of the pulse with respect to the RF can also be kept constant by monitoring this TAC.

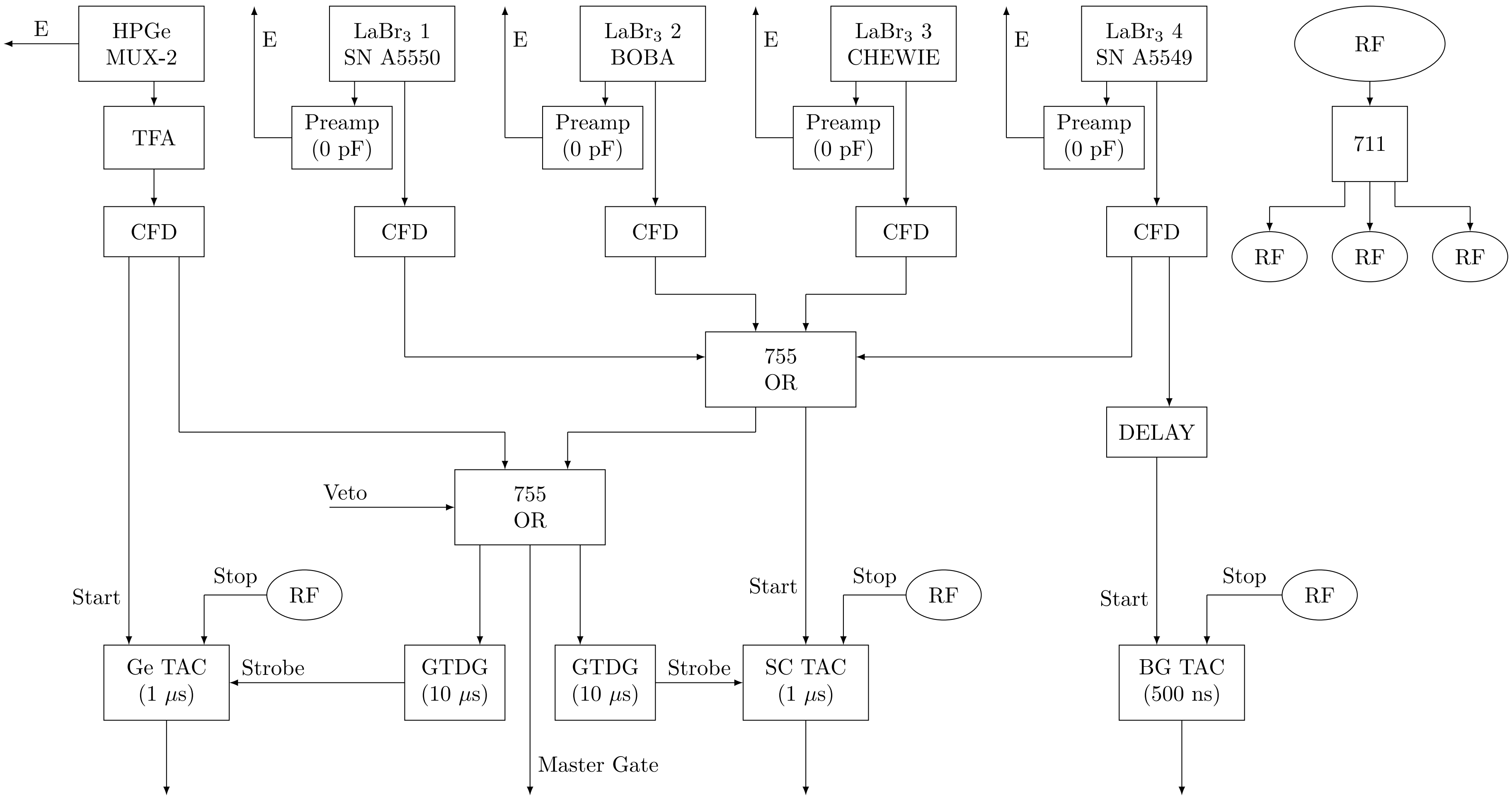
HPGe
MUX-2
E
TFA
CFD
LaBr$_3$ 1
SN A5550
E
Preamp
(0 pF)
CFD
LaBr$_3$ 2
BOBA
E
Preamp
(0 pF)
CFD
LaBr$_3$ 3
CHEWIE
E
Preamp
(0 pF)
CFD
LaBr$_3$ 4
SN A5549
E
Preamp
(0 pF)
CFD
RF
711
RF
RF
RF
755
OR
DELAY
Veto
755
OR
Start
Stop
RF
Ge TAC
(1 μs)
Strobe
GTDG
(10 μs)
GTDG
(10 μs)
Strobe
Start
Stop
RF
SC TAC
(1 μs)
Start
Stop
RF
BG TAC
(500 ns)
Master Gate

Figure 4.3: The electronics diagram for a TDPAD measurement. The TACs are started on a γ-ray detection event, and stopped by the radio frequency pulse. The beam pulsing system is synchronized with the same RF and so this functions as a measurement of the time between when the γ-ray is emitted and when the beam pulse occurs.

4.3 Data Acquisition

Each time the master gate is triggered, the DAQ (**D**ata **A**c**Q**uisition system) records values from the nine ADC channels in use for this experiment. These are listed in Table 4.1. The outputs of each ADC that fires in an event are written to disk so that they can be accessed later and sorted into histograms.

The "FLIP" ADC refers to the magnetic field direction – and is set up so that when the field is "down" a value of 8 (i.e. in channel 8) is recorded in the ADC, and when the field is "up" the value is 64. This enables the field up and field down data to be treated separately in post-experimental analysis.

ADC	Detector	Channels
1	HPGe MUX-2	4096
2	$LaBr_3$ 1	4096
3	$LaBr_3$ 2	4096
4	$LaBr_3$ 3	4096
5	$LaBr_3$ 4	4096
6	Ge TAC	8192
7	SC TAC	8192
8		8192
9	"FLIP"	4096

Table 4.1: The ADC allocations for the ^{107}Cd TDPAD measurement. For the preliminary experiments channel 8 was used for a γ-γ TAC which recorded coincidences between the two $LaBr_3$ detectors (1 and 4) and the two BaF_2 detectors (2 and 3).

5

Data Analysis

5.1 Event by event data

The experimental data obtained from the DAQ is in event-by-event form, each event containing values for each of the nine ADC channels shown in Table 4.1. Note: however, that generally only three ADCs will fire in most events, corresponding to a γ-ray detector, its associated TAC, and the field direction. The first stage of data analysis is to sort this event-by-event file into either 1D or 2D histograms (matrices). Each histogram channel represents a particular value (or pair of values) from the one or two ADCs, for example the energy of the HPGe detector. The contents of the histogram channel are then the number of events that have occurred with that particular ADC value (or pair of values), i.e. the number of γ rays detected that have a particular energy.

The sorting also involves a filtering process known as “gating”, whereby conditions are imposed on each event to determine its inclusion or exclusion in the histogram. For example, to form the energy spectrum of $LaBr_3$ detector 1, with the field down we sort a histogram of ADC channel 2, gating on ADC channel 9 between the values 7 and 10. Thus only the events with ADC channel 9 between 7 and 10 (field down) are included as the histogram is formed. We could also impose a timing condition by gating additionally on some values in ADC 7, or require that only $LaBr_3$ detector 1 has fired by excluding any events that have non-zero values in ADC channels 1, 3, 4, or 5.

For the purposes of TDPAD, eight matrices were sorted, one for every $LaBr_3$ detector/field-direction combination, requiring additionally that only a single scintillator has fired. This last requirement comes from the fact that there is a single TAC for all four scintillators – if a double, triple, or quadruple event occurs, it is impossible to determine which of the detectors started the TAC. Since the electronics are different for each detector, the channel which corresponds to the beam pulse is different for each detector. For single-detector events this can be adjusted for (see Section 5.2), however, if the detector that triggered the TAC is unknown, this adjustment is impossible.

By summing over different energies, a 1D time projection histogram can be obtained. Typically sums are taken between upper and lower energy bounds, which correspond to the upper and lower limits of a particular transition. This is also known as “gating” on the transition, as it is equivalent to the process outlined above. The gating process process allows the timing characteristics of particular energy transitions (or more generally energy regions) to be determined. A background subtraction is achieved by taking the difference of the histogram obtained by gating on the energy peak and the histogram obtained by gating on a nearby peak-free region, scaled by an appropriate constant. See Fig. 5.1 for an illustration of this concept.

In the context of TDPAD, this yields eight 1D time histograms, each corresponding to a field direction and detector for a single transition. Before adding these together, they must be aligned to account for any systematic differences in delay times as a result of cable path lengths or minor differences in electronics.

5.2 TAC spectra alignment

To account for any systematic differences in the time-spectra positions, a precise and consistent physical reference point must be used. The natural choice is the beam pulse, and to determine its position in the time spectra a transition which is purely prompt (i.e. has no isomeric components) must be found. An arbitrary channel number is picked as a reference, and each matrix is shifted such that the prompt (beam pulse) peak of the reference transition is centred at that particular channel. For example, for the case of ^{54}Fe, the 1016-keV transition (from the 1016-keV first excited 2^+ state in the ^{68}Ge produced by the 2p reaction channel) fulfills this criterion. For each of the eight matrices, a 1D time histogram is formed by gating on the 1016-keV transition. These are all (approximately) Gaussian distributions, and the number of channels needed to shift the centroid of the Gaussian to channel 3540 is recorded. These same shifts are then applied to the matrices, aligning them and accounting for any systematic differences.

This process can also be applied to account for slow drifts of the beam pulse position with respect to the RF. By sorting the data into several spectrum files (each containing a certain number of consecutive records), the drift of the beam pulse can be identified and corrected for. This alignment is vital to obtaining the high time-resolution that is necessary to resolve fast precessions. It should be stressed that these measurements are pushing the limits and are about an order of magnitude faster than the time regime usually studied in γ-ray spectroscopy (with HPGe detectors) in the ANU Laboratory (and elsewhere).

Once alignment shifts have been applied for every section of the sorted data, all the corresponding histograms in every section can be added together. This results in eight aligned matrices which contain data from the entire experiment.

5.3 Time and energy calibrations

Energy calibrations were carried out separately for each detector/field-direction combination using ^{60}Co, ^{152}Eu, and ^{137}Cs sources placed outside the target chamber. The calibration was assumed to be linear – whilst this is not strictly the case for the $LaBr_3$ detectors, small

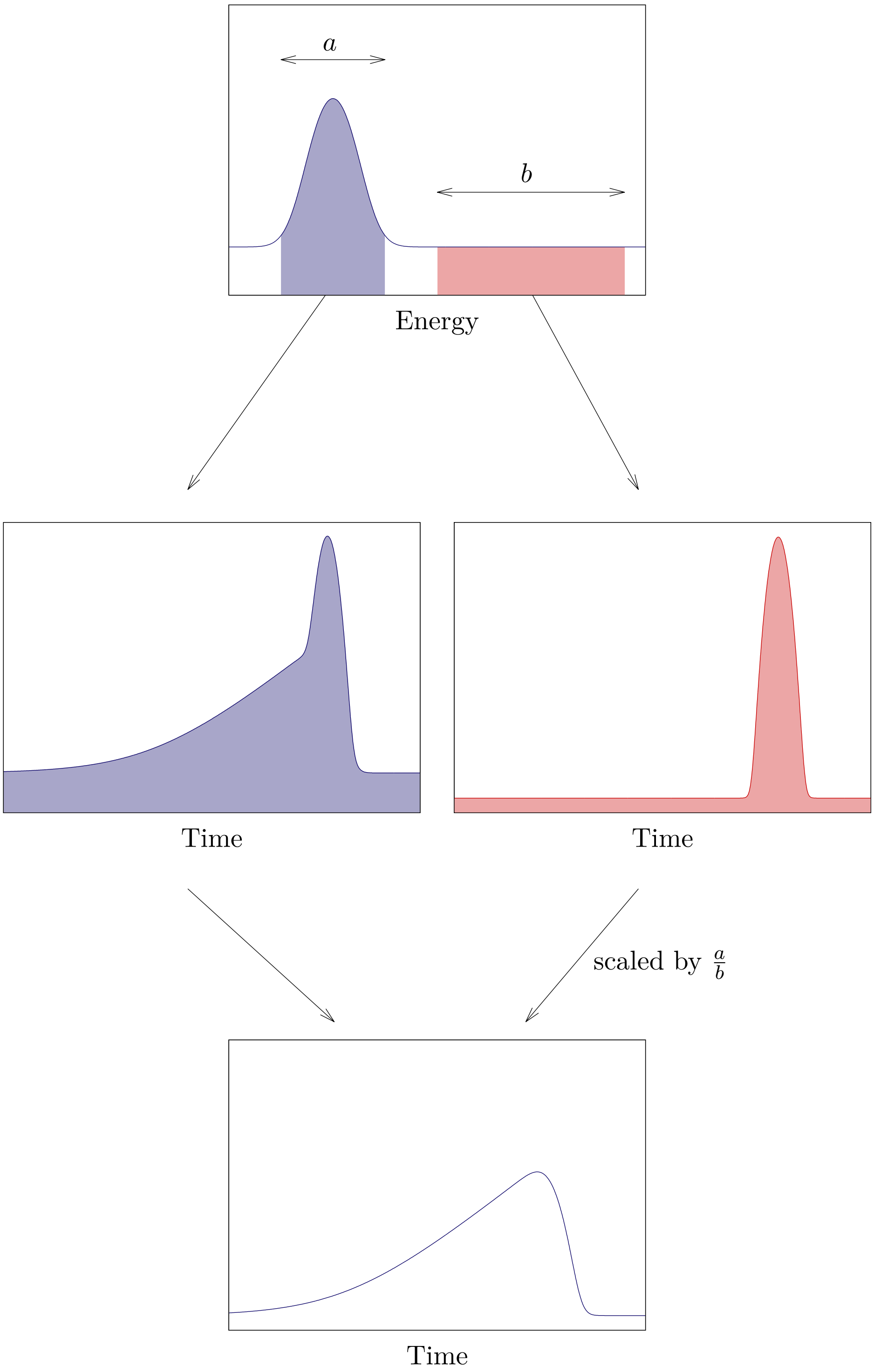
a
b
Energy
Time
Time
scaled by $\frac{a}{b}$
Time

Figure 5.1: An illustration of the process of random background subtraction. A region with no peaks close to the peak of interest is considered (shaded red). The time spectrum found by projecting this region is subtracted from the time spectrum obtained by projecting the peak region, after scaling appropriately.

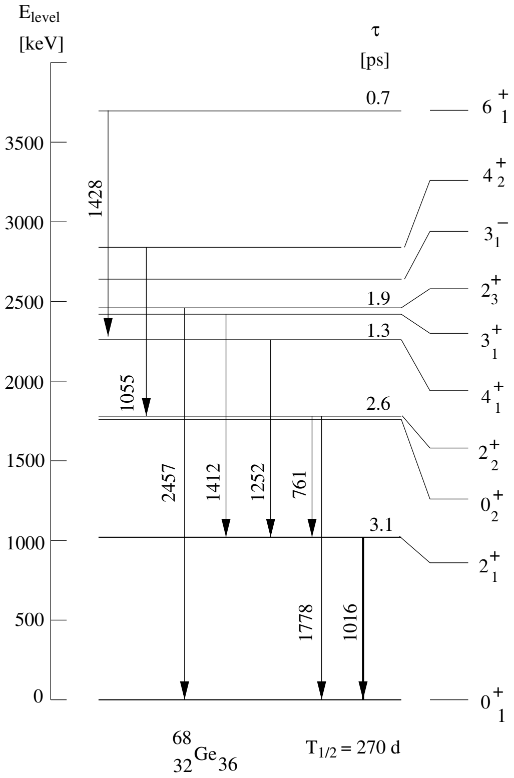

Figure 5.2: Partial level scheme for the ^{68}Ge which is produced in the ^{58}Ni(^{12}C, 2p) reaction with the ferromagnetic host layer of the target. The first excited 2^+ state decay is used to align the different matrices [Les+05].

nonlinearity is not significant for the purposes of this experiment; since the level schemes for each case are well known, it is not important to determine energies precisely.

5.4 Ratio function

The gating and background subtraction processes discussed in Section 5.1 corresponding to the transition depopulating the isomer of interest can be applied to the aligned and summed matrices. This gives eight 1D time histograms, corresponding to every detector/field-direction combination. Since the angular distribution is symmetric with respect to 180° rotations, opposite detectors have equivalent time spectra (for the same field direction). Similarly, detectors which are separated by 90° have equivalent angular correlation behaviour for opposite field directions. Thus, the eight histograms are summed into two groups: detector 1 field up, detector 2 field down, detector 3 field up, and detector 4 field down forming the first group, and the four remaining detectors forming the second. An example the two groups of summed spectra is given in Figure 5.3. The two histograms have two notable components; exponential decay that shows the lifetime of the relevant state, and oscillations corresponding to the precession of the state. The oscillations in each histogram are out of phase with those in the other histogram. Consequently, a ratio function can be formed,

$$R(t) = \frac{N_1 - N_2}{N_1 + N_2}, \tag{5.1}$$

where N_1 and N_2 are the first and second histograms, respectively. As has been shown, $R(t) \approx \cos(2\omega_L t)$. Thus determining the frequency of the oscillation in the ratio function allows for an evaluation of the Larmor precession frequency [Cer74].

Since background subtracted spectra are needed, and the background subtraction process introduces errors, a more effective ratio function can be formed. If T_1 and T_2 represent raw (not background subtracted) spectra, and P_1 and P_2 the background subtracted equivalents, the ratio function

$$R(t) = \frac{T_1 - T_2}{P_1 + P_2} \tag{5.2}$$

is equivalent to Equation 5.1, but with less error. This is because the subtraction of the raw spectra in the numerator carries out an effective background subtraction. Of course, errors have to be propagated according to the usual rules as described in Section 5.7 below.

5.5 Autocorrelation functions

An autocorrelation function compares a function with itself at a later time τ. It is defined as

$$X(\tau) = \lim_{T\to\infty} \frac{1}{T} \int\limits_0^T f(t)f(t+\tau)dt \tag{5.3}$$

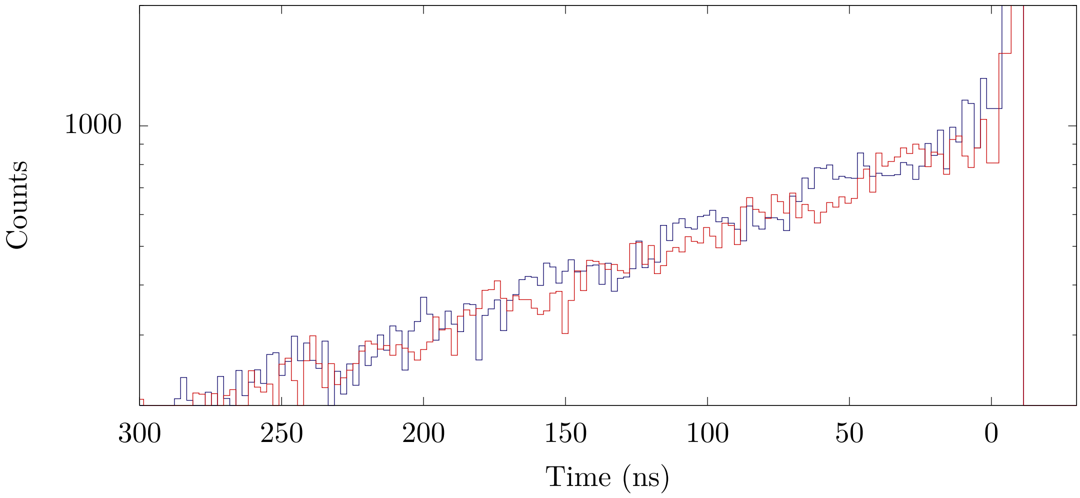

Figure 5.3: An example of time spectra obtained by summing spectra from different detectors after alignment. The oscillations due to nuclear precession can be seen as well as the exponential decay.

for a continuous function [Geo01]. For a pure cosine input function f, the autocorrelation X is also a cosine. Whilst phase and amplitude information is lost (the phase of the autocorrelation is 0, the amplitude corresponds to the degree of correlation), a cosine with even very significant noise will be much clearer in the autocorrelation. In the case where f contains multiple frequencies, each frequency with their relative amplitudes are preserved in the autocorrelation function. See Appendix A for examples and derivations.

When applied to a discrete histogram, the autocorrelation function between channels k_1 and k_2 becomes:

$$X(n) = \sum_{k=k_1}^{k_2-n} \frac{x_k x_{k+n}}{k_2 - k_1 - n + 1} \Bigg/ \sum_{k=k_1}^{k_2} \frac{x_k^2}{k_2 - k_1 + 1} \ . \tag{5.4}$$

This formula can be applied to any section of the ratio function to determine frequency components that are present. In many cases, even if the oscillation is difficult or impossible to observe directly in the ratio function, the autocorrelation function will clearly show the presence of oscillations. Autocorrelations are especially useful for analysis of states with long lifetimes. In these cases the number of counts for any single channel may be low, but with many counts spread over a large time period due to the long lifetime. An autocorrelation combines many channels in the calculation of each data point, thus using more information and improving the statistical significance of each point.

5.6 Fourier transforms

The Fourier transform decomposes a signal into its sine-wave components. It is especially useful in this context to identify the contributing frequencies, and to determine the presence of minor frequencies in ratio or autocorrelation functions. It is defined as:

$$\hat{f}(\omega) = \int_{-\infty}^{+\infty} f(x) e^{-ix\omega} dx, \tag{5.5}$$

for a continuous function. For a discrete histogram, the Discrete-time Fourier Spectrum (DTFT) is formed by,

$$\hat{f}(\omega) = \sum_{n=-\infty}^{\infty} x_n e^{-i\omega n}. \tag{5.6}$$

To form a Discrete Fourier Transform (DFT), the DTFT is sampled an arbitrary number N times. Taking the magnitude of the complex DFT, we find an N channel histogram showing the relative amplitudes of frequencies present in the original data.

5.7 Error Analysis

The error in a (raw) histogram bin containing N counts is assumed to be $\sqrt{N}$. Similarly, for a peak containing T counts, we have $\sigma_T^2 = T$. If there is a background under the peak of B_p, then this is estimated by scaling from an equivalent neighbouring region of the spectrum with number of counts B (see Figure 5.1). Thus $B_p \approx sB$, where s is the relevant scaling factor which corrects for the width in channels of the region of interest and possibly also any difference in background height under the peak region compared to that in the neighbouring background region. The error in the area of the background subtracted peak $P = T - sB$ is $\sigma_P^2 = T + s^2B$. Note that if s is small, the error introduced by background subtraction can be minimized.

Since every channel of a 1D TAC spectrum is formed by a background subtraction of the relevant energy peak, this process can be used to calculate the errors in the TAC spectrum bin counts. Mathematically, if $T(t)$ is the (time) histogram formed by gating on the energy peak, $B(t)$ the spectrum formed by gating on the background region, and s the relevant scaling factor, then

$$
\begin{aligned}
P(t) &= T(t) - sB(t), && (5.7)\\
\sigma_T(t)^2 &= T(t), && (5.8)\\
\sigma_B(t)^2 &= B(t), && (5.9)\\
\sigma_P(t)^2 &= T(t) + s^2B(t), && (5.10)
\end{aligned}
$$

where $P(t)$ is the background subtracted spectrum.

5.7.1 Ratio Function

Equation 5.2 gives

$$
\begin{aligned}
\left|\frac{\partial R}{\partial T_1}\right| &= \frac{1}{P_1 + P_2}, && (5.11)\\
\left|\frac{\partial R}{\partial T_2}\right| &= \frac{1}{P_1 + P_2}, && (5.12)\\
\left|\frac{\partial R}{\partial P_1}\right| &= \left|(T_1 - T_2)\frac{1}{(P_1 + P_2)^2}\right|, && (5.13)\\
\left|\frac{\partial R}{\partial P_2}\right| &= \left|(T_1 - T_2)\frac{1}{(P_1 + P_2)^2}\right|, && (5.14)
\end{aligned}
$$

such that

$$
\sigma_R^2 = \left(\frac{\partial R}{\partial T_1}\sigma_{T_1}\right)^2 + \left(\frac{\partial R}{\partial T_2}\sigma_{T_2}\right)^2 + \left(\frac{\partial R}{\partial P_1}\sigma_{P_1}\right)^2 + \left(\frac{\partial R}{\partial P_2}\sigma_{P_2}\right)^2, \qquad (5.15)
$$

which gives the error in the ratio function $R(t)$.

5.7.2 Autocorrelation Function

Equation 5.4 gives

$$X(n) = A/B, \tag{5.16}$$

with

$$A = \sum_{k=k_1}^{k_2-n} \frac{x_k x_{k+n}}{k_2 - k_1 - n + 1}, \qquad B = \sum_{k=k_1}^{k_2} \frac{x_k^2}{k_2 - k_1 + 1}. \tag{5.17}$$

However, since B is independent of n and only functions as a normalization factor to ensure that $X(0) = 1$, the error of B is not included in the analysis. Thus, taking B as a constant,

$$\frac{\partial X}{\partial x_i} = \frac{1}{B}\frac{\partial A}{\partial x_i}, \tag{5.18}$$

where i is a channel number between k_1 and k_2. So then we calculate

$$\frac{\partial A}{\partial x_i} = \frac{1}{k_2 - k_1 - n + 1}\left(\sum_{k=k_1}^{k_2-n} \frac{\partial x_k}{\partial x_i} x_{k+n} + x_k \frac{\partial x_{k+n}}{\partial x_i}\right). \tag{5.19}$$

Now since the errors in separate channels are independent,

$$\frac{\partial x_j}{\partial x_i} = \delta_{ij}, \tag{5.20}$$

where δ_{ij} is the Kronecker delta function. Thus the sums in equation 5.19 reduce to two terms, leaving

$$\frac{\partial A}{\partial x_i} = \frac{x_{i+n} + x_{i-n}}{k_2 - k_1 - n + 1} \tag{5.21}$$

where $x_j = 0$ if $j < k_1$ or $j > k_2$. The error in the autocorrelation function $X(n)$ is then found by summing over all the histogram channels i:

$$\sigma_X^2(n) = \sum_{i=k_1}^{k_2} \left(\frac{\partial X}{\partial x_i}\sigma_{x_i}\right)^2. \tag{5.22}$$

Note that 5.18 and 5.21 give the first term in the product, and σ_{x_i} is the error in the ith channel of the original histogram; in this case given by the error in the ratio function.

6

Preliminary Experiments

Preliminary experiments were conducted, primarily to "shake down" technical problems and establish the validity of the system and experimental setup. Three cases with known *g* factors, and on which TDPAD measurements had been successfully made in identical or similar experiments previously, were chosen for these measurements. The purpose was not necessarily to make original measurements, but rather to establish the effectiveness and applicability of $LaBr_3$ scintillators to the TDPAD method in-beam, which to our knowledge has not been done before.

6.1 Ge in iron

The first experiment used the ^{nat}Fe(^{16}O, 2pn) reaction to populate excited states in both ^{69}Ge and ^{67}Ge. These precess with long periods ($\sim$ 50 ns), and therefore serve as good cases to "shake down" the setup without pushing the timing limits of the $LaBr_3$ detectors. At the same time it allows an assessment of the energy resolution and effectiveness of the $LaBr_3$ detectors.

The target was held at a temperature of $\sim$ 6 K throughout the measurement, allowing a new measurement of the strength of the hyperfine field of Ge in iron at low temperature. The only previous measurement is at room temperature [LRR91].

6.1.1 Target

The target used was a natural iron foil rolled to 5.09 mg/cm^2, and annealed at $\sim$ 780 °C. The annealing process aligns the crystal structure of the metal foil to ensure saturation of the foil is reached with minimum external field applied. Natural iron contains $\sim$ 92% ^{56}Fe and $\sim$ 6% ^{54}Fe, on which the reactions take place. The single iron foil acts as both the target for the reaction and the ferromagnetic host.

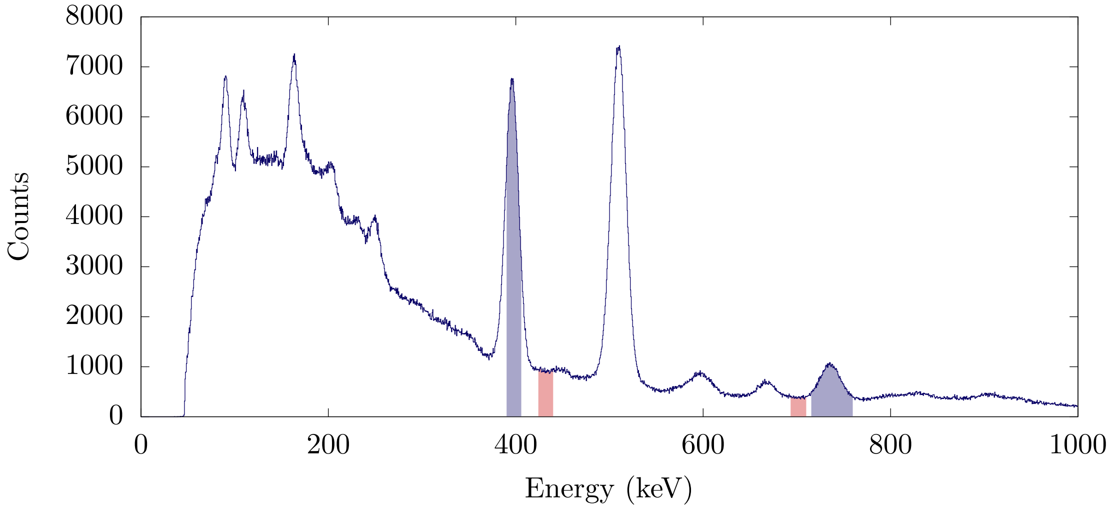

Figure 6.1: Out-of-beam energy spectrum from the ^{nat}Fe(^{16}O, 2pn) reaction. Blue shaded areas are the peaks of interest and red shaded areas the background subtraction regions.

6.1.2 ^{69}Ge in iron

The state of interest is the first-excited $\frac{9}{2}^+$ isomer, with an excitation energy of 398 keV. The state has a mean lifetime $\tau = 4060(70)$ ns, and a g factor of $g(\frac{9}{2}^+) = -0.2224(7)$ [Chr+70; Fuj+83]. It depopulates via a 398-keV γ ray. The experiment uses a 60-MeV beam and the ^{56}Fe(^{16}O, 2pn)^{69}Ge reaction. TDPAD has been used to measure the $\frac{9}{2}^+$ isomer in iron before, finding a precession period of $T_L = 43.7(3)$ ns at room temperature [LRR91].

Results

The energy spectrum obtained by one of the LaBr$_3$ detectors is shown in Figure 6.1. The summed time spectra are obtained by gating on the 398-keV peak and projecting the TAC information. These are shown in Figure 6.2, and an independent lifetime measurement of the $\frac{9}{2}^+$ isomer has been obtained. The lifetime obtained, $\tau = 3740(30)$ ns, is not in agreement with the literature values of $\tau = 4030(90)$ ns [Fuj+83], or $\tau = 4100(100)$ ns [Chr+70], which will be discussed below.

The ratio function obtained from these time spectra is shown in Figure 6.3. Weak oscillations are visible for ~ 1 μs after the prompt, this is explained by the long lifetime of the state: the long lifetime means that the total counts obtained are spread over a large number of channels, the effect of which is to reduce statistics and make it more difficult to discern the oscillations visually in the ratio data. However, it also allows an autocorrelation to be taken over a long time period. The autocorrelation function taken for ~ 1 μs after the prompt is shown in Figure 6.4. This clearly shows a single precession with period $T_L = 41.7$ ns, corresponding to a Larmor frequency of $\omega_L = 75.4(1)$ Mrad/s. The amplitude of the ratio function is also consistent with [LRR91; Lee88].

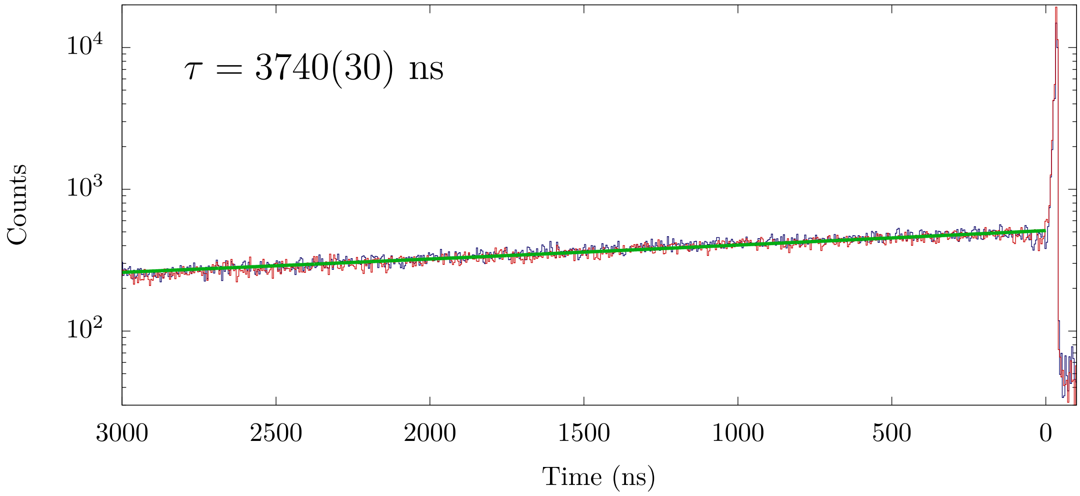

Figure 6.2: Time spectra gating on the 398-keV transition. Red and blue lines represent different groups of (in phase) histograms, see Section 5.1. The green line represents a fit to the data giving $\tau = 3740(30)$ ns. This is not in agreement with other values measured, however, the TAC range is too short to accurately determine the background level, and this accounts for the discrepancy.

6.1.3 ^{67}Ge in iron

The case of ^{67}Ge implanted into an iron host is similar to the previous ^{69}Ge case. The same data set was analysed, but looking at the ^{54}Fe(^{16}O, 2pn)^{67}Ge reaction. The 734-keV transition depopulates a $\frac{9}{2}^+$ isomer ($E_x = 752$ keV), with a similar g factor to that in ^{69}Ge, but with a much shorter lifetime of $\tau = 211(6)$ ns [Cha+00]. TDPAD has been used successfully on this state before, determining a $T_L = 51.4(6)$ ns [LRR91].

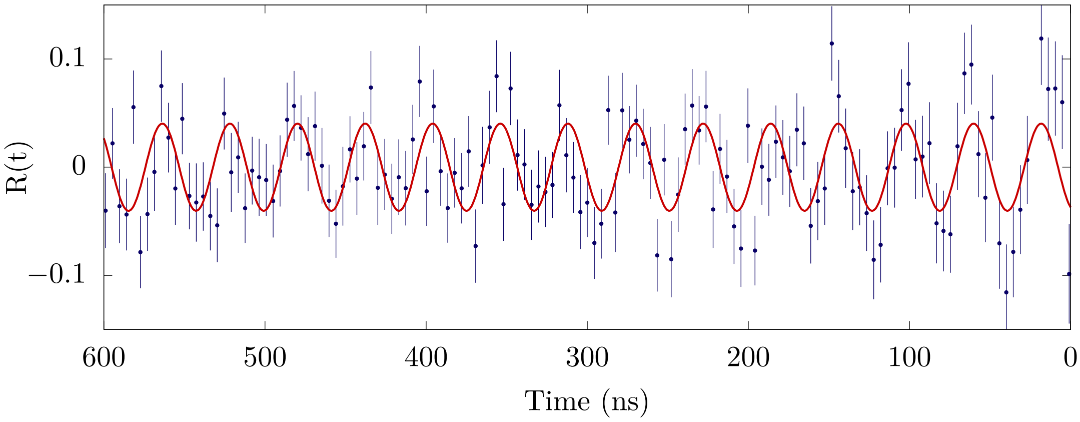

Figure 6.3: Ratio function formed from the spectra shown in Figure 6.2, i.e. for the 398-keV transition depopulating the $\frac{9}{2}^+$ isomer in ^{69}Ge . Oscillations are barely visible, however the amplitude of the ratio function is consistent with that previously observed [LRR91].

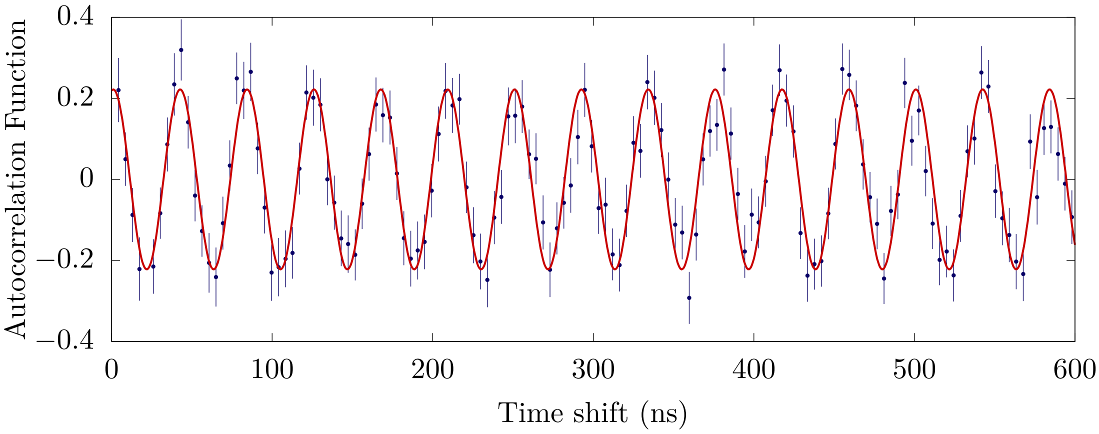

Figure 6.4: Autocorrelation function of the ratio function for the 398-keV ^{69}Ge $\frac{9}{2}^{+}$ isomer 1 μs after the prompt. Oscillations are clearly visible.

Results

The relevant gates and background subtraction regions for the 734-keV isomer are shown in Figure 6.1. The time spectra obtained are shown in Figure 6.5, and lifetime measurements have been made from these data to obtain $\tau = 169(2)$ ns. This does not agree with the previously measured $\tau = 211(6)$ ns [Cha+00], $\tau = 160(2)$ ns [AlN+79], $\tau = 147(14)$ ns [Nak+78], or $\tau = 101(10)$ ns [Ber+73]. A previous but never published measurement at the ANU using HPGe detectors is shown in Figure 6.6. The fitted lifetime gives $\tau = 155(3)$ ns. It is clear that there is much disagreement in the literature about the lifetime, and the value of $\tau = 169(2)$ ns is within the range of previous experiments. The shorter lifetime has the effect of concentrating the counts in fewer histogram bins than in the ^{69}Ge case, meaning that the ratio function more clearly shows the precession (Figure 6.7). The amplitude of the ratio function similar to that found in [LRR91; Lee88]. However, as in the previous case, taking an autocorrelation over a relevant time period after the prompt peak results in a cleaner oscillation. The precession oscillation period observed is 49.1 ns, corresponding to a Larmor frequency $\omega_L = 64.0(4)$ Mrad/s.

6.1.4 Discussion

These two cases establish the applicability of LaBr$_3$ detectors to the TDPAD method. Whilst the frequencies resolved are not beyond the limits of HPGe detectors, and TDPAD has been used in these cases previously using NaI(Tl) detectors [LRR91], the experiment successfully resolved the precession frequencies expected.

The Larmor frequencies obtained disagree with those presented in [LRR91]. This is due to the temperature-dependent nature of the hyperfine field B_{hf}. The previous measurements were conducted at room temperature [LRR91], however in the present experiments the target is cooled to ~ 6 K in the Hyperfine Spectrometer. Considering the ratio

$$\frac{g(^{67}\mathrm{Ge})}{g(^{69}\mathrm{Ge})} = \frac{\omega_L(^{67}\mathrm{Ge})}{\omega_L(^{69}\mathrm{Ge})}, \tag{6.1}$$

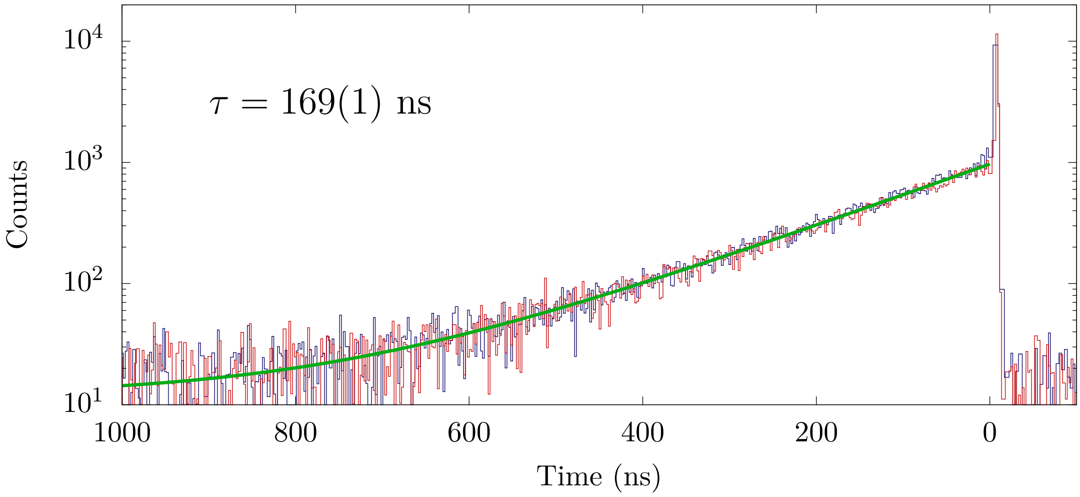

Figure 6.5: Time spectra formed by gating on the 734-keV transition. Red and blue lines represent different groups of (in phase) histograms, see Section 5.1.

this can be used as a reference for agreement that is independent of B_{hf}. The ratio obtained from [LRR91] is 0.85(1), which agrees extremely well with the ratio 0.849(5) obtained from the experiments conducted as part of this work.

The known g factor of the ^{69}Ge isomer allows us to calibrate the hyperfine field B_{hf} at low temperature. Using equation 2.32, we determine that $B_{hf} = 7.08(1)$ T for temperatures below 20 K. This compares with the previously measured 6.0(2) T at 300 K [RSR78]. The higher hyperfine field at low temperatures is to be expected given that the magnetization of the ferromagnet increases at lower temperatures [Boz93]. At 300 K, $T/\theta = 0.288$ ($\theta = 1043$ K, the Curie temperature of iron), and referring to Figure 6.9 we note there is a significant increase in magnetization as the temperature drops to ~ 6 K, where $T/\theta \approx 0.006$. Whilst the hyperfine field does not follow the magnetization directly, the magnetization of the foil gives a guide as to how the hyperfine field varies [RSR77].

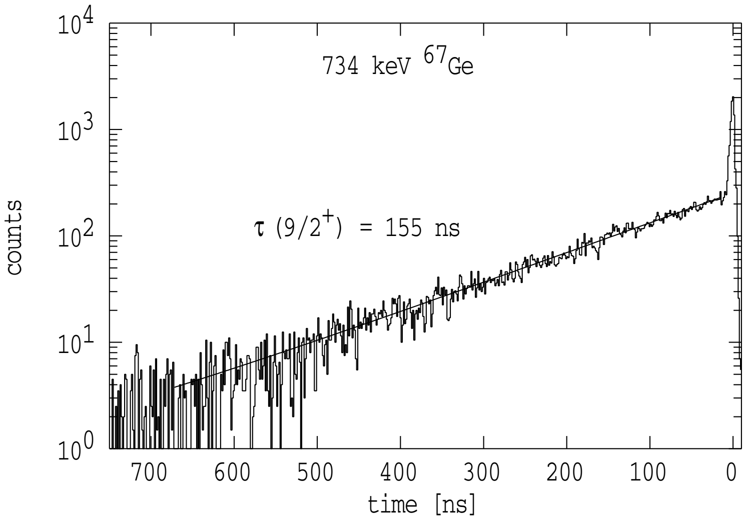

Figure 6.6: A previous lifetime measurement of the ^{67}Ge $\frac{9}{2}^+$ isomer conducted at the ANU using HPGe detectors.

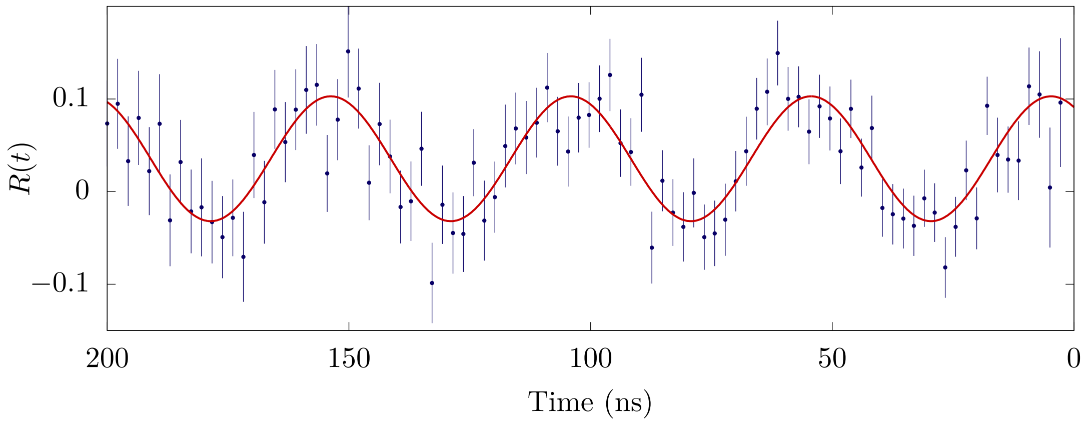

Figure 6.7: Ratio function formed for the 734-keV transition from the $\frac{9}{2}^+$ isomer in ^{67}Ge. Oscillations are present but with significant noise.

The lifetimes obtained for both isomers differ from previous measurements. The ^{69}Ge lifetime is shorter than expected, outside statistical errors. The inaccuracy can be attributed to the inability to determine the background level accurately. The short TAC range means that determining a constant background level in the time spectrum is difficult, and this is likely the cause of the discrepancy. The ^{67}Ge lifetime is longer than other measurements [AlN+79], Figure 6.6. The most likely cause is a subtlety of background subtraction that has not been accounted for. However, making accurate lifetime measurements is not the focus of the present work and since the effect on the ratio function extracted is minimal, the lifetime discrepancies were not pursued. Moreover, lifetimes in agreement with the literature were obtained for other cases described in this thesis. The successful resolution of the precession frequencies clearly shows the ability of the LaBr$_3$ detectors in the current setup to perform the TDPAD method.

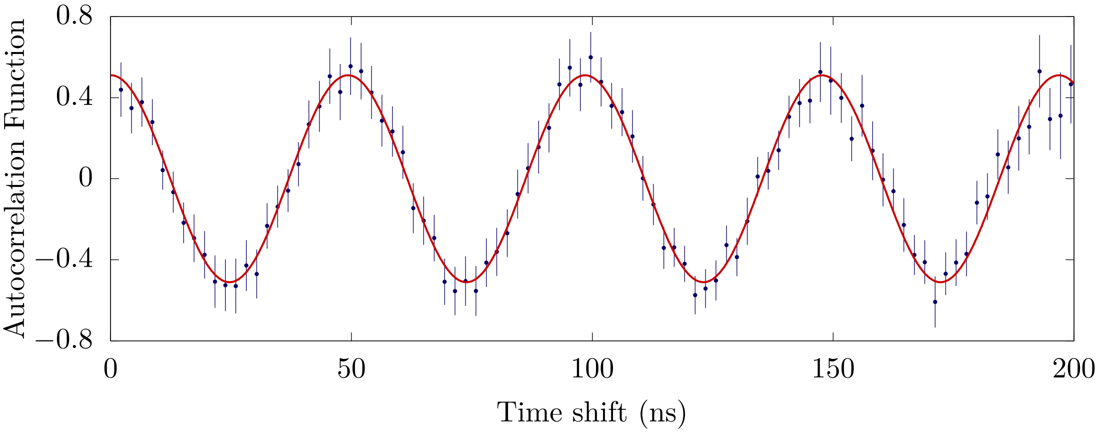

Figure 6.8: Autocorrelation function for the 734-keV transition from the $\frac{9}{2}^+$ isomer in ^{67}Ge. The autocorrelation function is taken over the ratio function to 250 ns after the prompt. Oscillations are clear with a smaller level of noise.

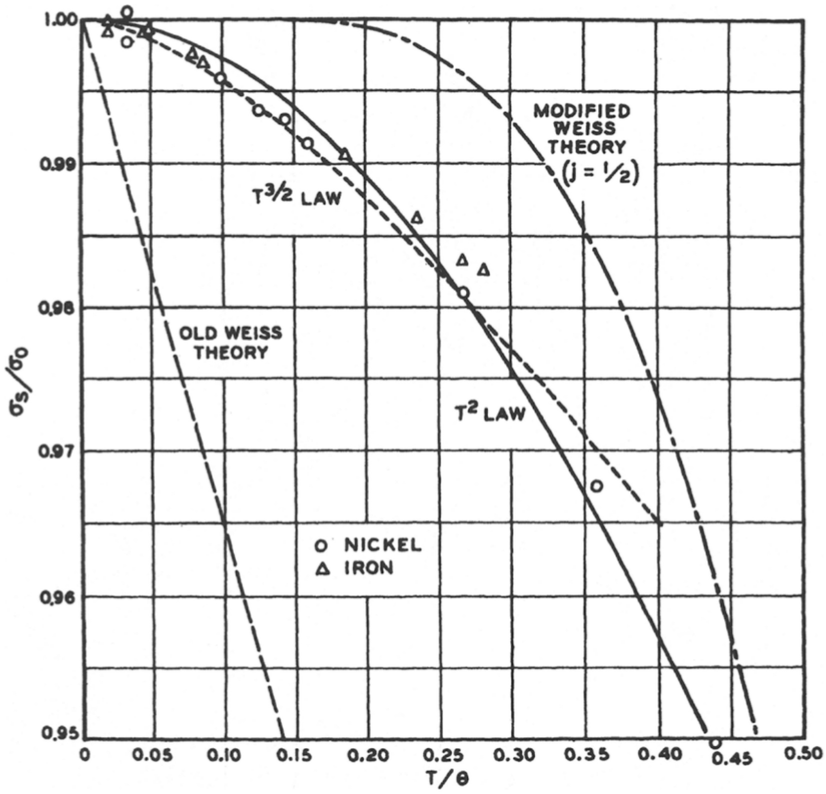

Figure 6.9: The variation of spontaneous magnetization with temperature, showing theoretical predictions and experimental results for iron and nickel [Boz93].

6.2 ^{54}Fe in nickel

The final preliminary experiment was conducted using a 40-MeV beam, with the ^{12}C(^{45}Sc, p2n)^{54}Fe reaction populating an exited state in ^{54}Fe. This reaction and isomer have been studied previously using TDPAD or similar methods [Hen+71; Has+84; Raf+83]. The isomer is a 2.95-MeV, 10^+ excited state that feeds an E2 cascade of 5 γ-ray transitions. In principle, any of these can be used to determine the alignment of the initial isomer, as each intervening lifetime is short in comparison to the precession frequency. The mean lifetime of the 10^+ isomer is $\tau = 525(10)$ ns [Daf+78]. Using the value of the hyperfine field $B_{hf} = -27.00(3)$ T [Kra83], we calculate an expected precession period of $T_L \approx 3$ ns. Note that this is approaching the limit of the experimental setup, whilst the time resolution of the LaBr$_3$ detectors is adequate (better than 0.5 ns), the beam-pulse system is limited to $\Delta t \sim 2$ ns. Thus, this is a good case to explore the limits of what is achievable with the present pulsing system of the 14UD accelerator.

6.2.1 Target

The ^{45}Sc forming the first layer of the target was evaporated onto a nickel foil to a thickness of 0.76 mg/cm^2. The foil was a 2.44 mg/cm^2 piece of nickel, annealed at ~ 790 °C.

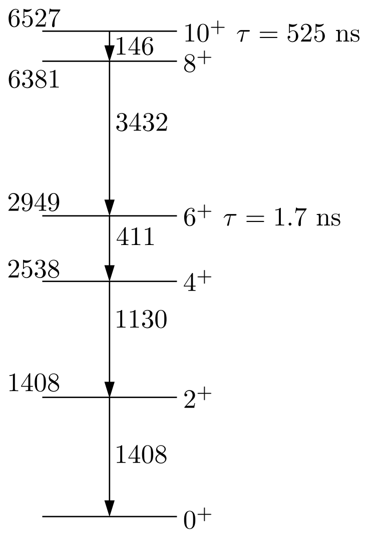

Figure 6.10: Partial level scheme for ^{54}Fe showing the stretched E2 cascade that can be used to measure precessions in the 10^{+} isomer. Excitation and transition energies are in keV.

6.2.2 Results

The energy spectrum obtained can be seen in Figure 6.11. The transition used to adjust for the beam drift was the 1016-keV transition from the 1016-keV first excited 2^{+} state in ^{68}Ge, produced in the 2p reaction channel on the ^{58}Ni in the ferromagnetic host layer of the target. This has a lifetime of 3.00(16) ps [Lüt+12; Les+05; PK82], short enough to be considered entirely in coincidence with the beam pulse and therefore a good probe for the time reference. An example of a typical prompt peak obtained by gating on the 1016-keV transition can be seen in Figure 6.12

The 3432-keV, 411-keV, 1130-keV, and 1408-keV transitions can be clearly observed in

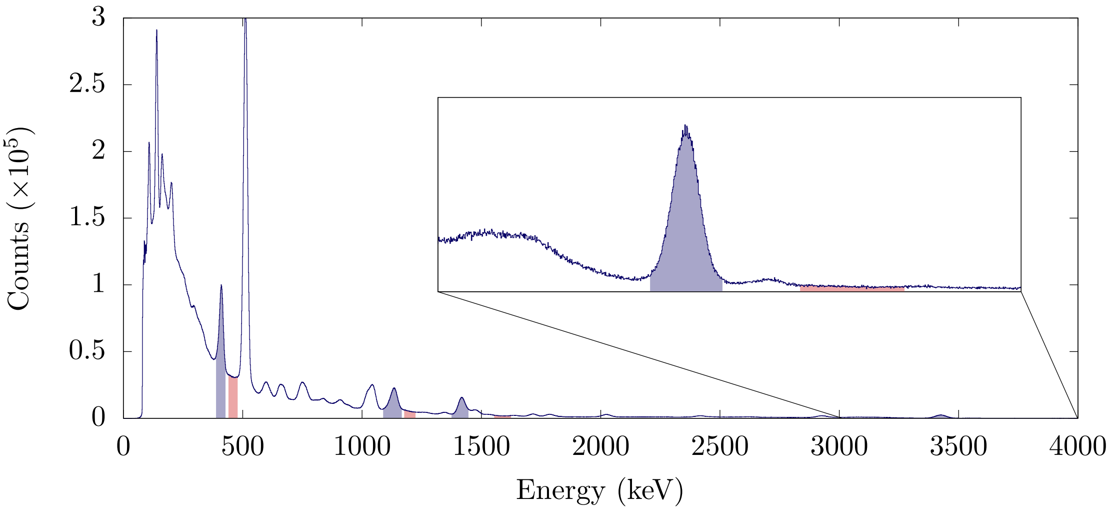

Figure 6.11: Energy spectrum for ^{54}Fe. The blue shaded peaks are the transitions in the cascade from the 10^{+} isomer, and the red shaded areas are the relevant background subtraction regions. The zoomed section shows the 3432-keV transition in more detail.

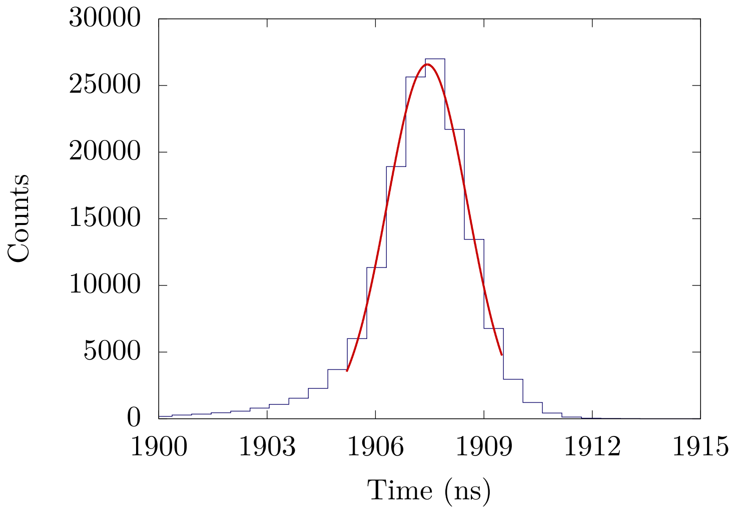

Figure 6.12: A Gaussian is fitted to the prompt peak to obtain the centroid. This is the reference point by which the spectra from different runfiles and detectors are aligned.

Figure 6.11, with the 146-keV transition also present over a significant background. Each of these can be examined separately, and the precession frequencies should be the same in each. The mean lifetime of the 6^+ state has been previously determined to be 1.76(3) ns [Coc+70; SNY71; Hen+71]. The effect of this state on the spectra generated by the lower (411-keV, 1130-keV, 1408-keV) transitions has been calculated by [Raf+83] to be an angular shift and attenuation to the A_2 coefficient, but, importantly, no change to the frequency of oscillation observed.

The time spectra obtained by gating on the four transitions can be seen in Figure 6.13, with lifetime curves fitted. The four values have a weighted average of $\tau = 516(1)$ ns. This is in agreement with previous measurements of $\tau = 525(10)$ ns [Daf+78], and $\tau = 516(45)$ ns [Boz+78].

The ratio functions obtained from each of the transitions are inconclusive, showing no clear oscillations. This is expected – not only is the predicted oscillation at the limit of the timing resolution of the setup, but the lifetime of the isomer is also relatively long, meaning that, as in the ^{69}Ge case, the counts are spread over many histogram bins.

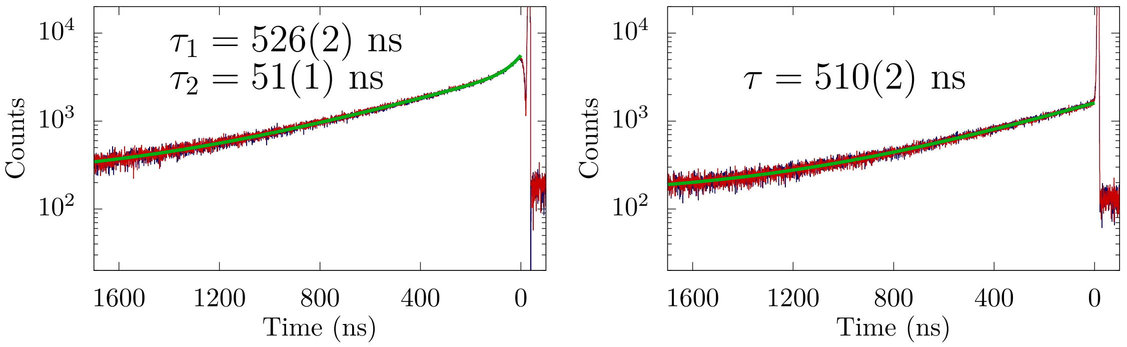

(a) 411-keV transition **(b)** 1130-keV transition

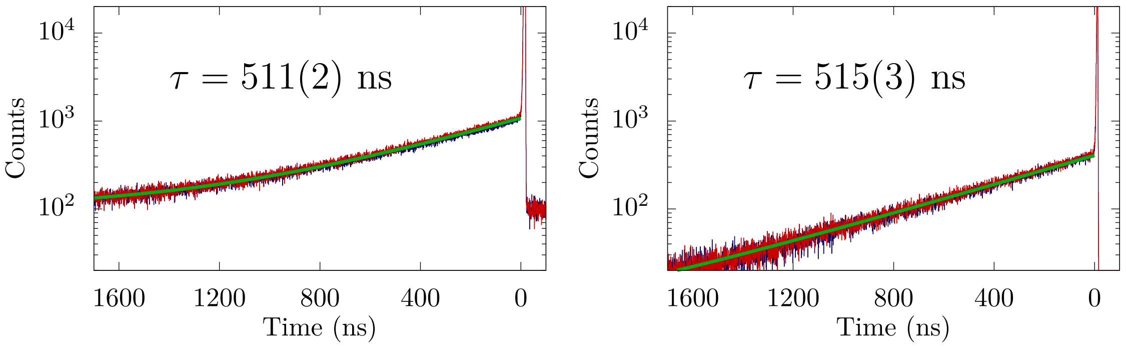

(c) 1409-keV transition **(d)** 3432-keV transition

Figure 6.13: Time spectra for the four cascading transitions from the 10^+ isomer.

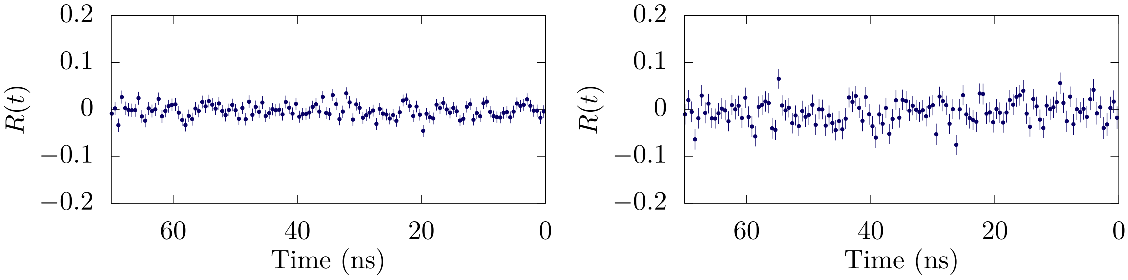

(a) 411-keV transition **(b)** 1130-keV transition

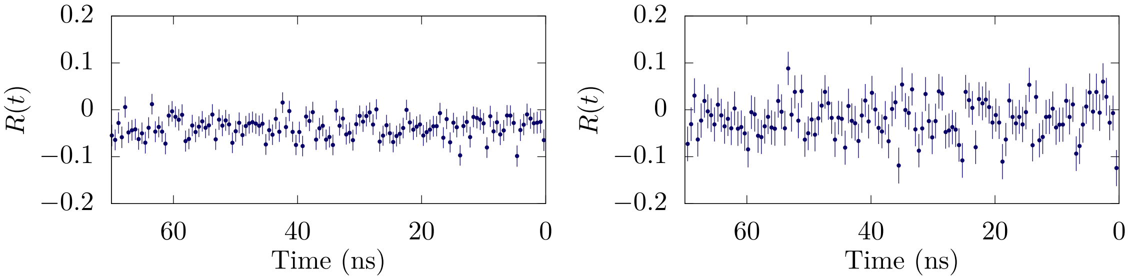

(c) 1409-keV transition **(d)** 3432-keV transition

Figure 6.14: Ratio functions for the four cascading transitions from the 10^+ isomer of ^{54}Fe.

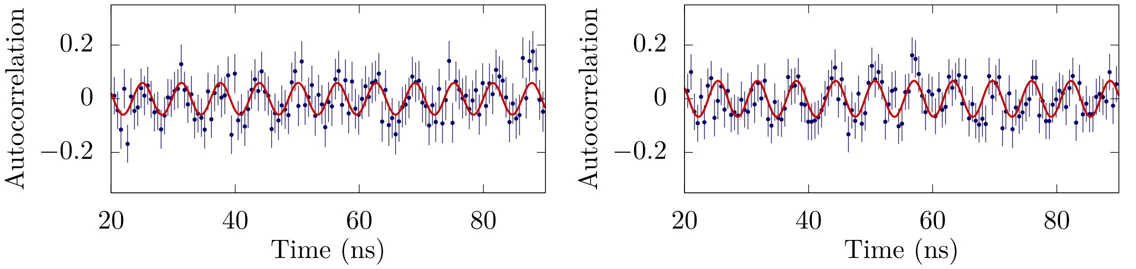

(a) 411-keV transition **(b)** 1130-keV transition

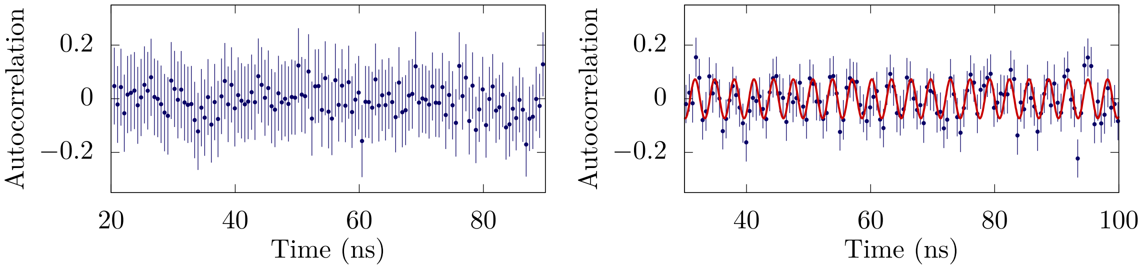

(c) 1409-keV transition **(d)** 3432-keV transition

Figure 6.15: Autocorrelation functions for the four cascading transitions from the 10^+ isomer of ^{54}Fe.

Taking autocorrelation functions over relevant time periods after the beam prompt results in Figure 6.15, which shows the autocorrelations obtained for each of the four transitions. Interestingly, the frequencies present are not the same for each transition. Observing the Fourier transforms of these autocorrelation functions (Figure 6.16), we see that there is a dominant peak corresponding to $T_L \approx 3$ ns in the 3432-keV transition. This is the expected precession, clearly resolved. However, in both the 1130-keV and 411-keV transitions we see a dominant component with $T_L \approx 6$ ns.

The origin of the 6-ns oscillation is unclear. It is possible that the 3-ns oscillation is attenuated somewhat as the cascade progresses, especially by the longer lived 6^+ state. This would explain the lack of a 3-ns oscillation in the three later transitions. However, it fails to explain the presence of the slower oscillation. The only physical explanation for this is a contaminant that is not present in the higher 3432-keV transition. Note in Figure 6.11 that the 3432-keV transition has essentially no contaminants – it is the highest peak in the spectrum and thus above any Compton background from other transitions. However, since the 6-ns oscillation is present in both the 411-keV and 1130-keV transitions, it is very unlikely that both are affected by the same contaminant. Moreover, neither the literature nor the HPGe detector present gives support to other relevant transitions that are close in energy to either 411 keV or 1130 keV. Indeed, the g factor of the 10^+ isomer has been determined by the same reaction and technique, using NaI detectors and the 1130-keV and 1408-keV transitions [Raf+83].

It is possible that the 6-ns oscillation originates from the Compton background that hasn't been properly subtracted. However, performing the same ratio and autocorrelation analysis on the background regions close to the lower energy peaks shows no precession here either, meaning background precession as the cause of the 6-ns oscillations is unlikely.

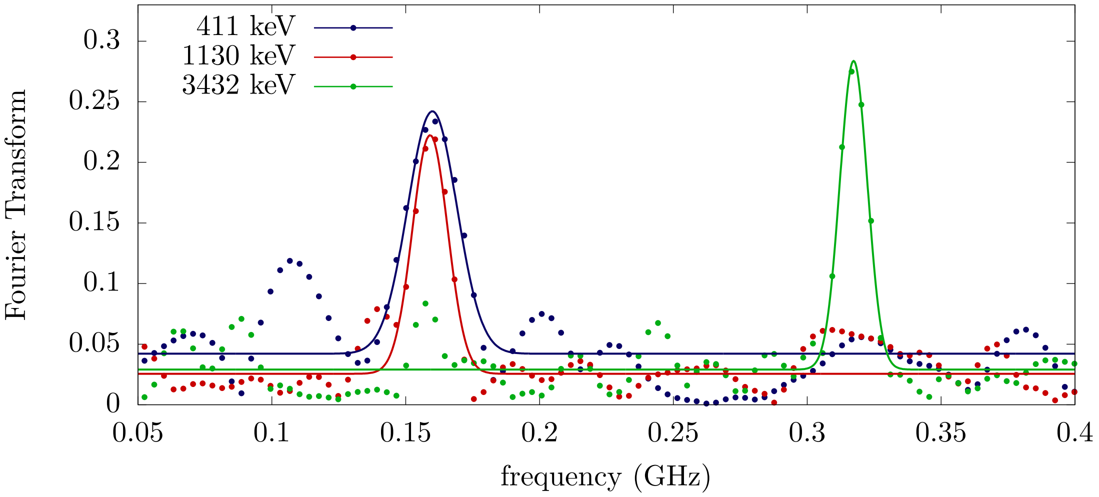

Figure 6.16: Fourier transforms of the autocorrelation functions show peaks corresponding to a 3-ns oscillation in the 3432-keV transition, and a 6-ns oscillation in the 411-keV and-1130 keV transitions.

Another possibility is that the anomalous oscillation is a result of an artifact in the autocorrelation procedure. However, the large amounts of noise present in the ratio functions make it impossible to fit curves to these in any meaningful way, making it difficult to establish whether the 6-ns oscillation is present in the ratio functions of the 411-keV and 1130-keV transitions. Fourier transforms of these ratio functions show no clear peaks.

The 3432-keV transition however clearly shows the expected precession frequency clearly in the autocorrelation function and its Fourier transform. In comparison to data obtained by [Raf+83], the experiment shows the advantages of the $\mathrm{LaBr_3}$ detectors. We were able to resolve a 3-ns precession, in comparison the ~ 5-ns precession previously measured by the use of a non-standard detector and magnetic field orientation geometry to reduce the frequency [Raf+83].

7

^{107}Cd in gadolinium

The discrepancy between the measured g factors of $g(\frac{11}{2}^{-}) = -0.189(2)$ and $g(10^{+}) = -0.09(3)$ in ^{107}Cd and ^{110}Cd, respectively, presents an interesting problem for further investigation [Ber+74; RSA95; Rag89]. Since the most likely source of error is the effective hyperfine field in the implantation process in the ^{110}Cd integral measurement, the ^{107}Cd $\frac{11}{2}^{-}$ isomer can be used as a probe to investigate the internal hyperfine magnetic field via the TDPAD method.

7.1 Target

The host used was a gadolinium foil, rolled to 3.94 mg/cm^2, before being annealed at ~ 770 °C. The foil is 99.9% natural gadolinium. The target material was ^{98}Mo and was evaporated onto the host foil to 280 μg/cm^2. The target was held at ~ 6 K during the measurement.

Using the `PACE4` software package (Projection Angular-momentum Coupled Evaporation Monte-Carlo code)[1], the expected recoil energy of the ^{107}Cd nuclei was estimated. This information was used in conjunction with the `SRIM` program (Stopping Range of Ions in Matter)[2], to calculate the optimal target and backing thickness. A thickness of 4.99 μm (3.94 mg/cm^2) was deemed sufficient for the gadolinium foil, as illustrated in Figure 7.1.

7.2 Excitation Function

Initially, an excitation function was measured to establish the correct beam energy. The reaction of interest is ^{12}C(^{98}Mo, 3n)^{107}Cd. However, it is important that the $\frac{21}{2}^{+}$, 2.679-MeV

---

[1] http://lise.nscl.msu.edu/pace4.html

[2] www.srim.org

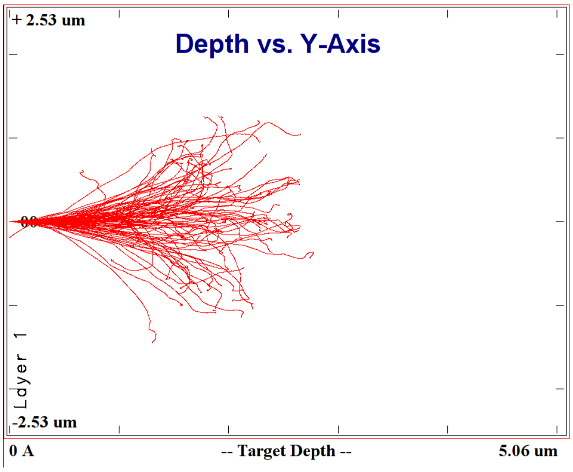

Figure 7.1: Stopping power calculation using `SRIM` shows that a thickness of ~ 5 μm is sufficient to stop the recoiling Cd nuclei.

isomer in ^{107}Cd is not excited strongly – this feeds the lower 845-keV state and if strongly populated, would obscure the precession of the $\frac{11}{2}^-$ state (see Figure 7.2).

Figure 7.3 shows the excitation function data from 42 MeV to 51 MeV in 3 MeV beam energy steps. The 520-keV transition depopulates the $\frac{21}{2}^+$ isomer, and so it is important that this is not excited strongly. The other two transitions shown are from Coulomb excitation of the ^{98}Mo (787-keV), and the prompt 632-keV γ ray depopulating the 2_1^+ state of ^{106}Cd, which is formed in the 4n reaction channel. A beam energy of 48 MeV was decided on as the optimal energy to maximize the excitation of the $\frac{11}{2}^-$ state.

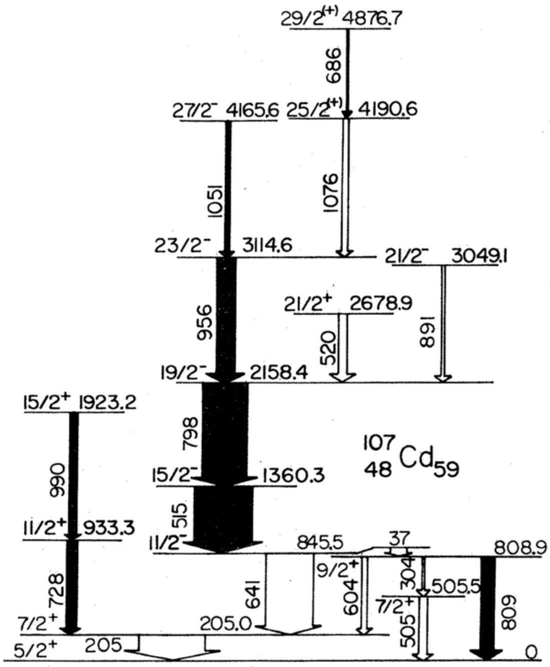
29/2(+) 4876.7
989
27/2- 4165.6
25/2(+) 4190.6
1051
1076
23/2- 3114.6
21/2- 3049.1
21/2+ 2678.9
956
520
891
19/2- 2158.4
15/2+ 1923.2
798
107 48 Cd 59
990
15/2- 1360.3
11/2+ 933.3
515
11/2- 845.5
37
808.9
728
641
9/2+
604
304
505.5
7/2+
7/2+
505
809
205.0
5/2+ 205
0

Figure 7.2: Partial level scheme of ^{107}Cd [Str+78].

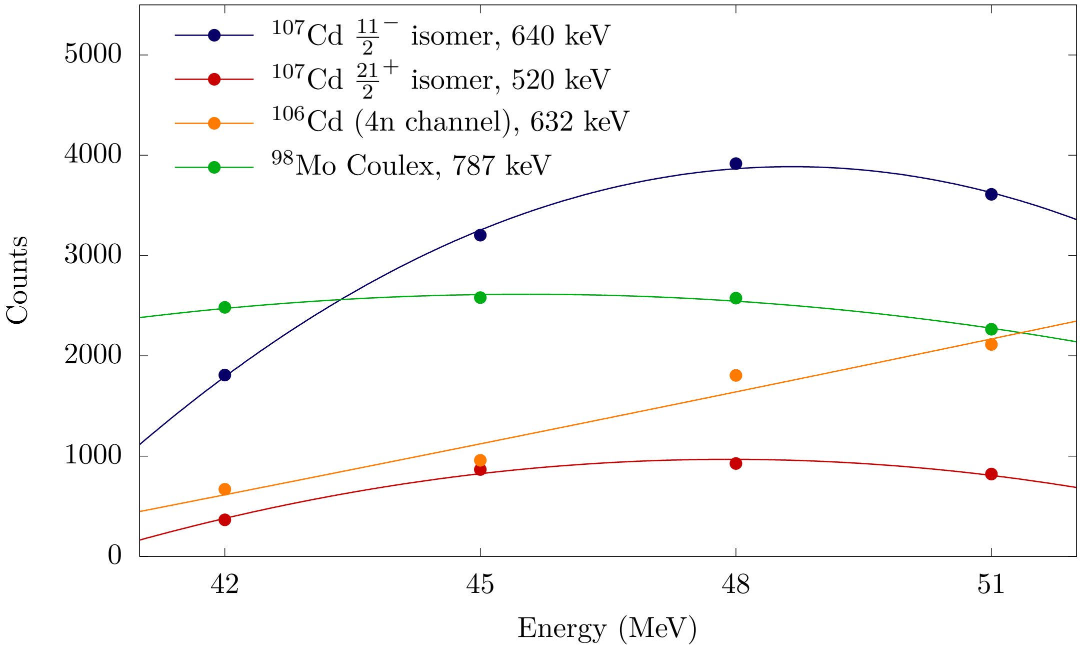

Figure 7.3: The areas of key transition peaks as a function of energy. Maximizing the 640-keV peak whilst minimizing contaminants gives the ideal energy as 48 MeV.

7.3 Results

An example of an energy spectrum obtained is shown in Figure 7.4. The 640-keV transition is clear, showing the population of 845-keV isomer. Figure 7.5 shows a section of the in-beam spectrum, which has a prominent 1633-keV peak. This γ ray is a result of a ^{12}C + ^{12}C $\rightarrow$ ^{20}Ne + α reaction with carbon accumulated on the target or beam dump. The mean lifetime is 1.05(6) ps [Til+88; Ajz87], well shorter than the width of the prompt peak and thus the transition can be considered to have no isomeric component. This is also a relatively clean peak, meaning that although it is the result of a contaminant, it can also be used to adjust for beam drift and timing differences between detectors as outlined in Section 5.2.

Unfortunately, the target chamber geometry means that this process can be less straightforward. The carbon and hence 1.63-MeV γ rays can come from three locations: the collimator, the target, and the beam dump. Since the beam takes a non-negligible time to travel between these three locations, a few cm apart, the γ rays from each are detected at different times relative to the RF pulse. Hence, when projecting the time spectrum from the 1.63-MeV peak, not one but three peaks are seen. These peaks can be observed in Figure 7.6. The presence of three peaks is not a significant problem as their separation depends only on the fixed target chamber geometry, and so the alignment shift can easily be found if the peaks can be distinguished and identified.

The gated and background-subtracted time spectra are shown in Figure 7.7. The decay curve of the $\frac{11}{2}^-$ isomer has been fitted and the mean lifetime found to be 109.7(8) ns. This is in agreement with previous measurements τ = 111(10) ns [Ber+74] and τ = 107(3) ns [RSA95]; it is also within two standard deviations of the other lifetime observed, τ = 97(9) ns [Hag+74]. Some oscillations can be seen in the time spectra, and taking

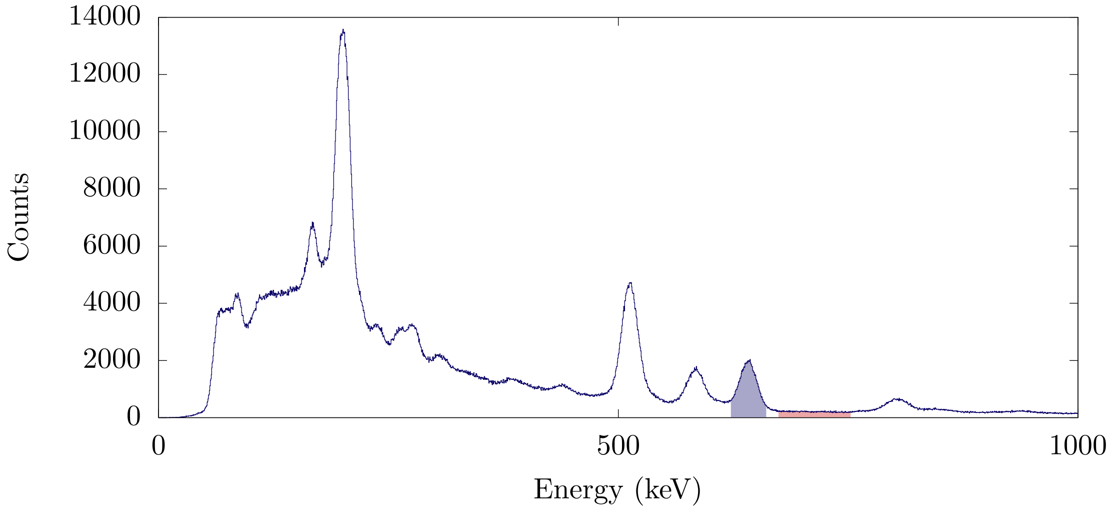

Figure 7.4: The out-of-beam energy spectrum from the ^{107}Cd experiment. The gated 640-keV peak depopulates the $\frac{11}{2}^{-}$ isomer.

the ratio function makes these clear. The oscillations give a Larmor frequency of $\omega_L = 0.262(4)$ Grad/s, however they also decay in amplitude very rapidly. This effect is supported by other literature [FH73], and is discussed in detail in Section 7.4.

7.3.1 Angular Distribution

An angular distribution measurement was also made by placing the HPGe detector at 0°, 25°, 45°, 65°, and 90°. This enables an estimate of the σ/j_i to be found by determining the angular distribution of higher prompt transitions feeding the 845-keV isomer. Angular distributions for both the 956-keV E2 transition and the 798-keV E2 transition were measured. These are shown in Figure 7.9. The fitted σ/j_i values found are 0.32(5) and

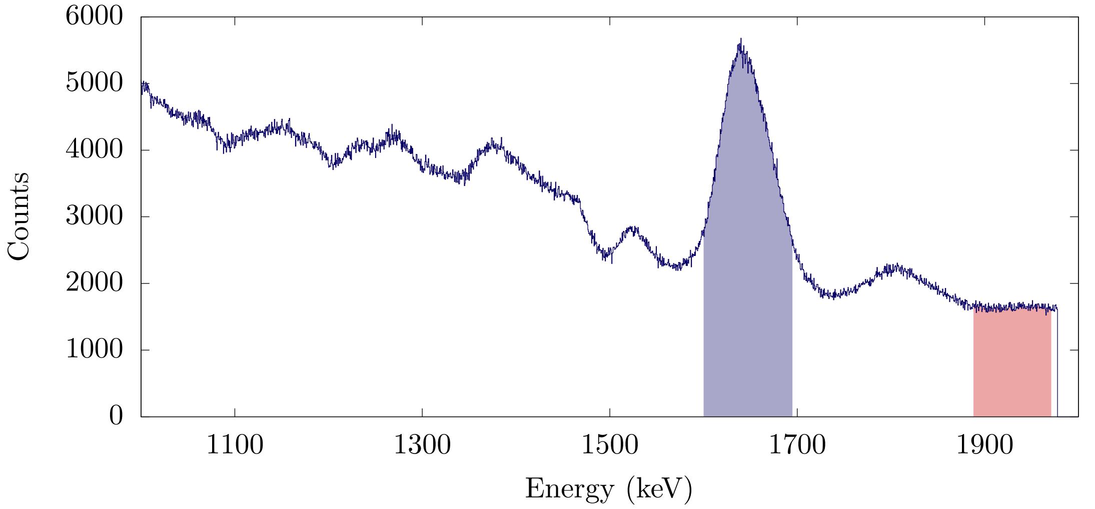

Figure 7.5: The in-beam spectrum shows a peak at 1633-keV which can be used to determine the position of the beam pulse prompt in the TAC spectrum.

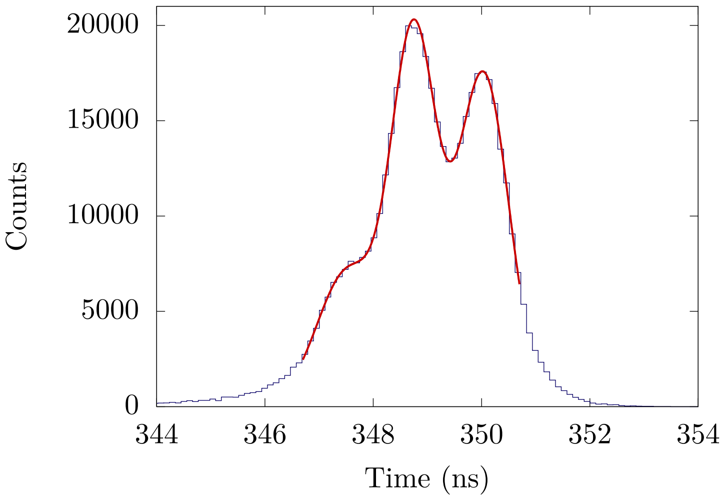

Figure 7.6: Three peaks can be resolved at 347.5, 348.7, and 350.0 ns. These are attributed to γ rays from the collimator, target, and beam dump – the time difference is then the time of flight between the different locations.

0.30(6) respectively, meaning for further calculations $\sigma/j_i = 0.3$ can be assumed. It is worth noting that a $\sigma/j_i \approx 0.35$ is commonly observed in heavy ion reactions like that used here.

7.4 Discussion

7.4.1 ^{107}Cd in gadolinium

The frequency obtained in Figure 7.8 gives $\omega_L = 0.262(4)$ Grad/s, which corresponds to an internal hyperfine field strength of $B_{hf} = -29.7(6)$ T, using equation 2.32. This is not in agreement with the field of $-34.0(7)$ T reported in [Kra83; FH73] for Cd in gadolinium. The

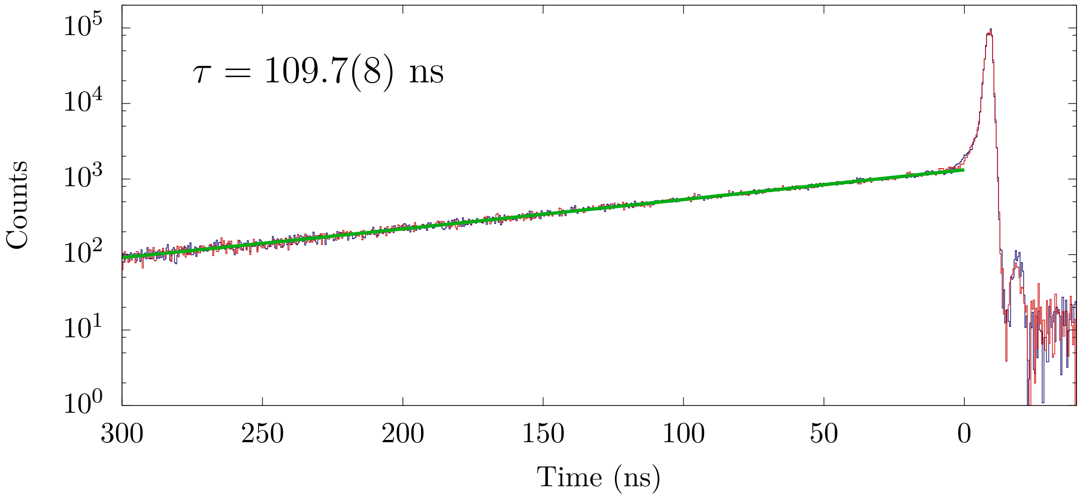

Figure 7.7: Time spectra with fitted lifetime for the 640-keV transition in ^{107}Cd.

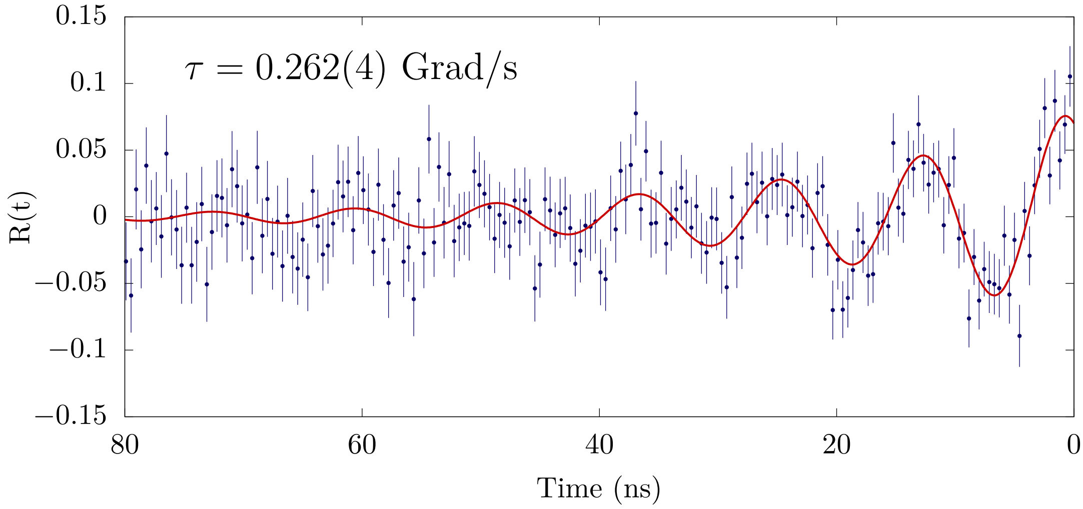

Figure 7.8: Ratio function of the 640-keV transition. Oscillations decay quickly, anisotropy is lost before a single mean lifetime has elapsed. The amplitude of the ratio function is assumed to be exponentially decaying for the purposes of this fit.

difference in hyperfine field is potentially due to minor heating of the target by the beam. The effect of beam heating has not been characterized for this experiment, however in previous measurements on Ni beams near the Curie temperature of gadolinium and terbium hosts, heating on the order of 20 K was inferred. Thus a 20 K increase in temperature is an upper limit for this experiment; the present measurement with a pulsed ^{12}C beam and transmission target must deposit less energy in the target and thus we can be confident that the temperature in the beam spot is below 20 K [Stu+05]. The measurement of $B_{hf} = -34.0$ T was made at 4.2 K [FH73], and as previously discussed in Section 6.1.4, the hyperfine field is a temperature-dependent quantity. The temperature dependence of Cd in gadolinium has been measured by Boström et al. [Bos+71]. However, the observed temperature dependence cannot account for the present results.

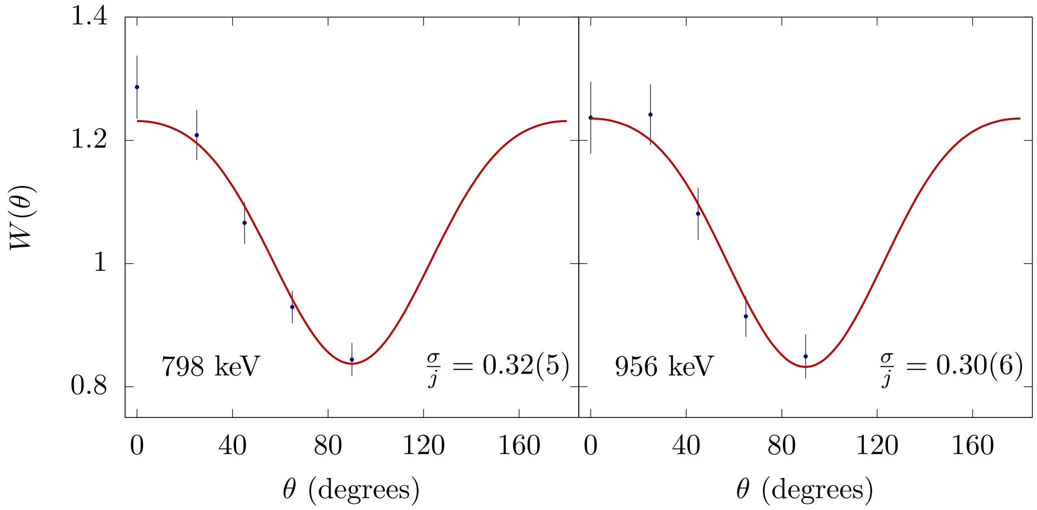

Figure 7.9: Angular distributions for two of the transitions feeding the $\frac{11}{2}^-$ isomer.

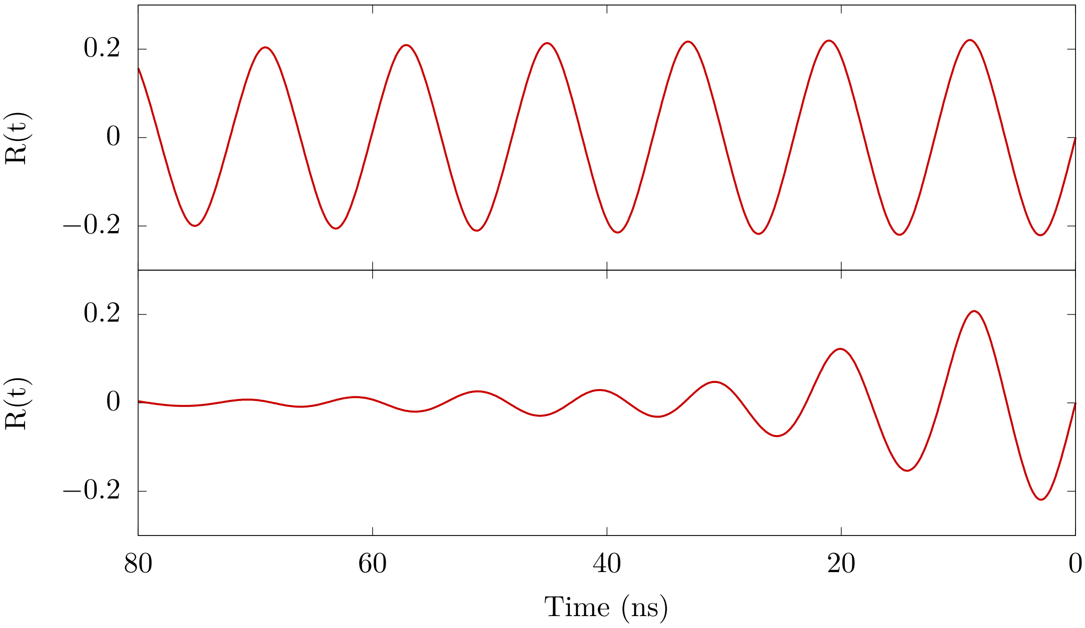

Figure 7.10: Ratio functions simulated for two values V_{zz} are shown. Above, a realistic value ($V_{zz} = 0.85483$) which shows little decay in the oscillations on relevant time-scales. Below, an unrealistically large electric field gradient ($V_{zz} = 8.5483$) is needed to achieve a decay on the time-scale of ~ 40 ns.

At this point it is important to observe that the previous measurements of hyperfine fields were done without an external polarizing field (except to determine the sign of B_{hf}). It is possible in the present work that the internal and external fields are not fully aligned. Such an effect could be studied by measuring the internal field as a function of the strength of the external field. If the internal and external fields are not fully aligned, this would reduce the hyperfine field strength at the implanted nucleus.

The oscillations in the ratio function decay rapidly, and almost completely disappear by ~ 40 ns after the population of the state. This is clearly an effect that is separate from the decay of the state, as this has a lifetime of $\tau = 109.7(8)$ ns. In fact the decay in the A_2 coefficient has been observed in other studies of Cd in gadolinium [FH73], where it was attributed to a combination of electric field gradients, together with a continuous spread in the hyperfine field values, as opposed to a single well-defined field strength.

Figure 7.10 shows calculated ratio functions for the $\frac{11}{2}^{-}$ ^{107}Cd isomer in gadolinium, taking into account the electric field gradient. Simulations for two values of V_{zz} are plotted. The first is a realistic value and shows little decay of the ratio function on relevant time-scales. The second shows a decay of the ratio function in ~ 40 ns, however the strength of the electric field gradient necessary to achieve this shows that the electric field gradient is not the cause of the decaying amplitude. Thus, a continuous spread of hyperfine field values is pursued as an explanation.

In [FH73] a Gaussian distribution of hyperfine field strengths with FWHM $\Delta B_{hf} = 0.5$ T was found. To produce a ratio function that decays as quickly as the experimental data obtained in this work requires a (Gaussian) spread of $\Delta B_{hf} \sim 10$ T. This is not in agreement with the value obtained in [FH73]. We note, however, that the ^{111}Cd impurity

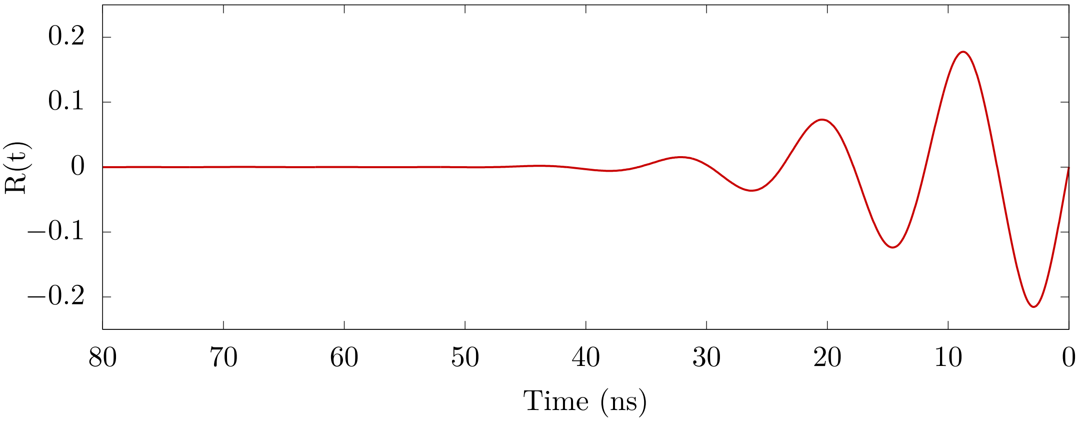

Figure 7.11: A simulated ratio function generated by a continuous Gaussian spread of B_{hf} values with $\Delta B_{hf} = 9.4$ T. The spread achieves damping that is of the same order as what is observed experimentally.

in the gadolinium host in [FH73] was prepared by melting the radioactive source into the gadolinium – as opposed to recoil implantation. Moreover, as previously noted it is possible that in this work the internal and external fields are not completely aligned. This could not only have the effect of reducing the dominant field strength, but also of creating a larger spread in B_{hf} values than measured in the case of [FH73].

Thus the different methods of preparation can account for the larger ΔB_{hf} determined in this work. An example of a theoretical ratio function calculated for $\Delta B_{hf} = 9.4$ T is shown in Figure 7.11.

Notably, the oscillations in the experimental ratio function (Fig. 7.8) have an initial

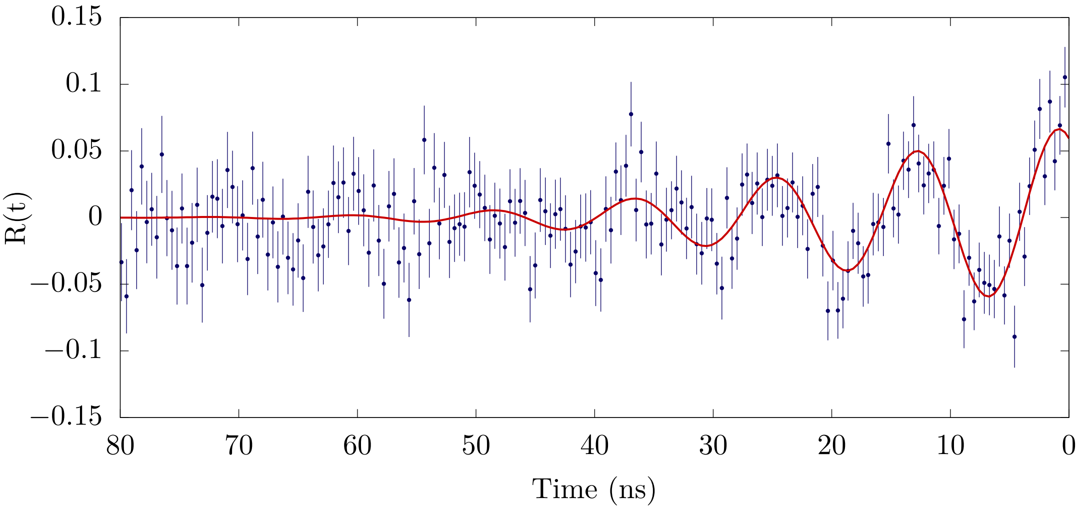

Figure 7.12: The experimental ratio function for the 640-keV transition depopulating the $\frac{11}{2}^-$ isomer in ^{107}Cd, with a fitted ratio function. The parameters of the fit are the (full-field) strength, its spread, and the fraction of full-field implantation sites. It is assumed that all other implantation sites have $B_{hf} = 0$. Note that there is a time offset in this figure compared with the theoretical curves – the true time zero is ≈ -10 ns.

amplitude of ~ 0.1. Comparing this to the theoretical curve in Figure 7.11, it can be seen that the experimental amplitude is much lower than expected. This is explained by the possibility of low-field implantation sites. These have the effect of reducing the initial ratio function amplitude as some fraction of implanted ions are effectively not precessing on relevant timescales. A theoretical ratio function generated by some combination of *two* field sites can be fitted to the experimental data. The field strength at one site is assumed to be is assumed to be 0 T, with the parameters of the fit being the field strength of the other site, the width of its (Gaussian) distribution, and the relative abundances of the two sites in the implantation process. The fitted ratio function can be seen in Figure 7.12. The values from the fit are $B_{hf} = -28.9$ T (the central value), $\Delta B_{hf} = 5$ T, and a proportion of full-field implantation sites $\alpha = 0.34$. However, the α and ΔB_{hf} values can vary significantly whilst achieving a similar quality of fit. (For this reason uncertainties have not been assigned to the fit parameters, which are highly correlated).

7.4.2 ^{110}Cd 10^+ level g factor

The characterization of the implantation process shows that a significant number of implantation sites have low hyperfine fields. This explains the g-factor measurement $g(10^+) = -0.09(3)$ [RSA95] and the discrepancy with the $g(\frac{11}{2}^-) = -0.189(2)$ value [Ber+74; Rag89], and values of $g(\nu h_{\frac{11}{2}^-}) \sim -0.2$ in the Cd isotopes (see Table 8.1). If a significant proportion of implanted nuclei are on low-field sites, the integral measurement will underestimate the magnitude of the true g factor. Since a variety of fitted α values (the proportion of full-field implantation sites) can result in similarly good fits, determining the effective average field for the integral measurement is not possible at this time. Nevertheless, with the above caveat, for illustrative purposes the above parameters can be applied to revise the ^{110}Cd g-factor measurement. The result (ignoring uncertainties in the average field strength) is $g(10^+) \approx -0.31(10)$, which is consistent with the expected value for a $\nu(h_{\frac{11}{2}^-})$ configuration.

8

^{111}Sn in gadolinium: g-factor measurement

8.1 Measurement

A final experiment was conducted to further test the limits of the LaBr_3 setup and the TDPAD method. The measurement used the same target as described in Section 7.1, however, an ^{16}O beam was used. The reaction was $^{98}\mathrm{Mo}(^{16}\mathrm{O},3\mathrm{n})^{111}\mathrm{Sn}$, which populates an $\frac{11}{2}^-$ isomer in ^{111}Sn, analogous to the isomer in ^{107}Cd. Both of these isomers are formed primarily by a single $\nu h_{\frac{11}{2}}$ neutron [Jer+92; Pra+84; Bre+74]. In contrast to the isomer in ^{107}Cd, the lifetime of the state in ^{111}Sn is short, $\tau = 13.3(15)$ ns [Bre+74]. This presents further challenges to the TDPAD method, as the fast decay of the state means oscillations will quickly be obscured by high statistical errors.

The g factor of the $\frac{11}{2}^-$ isomer has been measured once before as $g = -0.23(2)$ [Bre+74]. This experiment used an external field of 60.1 kG, resulting in a slower precession of 10.3(8) Mrad/s, with a period longer than the mean lifetime. In contrast, the implantation into gadolinium gives a field strength of $B_{hf} = -32.9(4)$ T [Kra83; GMM69], meaning an expected precession frequency of $\omega_L \approx 0.36$ Grad/s, or period of $T_L \approx 9$ ns. If this frequency can be resolved, it could potentially result in a more precise g-factor measurement.

As with the case of ^{107}Cd, an excitation function was measured. A beam energy of 58 MeV was decided on to maximize the excitation of ^{111}Sn whilst minimizing the 4n reaction channel.

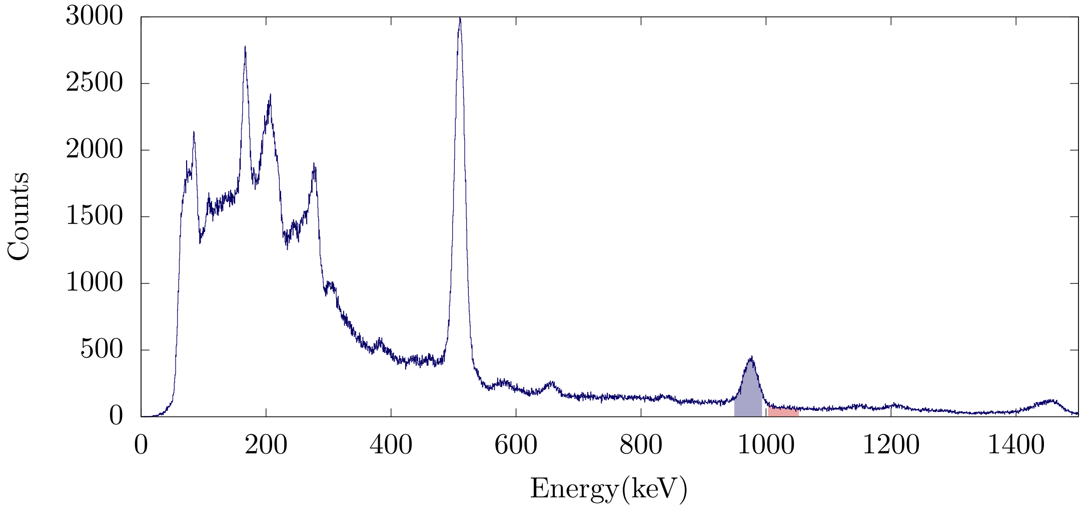

Figure 8.1: Energy spectrum showing the $\frac{11}{2}^-$ isomer in ^{111}Sn.

8.2 Results

The out-of-beam energy spectrum can be seen in Figure 8.1. The highlighted regions show the 978-keV peak which depopulates the $\frac{11}{2}^-$ isomer, and the relevant background subtraction region. The time spectra obtained can be seen in Figure 8.2. A lifetime curve has been fitted and $\tau = 12.7(1)$ ns obtained for the lifetime of the state. Other lifetime measurements for the state report $\tau = 13.3(15)$ ns [Bre+74], $\tau = 11(1)$ ns [Bri+72], $\tau = 14.4(7)$ ns [Pra+84]. The value obtained agrees with the weighted average $\tau = 13.3(3)$ of the literature values.

The ratio function is shown in Figure 8.3. A weak oscillation obscured by a significant amount of statistical fluctuation is present, however taking the autocorrelation over a longer time period (Figure 8.4) makes the oscillation clear. The Larmor frequency

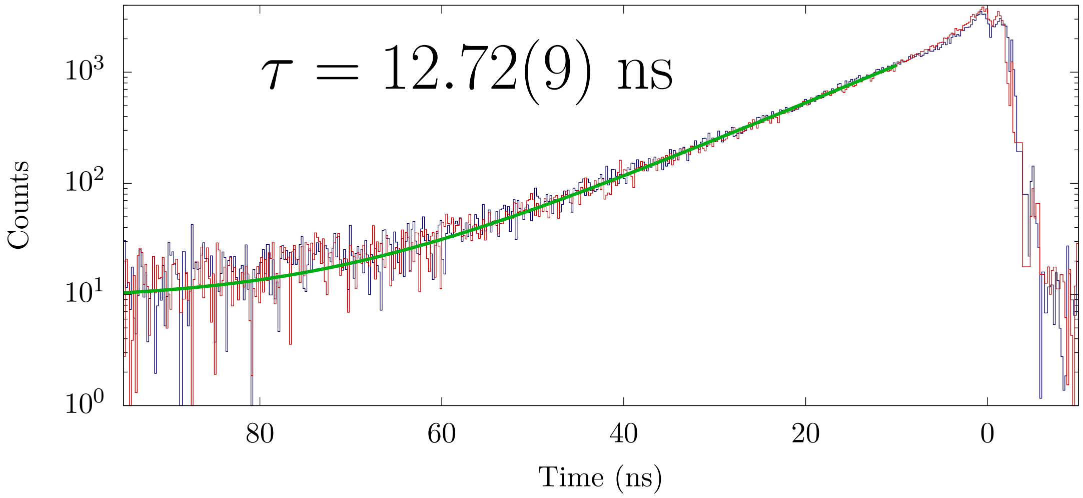

Figure 8.2: Time spectrum for the $\frac{11}{2}^-$ isomer in ^{111}Sn with fitted lifetime curve. Note the double prompt peak which indicates some sort of contamination.

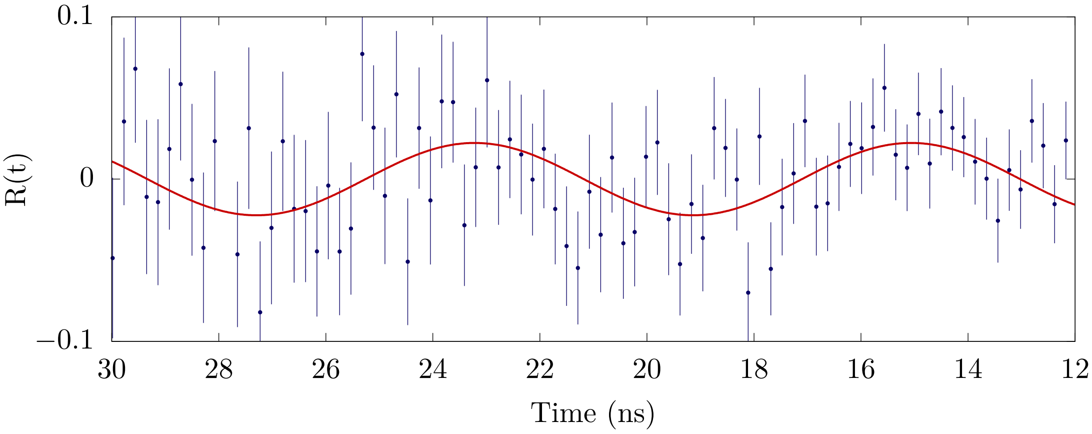

Figure 8.3: Ratio function for the $\frac{11}{2}^-$ isomer in ^{111}Sn showing weak oscillations.

$\omega_L = 0.40(1)$ Grad/s can be used with the hyperfine field strength of −32.9(4) T reported in [Kra83; GMM69] to determine the g factor. The field strength was measured at 4 K, which is close to the temperature used in the present work. We find $g(\frac{11}{2}^-) = -0.25(2)$, in agreement with the previous measurement of $g(\frac{11}{2}^-) = -0.23(2)$ [Bre+74].

8.3 Discussion

This measurement serves to further show the difficulties in aligning the TAC spectra. The transition used to accomplish the alignment in this case was the 1084-keV transition, from a 2062-keV state in ^{111}Sn. However, as can be seen in the in-beam energy spectrum (Figure 8.6), the higher energy state is not strongly excited. The time spectrum obtained for alignment (Figure 8.7) also reflects this – low counts meaning that centroid of the distribution is difficult to determine precisely. Moreover, any contaminants that may be present would be impossible to resolve and isolate because of the low statistics. The case of ^{107}Cd (see Figure 7.6) shows that this can be important.

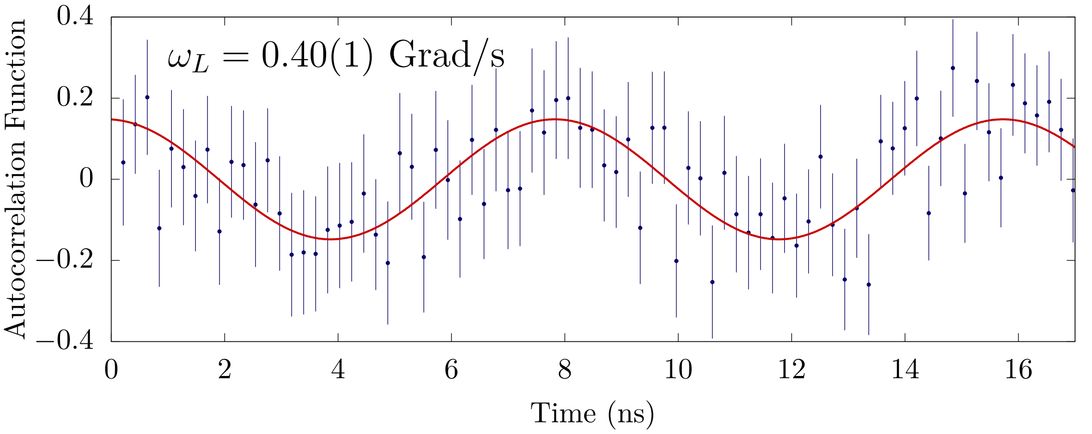

Figure 8.4: Autocorrelation function for the $\frac{11}{2}^-$ isomer in ^{111}Sn making the precessions in Figure 8.3 clear.

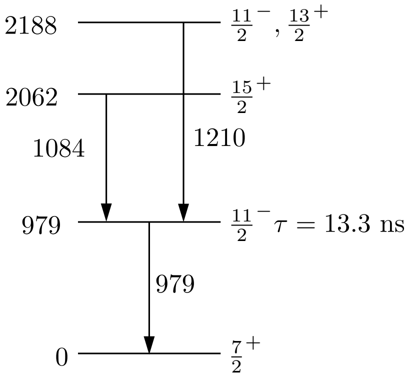
2188
2062
1084
979
0
1210
979
$\frac{11}{2}^-$, $\frac{13}{2}^+$
$\frac{15}{2}^+$
$\frac{11}{2}^-$ $\tau = 13.3$ ns
$\frac{7}{2}^+$

Figure 8.5: Partial decay scheme of ^{111}Sn, showing the isomeric $\frac{11}{2}^-$ state as well as the prompt 1084-keV transition used to align the spectra.

Especially as time scales decrease, the ability to precisely align the detectors becomes not only more important, but also more difficult. If the time required to form a "good" alignment spectrum is on the same order as the time-scales on which the beam pulse is drifting, good alignment becomes impossible. With the current experimental arrangement, this limit has been reached in the case of ^{111}Sn. As a result of the difficulties encountered in the alignment process, the precession is only clear for a few oscillations and consequently the precision of the g-factor measurement is lower than would be ideal. In future it will be necessary to develop a method of detecting the beam pulse arrival time with greater accuracy, particularly when pulsed beams of sub-nanosecond duration become available at the Heavy Ion Accelerator Facility.

The g factors of the $\nu(h_{\frac{11}{2}})$ states in Cd and Sn are shown in Table 8.1. It can be seen clearly in the case of Cd that about the $N = 64$ sub-shell closure ($A = 112$) the magnitude of the g factors reaches a maximum, with g factors falling off on either side. Observing

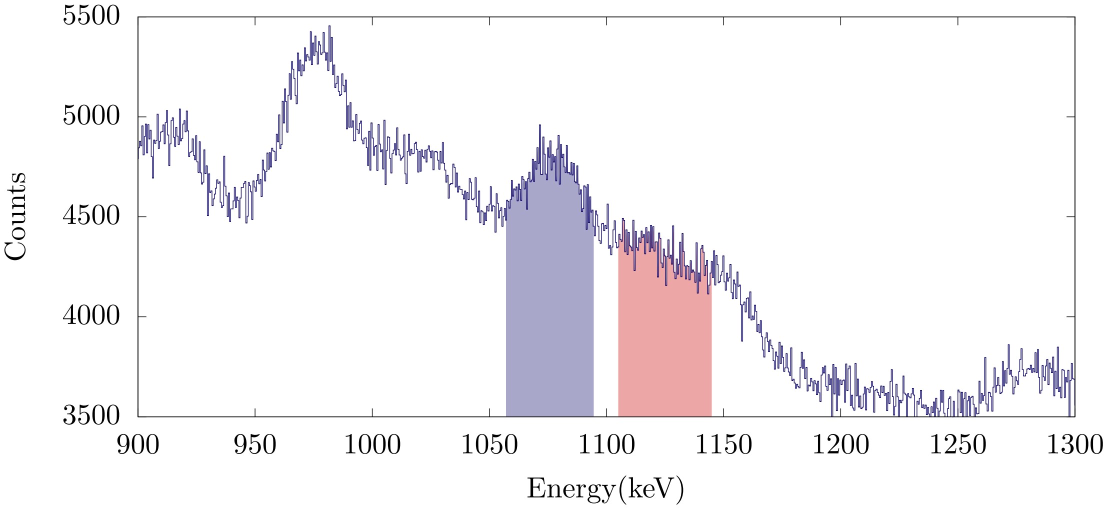

Figure 8.6: In beam energy spectrum from an LaBr$_3$ detector showing the 1084-keV transition in ^{111}Sn used to align the spectra from different detectors.

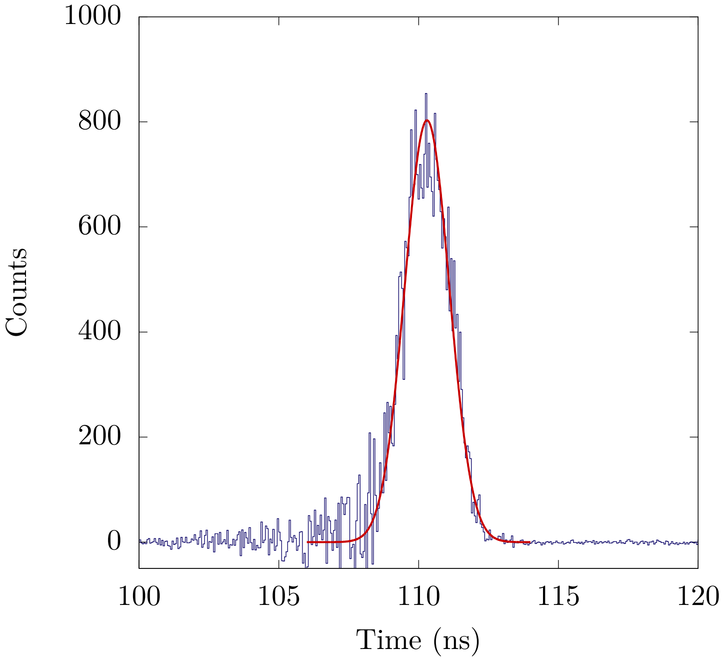

Figure 8.7: An example of a spectrum that was used to determine the position of the beam pulse. Note the low statistics, especially in comparison to Figures 6.12 and 7.6.

such trends often lead to deeper understanding of the structure of the nucleus [Yor+13; Yor+16]. Unfortunately, the g-factor measurements for Sn around the sub-shell closure ($A = 114$) are not precise enough to provide such insight. Clearly a better measurement of $g(\frac{11}{2}^-)$ for ^{111}Sn would be helpful here. Although it was not achieved here, the g-factor measurement made is consistent with the previous work [Bre+74]. The success of the measurement despite the difficulties encountered shows the applications of LaBr$_3$ detectors to determining g factors of shorter lived states with the TDPAD technique, and that a more precise measurement on ^{111}Sn may be achieved in the future.

A	g(Cd)	g(Sn)	References
107	−0.189(2)		[Ber+74; Rag89]
109	−0.1993(4)		[Sto05]
111	−0.20093(7)	−0.23(2)	[LM69; Sto05; Bre+74]
113	−0.1977789(4)	−0.235(4)	[CM69; Sto05; Bre+74]
115	−0.1892789(3)	−0.251(2)	[CM69; Sto05]
117	−0.1814(7)	−0.2537(2)	[Yor+13; Ans+86]
119	−0.1753(5)	−0.255(15)	[Yor+13; Gum+72]
121	−0.1836(7)	−0.2523(2)	[Yor+13; Ans+86]
123	−0.1821(5)	−0.2491(2)	[Yor+13; Ans+86]

Table 8.1: A comparison of magnetic moments for analogous $h_{\frac{11}{2}^-}$ states in the odd Cd and Sn isotopes.

9

Conclusion

The application of $LaBr_3$ detectors to the TDPAD technique has been achieved in five separate cases, covering a variety of situations and their associated challenges. Results for the slowly precessing ^{69}Ge and ^{67}Ge isomers show the effectiveness of the setup with strong agreement with past measurements [LRR91]. The observation of the precessions also allows a measurement of the hyperfine field of Ge in iron at low temperatures to be made for the first time and with high precision.

The measurement of the 10^+ state in ^{54}Fe shows that $LaBr_3$ scintillators are capable of resolving very fast precessions on the order of ~ 1 ns in-beam. Moreover, the limiting factor is not the $LaBr_3$ detectors themselves but rather the beam pulsing resolution and stability.

The successful measurement of the precession in ^{107}Cd shows the application of the in-beam TDPAD technique to examining the magnetic structure after the implantation process. The case studied allows the resolution of the discrepancy between the $g(10^+)$ measurement in ^{110}Cd [RSA95] compared with $g(\frac{11}{2}^-)$ measurements in neighbouring nuclei. Thus it appears that the first 10^+ state in ^{110}Cd is formed by the maximal coupling of a pair of $h_{\frac{11}{2}}$ neutrons $(10 = \frac{11}{2} + \frac{9}{2})$, and that the nucleus retains an essentially spherical shape. Insight into both the strength of the magnetic hyperfine field, and also its distribution across different implantation sites, was gained. Whilst the observed average field strength is close to that obtained in previous measurements, approximately half of the implanted Cd nuclei reside on effectively field-free sites.

The ^{111}Sn experiment makes a further application of this methodology. A measurement of a much shorter-lived state was possible because of the fast frequencies that can now be resolved. Once again, this experiment makes it clear that the limitations of the current system are not the detectors used, but rather the beam pulsing and its temporal stability.

The drift of the beam pulse with respect to the RF signal that drives the pulsing system is a serious consideration that must be accounted for. Especially as the time-scale of the pulsing system becomes shorter, as planned by the installation of a picosecond buncher, this becomes increasingly significant. Moreover, it becomes increasingly difficult to adjust for the beam drift effectively as lifetimes and precession periods decrease. Developments which make this process more accurate would further increase the scope of TDPAD methods. The ANU group is evaluating alternative pulse-detection systems to enable timing off the beam pulse arrival at the target chamber instead of the RF buncher.

The use of gadolinium hosts has experimental advantages for TDPAD measurements of the type investigated here. However, the measurement of Cd in gadolinium clearly showed evidence of a complex hyperfine magnetic field distribution after implantation. It is evident that further investigations of the distributions of hyperfine fields following implantation into magnetized gadolinium are needed before they can be used routinely for g-factor measurements.

Appendices

A

Autocorrelation Functions

As defined in 5.3, the auto correlation function is

$$X(\tau) = \lim_{T\to\infty} \frac{1}{T} \int\limits_0^T f(t)f(t+\tau)dt. \tag{A.1}$$

Using the angle addition formulae for trigonometric functions

$$\cos(\alpha+\beta) = \cos(\alpha)\cos(\beta) - \sin(\alpha)\sin(\beta) \tag{A.2}$$
$$\sin(\alpha+\beta) = \cos(\alpha)\sin(\beta) + \cos(\beta)\sin(\alpha), \tag{A.3}$$

it can be shown that for a pure harmonic function, $f(t) = \cos(t)$, that the autocorrelation function is also a pure cosine curve.

$$
\begin{aligned}
X(\tau) &= \lim_{T\to\infty} \frac{1}{T} \int_0^T \cos(t)\cos(t+\tau)dt && \text{(A.4)}\\
&= \lim_{T\to\infty} \frac{1}{T} \int_0^T \cos(t)(\cos(t)\cos(\tau) - \sin(t)\sin(\tau))dt && \text{(A.5)}\\
&= \lim_{T\to\infty} \frac{1}{T} \left[\cos(\tau)\int_0^T \cos(t)^2 dt - \sin(\tau)\int_0^T \sin(t)\cos(t)dt\right] && \text{(A.6)}\\
&= \frac{1}{2}\lim_{T\to\infty} \frac{1}{T} \left[\cos(\tau)(T+\cos(T)\sin(T)) - \sin(\tau)\sin(T)^2\right] && \text{(A.7)}\\
&= \frac{1}{2}\lim_{T\to\infty} \cos(\tau)(1+\frac{\cos(T)\sin(T)}{T}) - \sin(\tau)\frac{\sin(T)^2}{T} && \text{(A.8)}\\
&= \frac{1}{2}\cos(\tau). && \text{(A.9)}
\end{aligned}
$$

The above shows that the autocorrelation gives the same cosine curve, up to a normalization factor. This can be easily extended to a more general cosine curve $f(t) = a\cos(bt+c)$, and by carrying out the substitution $t' = bt + c$, it is noted that

$$X(\tau) = \frac{a^2}{2}\cos(b\tau), \tag{A.10}$$

once again a pure cosine with the same frequency, up to a normalization factor. Now consider a function composed of an arbitrary number of harmonic components, $f_i(t) = a_i\cos(b_i t+c_i)$, each with distinct frequencies, i.e. $b_i \neq b_j$ for $i \neq j$. Then

$$
\begin{aligned}
f(t) &= \sum_{i=1}^{\infty} a_i\cos(b_i t + c_i) && \text{(A.11)}\\
&= \sum_{i=1}^{\infty} f_i(t), && \text{(A.12)}
\end{aligned}
$$

and the autocorrelation function is given by:

$$
\begin{aligned}
X(\tau) &= \lim_{T\to\infty} \frac{1}{T} \int_0^T \sum_{i,j=1}^{\infty} a_i a_j \cos(b_i t + c_i)\cos(b_j t + c_j + b_j\tau)dt && \text{(A.13)}\\
&= \sum_{i,j=1}^{\infty} a_i a_j \lim_{T\to\infty}\frac{1}{T}\left[\cos(b_j\tau)\int_0^T \cos(b_i t c_i)\cos(b_j t + c_j)dt\right. && \text{(A.14)}\\
&\qquad \left. - \sin(b_j\tau)\int_0^T \sin(b_i t + c_i)\cos(b_j t + c_j)dt\right].
\end{aligned}
$$

Noting that for $i \neq j$, the limits of the integrals become:

$$\lim_{T\to\infty} \frac{1}{T} \int_0^T \cos(b_i t + c_i)\cos(b_j t + c_j)dt = 0 \tag{A.15}$$
$$\lim_{T\to\infty} \frac{1}{T} \int_0^T \sin(b_i t + c_i)\cos(b_j t + c_j)dt = 0.$$

Thus all terms in the sum except for $i = j$ vanish, giving:

$$X(\tau) = \sum_{i=1}^{\infty} \lim_{T\to\infty} \frac{1}{T} \int_0^T f_i(t) f_i(t+\tau)dt \tag{A.16}$$
$$= \sum_{i=1}^{\infty} \frac{a_i^2}{2} \cos(b_i \tau), \tag{A.17}$$

Thus, the autocorrelation obtained is a weighted sum of the original frequencies present, with all phase information lost.

A.1 Discrete autocorrelation function

The discrete version of the autocorrelation function shown in Equation 5.4 is found by restricting the limit to a finite value (considering there are only a finite number of channels in the histogram data), and normalizing to the value of the autocorrelation at $\tau = 0$, so that the autocorrelation function of a pure harmonic signal has an amplitude of 1.

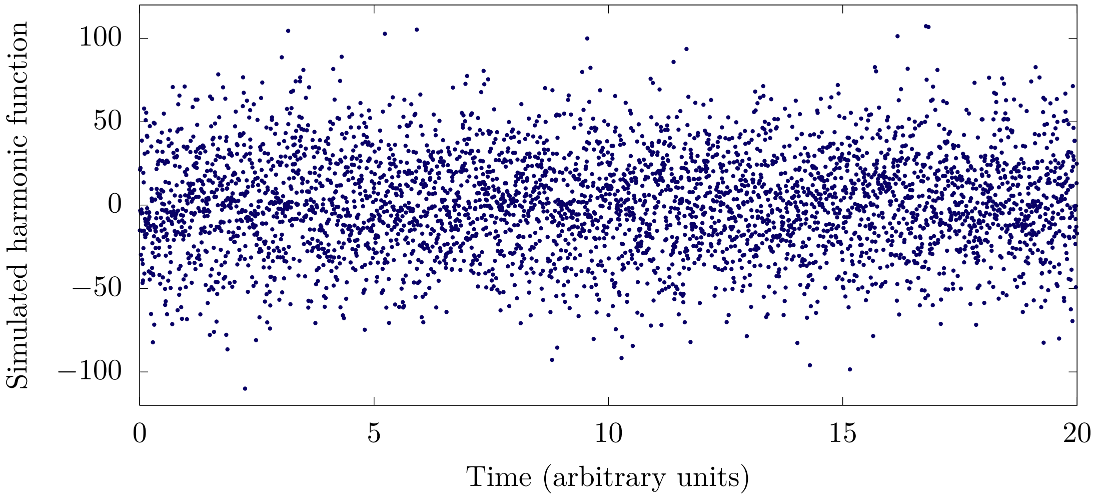

Figure A.1: The simulated data is a cos(x) curve with Gaussian noise added. The standard deviation of the noise is 6 times the amplitude of the cosine curve, obscuring the oscillation completely.

$$X(\tau) = \lim_{T\to\infty} \frac{1}{T} \int_0^T f(t)f(t+\tau)dt \tag{A.18}$$

$$\approx \frac{1}{T_{max} - T_{min}} \int_{T_{min}}^{T_{max}} f(t)f(t+\tau)dt \tag{A.19}$$

$$X(n) \approx \frac{1}{T_{max} - T_{min}} \sum_{k=T_{min}}^{T_{max}} x_k x_{k+n} \tag{A.20}$$

$$= \sum_{k=k_1}^{k_2-n} \frac{x_k x_{k+n}}{k_2 - k_1 - n + 1}, \tag{A.21}$$

$$\tag{A.22}$$

where the channel numbers k_1 and k_2 correspond to the values T_{min} and T_{max}. The normalization factor is given by

$$X(0) = \sum_{k=k_1}^{k_2} \frac{x_k^2}{k_2 - k_1 + 1}, \tag{A.23}$$

which gives the form in equation 5.4.

A.2 Autocorrelation simulations

To establish the accuracy and effectiveness of this technique, finding the autocorrelation functions of simulated data can be informative. Consider Figure A.1, a cosine curve with

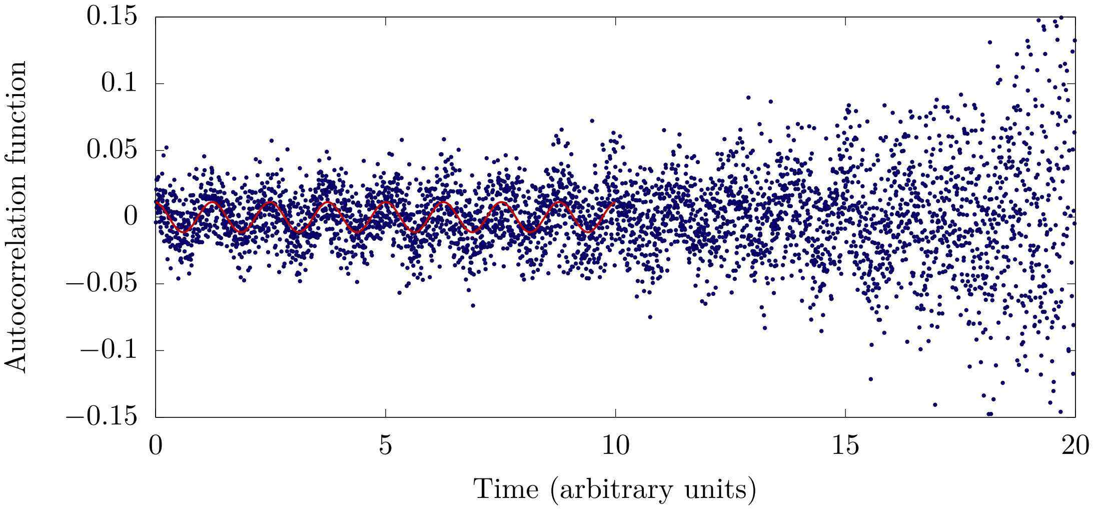

Figure A.2: The data set shown in Figure A.1, when analysed using an autocorrelation function shows a single frequency oscillation. The fitted curve finds the frequency to be the same as that used in the simulation.

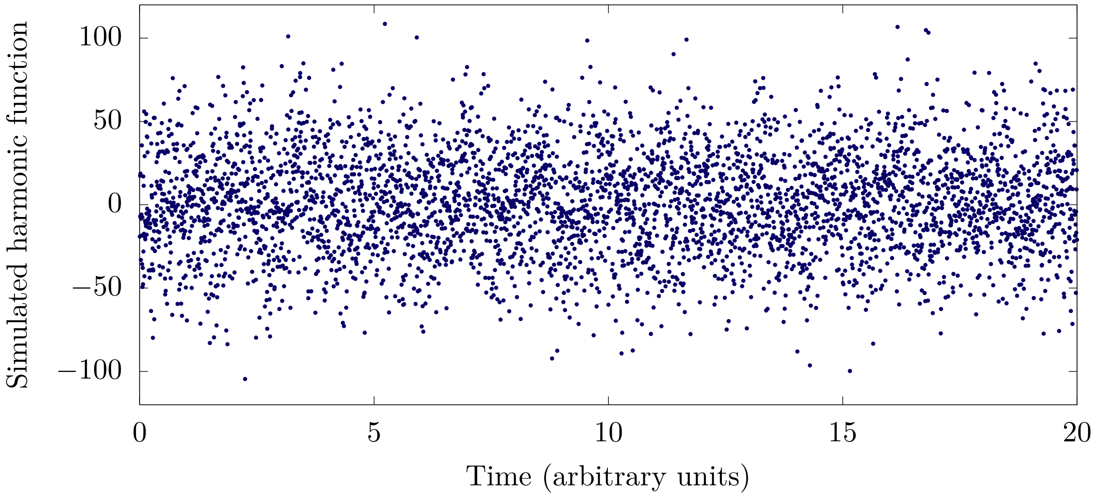

Figure A.3: Once again the noise completely obscures any oscillations in the data.

arbitrary phase, amplitude, and significant random (Gaussian) noise.

However, when the autocorrelation of the data is taken, a single oscillation of the correct frequency can be seen (Figure A.2).

The autocorrelation technique can also be tested on data with more than one frequency. Consider Figure A.3, the sum of two cosine components with different amplitudes, phases, and frequencies.

However, the autocorrelation function clearly shows two frequencies which go in and out of phase with each other. Note: initially they start in phase, regardless of their relative phases in the original data.

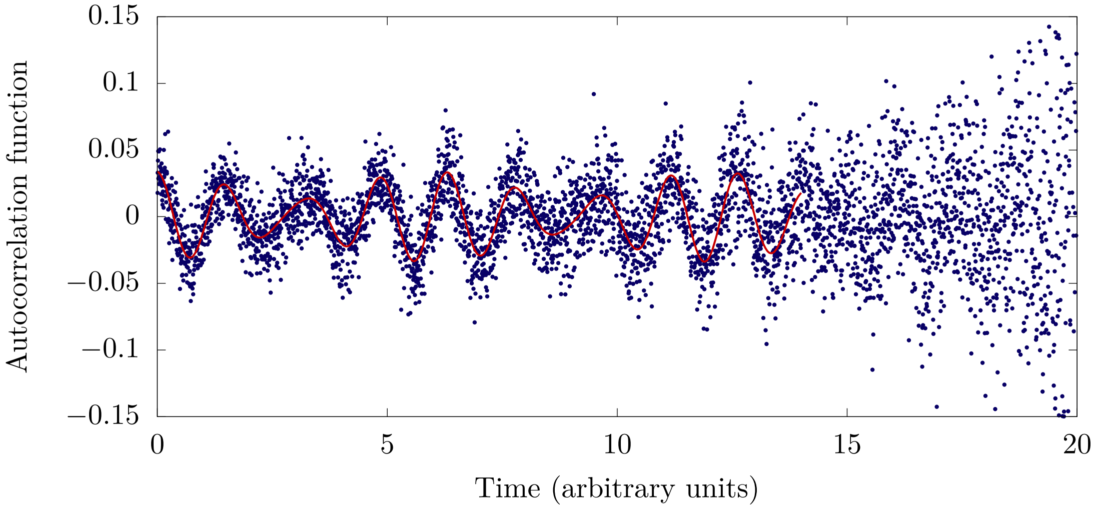

Figure A.4: The autocorrelation function reveals the two correct frequencies from the simulation.

B

Angular Momentum Algebra

B.1 Coupling two angular momenta and Clebsch-Gordan coefficients

Consider a system in which we have three angular momenta $\boldsymbol{j}, \boldsymbol{j_1}, \boldsymbol{j_2}$, coupled according to

$$\boldsymbol{j} = \boldsymbol{j_1} + \boldsymbol{j_2}. \tag{B.1}$$

One natural choice of basis states is the $|j_i, m_i\rangle$ representation that diagonalizes the $\hat{J}_i^2$ and $\hat{J}_{zi}$ operators, i.e.

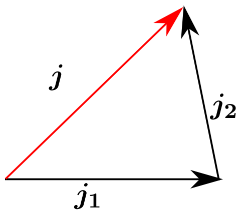

Figure B.1: The coupling of two angular momenta $\boldsymbol{j_1}$ and $\boldsymbol{j_2}$ to form $\boldsymbol{j}$

$$\hat{J}_1^2 \left| j_1, m_1 \right\rangle = j_1(j_1+1) \left| j_1, m_1 \right\rangle \qquad \hat{J}_2^2 \left| j_2, m_2 \right\rangle = j_2(j_2+1) \left| j_2, m_2 \right\rangle \tag{B.2}$$

$$\hat{J}_{z1} \left| j_1, m_1 \right\rangle = m_1 \left| j_1, m_1 \right\rangle \qquad \hat{J}_{z2} \left| j_2, m_2 \right\rangle = m_2 \left| j_2, m_2 \right\rangle . \tag{B.3}$$

However, it is often useful to work in a basis where $\hat{J}^2$ and $\hat{J}_z$ are diagonal. The $\hat{J}_1^2$ and $\hat{J}_2^2$ operators are also diagonal in this basis. The Clebsch-Gordan coefficients allow the transformation between these two sets of basis states:

$$\left| j, m, j_1, j_2 \right\rangle = \sum_{m_1, m_2} \left\langle j_1 m_1 j_2 m_2 | j m \right\rangle \left| j_1, m_1, j_2, m_2 \right\rangle . \tag{B.4}$$

The states on the right diagonalize the $\hat{J}_1^2, \hat{J}_2^2, \hat{J}_{z1}, \hat{J}_{z2}$ operators, and those on the left diagonalize second set: $\hat{J}^2, \hat{J}_z, \hat{J}_1^2, \hat{J}_2^2$. Note that the coupling requires $|j_1 - j_2| \leqslant j \leqslant |j_1 + j_2|$, and $m_1 + m_2 = m$, thus the Clebsch-Gordan coefficients vanish whenever this is not the case.

The Clebsch-Gordan coefficients have many useful symmetry and orthogonality relationships, which will not be stated here but are well known and documented [Ros57; Mes66; Sie66].

B.1.1 Wigner 3-j symbols

Sometimes the Wigner 3-j symbol is used instead of a Clebsch-Gordan coefficient. It is defined as the following:

$$\begin{pmatrix} j_1 & j_2 & j \\ m_1 & m_2 & m \end{pmatrix} = (-)^{j_1 - j_2 - m} \frac{1}{\sqrt{2j+1}} \left\langle j_1 m_1 j_2 m_2 | j - m \right\rangle . \tag{B.5}$$

These are equivalent to Clebsch-Gordan coefficients but have better symmetry relationships and can simplify the mathematics in some cases [Sie66; Mes66].

B.2 Coupling three angular momenta and Racah coefficients

Consider now a system which consists of the sum of three angular momentum components:

$$\boldsymbol{j} = \boldsymbol{j_1} + \boldsymbol{j_2} + \boldsymbol{j_3}. \tag{B.6}$$

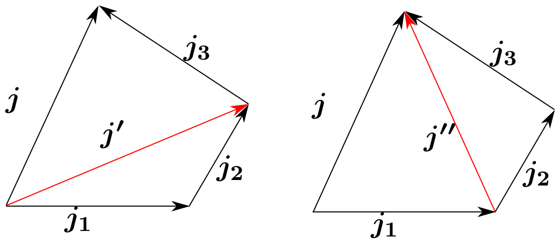

Figure B.2: Two coupling schemes are shown: on the left first coupling $\boldsymbol{j_1}$ and $\boldsymbol{j_2}$ to form $\boldsymbol{j'}$, then coupling $\boldsymbol{j'}$ and $\boldsymbol{j_3}$ to get $\boldsymbol{j}$. On the right the order is changed – $\boldsymbol{j_2}$ and $\boldsymbol{j_3}$ are coupled first to form $\boldsymbol{j''}$, before $\boldsymbol{j_1}$ and $\boldsymbol{j''}$ are coupled to get $\boldsymbol{j}$

There are several ways that this can be reduced to repeatedly coupling different pairs of angular momenta, and these are depicted pictorially in Figure B.2. As we would expect, the different coupling schemes lead to different bases that diagonalize different operators. Namely the first scheme (in B.2) diagonalizes $\hat{J}^2, \hat{J}_z, \hat{J}'^2, \hat{J}_1^2, \hat{J}_2^2$, and $\hat{J}_3^2$, whilst the second diagonalizes $\hat{J}^2, \hat{J}_z, \hat{J}''^2, \hat{J}_1^2, \hat{J}_2^2$, and $\hat{J}_3^2$.

The coefficients which allow the transformation between these bases are the Racah coefficients. It can be deduced that for the j' representation

$$|jmj'j_1j_2j_3\rangle = \sum_{\substack{m_1m_2\\m_3m'}} \langle j_1m_1j_2m_2|j'm'\rangle\,\langle j'm'j_3m_3|jm\rangle\,|j_1m_1j_2m_2j_3m_3\rangle\,, \tag{B.7}$$

and for the j'' representation

$$|jmj''j_1j_2j_3\rangle = \sum_{\substack{m_1m_2\\m_3m'}} \langle j_2m_2j_3m_3|j''m''\rangle\,\langle j_1m_1j''m''|jm\rangle\,|j_1m_1j_2m_2j_3m_3\rangle\,. \tag{B.8}$$

The transformation between the two is how the Racah coefficients $W(j_2j_1jj_3;j'j'')$ are defined:

$$\langle jmj'j_1j_2j_3|jmj''j_1j_2j_3\rangle = \sqrt{(2j'+1)(2j''+1)}W(j_2j_1jj_3;j'j''), \tag{B.9}$$

or equivalently:

$$|jmj'j_1j_2j_3\rangle = \sum_{j''} \sqrt{(2j_1+1)(2j_2+1)}W(j_2j_1jj_3;j'j'')\,|jmj''j_1j_2j_3\rangle\,. \tag{B.10}$$

Racah coefficients are closely linked to the Wigner 6-j symbols which are not defined here. These, and the relevant symmetry and orthogonality relations can be found in [Mes66; Ros57; Sie66]

Bibliography

[Ajz87] F. Ajzenberg-Selove. “Energy levels of light nuclei A = 18-20”. In: *Nuclear Physics A* 475.1 (1987), pp. 1–198.

[Akb15] A. Akber. *Fast $\gamma\gamma$ timing with LaBr$_3$ scintillators.* 2015.

[AlN+79] A. M. Al-Naser et al. “Decay scheme of excited states in ^{67}Ge”. In: *Journal of Physics G* 5.3 (1979), pp. 423–432.

[Ans+86] M. Anselment et al. “Charge radii and moments of tin nuclei by laser spectroscopy”. In: *Physical Review C* 34.3 (1986), pp. 1052–1059.

[Ber+73] H. Bertschat et al. “Magnetic Moments of Excited $\frac{9}{2}^+$ States Around A = 70, Experimental Values for ^{67}Zn and ^{67}Ge”. In: *International Conference of Nuclear Magnetic Moments and Nuclear Structure.* 1973.

[Ber+74] H. Bertschat et al. “Magnetic moment and half-life of the isomeric $\frac{11}{2}^-$ state in ^{107}Cd”. In: *Nuclear Physics A* 222 (1974), pp. 399–404.

[Bos+70] L. Bostrom et al. “Internal fields for Cd in gadolinium metal”. In: *Physics Letters A* 31A.8 (1970), pp. 436–437.

[Bos+71] L. Bostrom et al. “Hyperfine Interaction for a Cadmium Impurity in Gadolinium Metal”. In: *Physica Scripta* 3 (1971), pp. 175–181.

[Boz+78] E. Bozek et al. “Isomeric Level at 6528 keV in ^{54}Fe”. In: *International Conference on Medium-Light Nuclei.* 1978.

[Boz93] R. M. Bozorth. *Ferromagnetism.* Wiley, 1993.

[Bre+74] R. Brenn et al. “Electromagnetic properties of the $\frac{11}{2}^-$ states in ^{111}Sn and ^{113}Sn”. In: *Physical Review C* 10.4 (1974), pp. 1414–1421.

[Bri+72] H. F. Brinckmann et al. “Nuclear Isomers in ^{113}Sn, ^{111}Sn, ^{117}Te, and ^{115}Te”. In: *Nuclear Physics A* 193 (1972), pp. 236–246.

[Cer74] J. Cerny. *Nuclear Spectroscopy and Reactions.* Academic Press, 1974.

[Cha+00] C. Chandler et al. “Observation of isomeric states in neutron deficient $A \sim 80$ nuclei following the projectile fragmentation of ^{92}Mo”. In: *Physical Review C* 61.4 (2000), pp. 1–14.

[Chr+70] J. Christiansen et al. “Stroboscopic observation of nuclear larmor precession”. In: *Physical Review C* 1.2 (1970), pp. 613–618.

[Chr83] J. Christiansen. *Hyperfine Interactions of Radioactive Nuclei.* Topics in Current Physics. Springer Berlin Heidelberg, 1983.

[CM69] R. L. Chaney and M. N. Mcdermott. “Nuclear orientation of ^{113}Cd^m, ^{115}Cd, and ^{115}Cd^m”. In: *Physical Letters* 29.2 (1969), pp. 103–104.

[Coc+70] S. Cochavi et al. “$E2$ Transition Strengths Between $(1f_{7/2})^{\pm 2}$ States of Ca^{42}, Ti^{50}, and Fe^{54}”. In: *Physical Review C* 2.6 (1970), pp. 2241–2248.

[Cre+10] F. C. L. Crespi et al. “HPGe detectors timing using pulse shape analysis techniques”. In: *Nuclear Instruments and Methods in Physics Research A* 620.2-3 (2010), pp. 299–304.

[Daf+78] E. Dafni et al. “Static moments of ^{54}Fe^{m} and perturbed angular distributions with combined dipole and quadrupole interactions”. In: *Physics Letters B* 76.1 (1978), pp. 51–53.

[Dor+93] P. Dorenbos et al. “Absolute light yield measurements on BaF$_2$ crystals and the quantum efficiency of several photomultiplier tubes”. In: *IEEE Transactions on Nuclear Science* 40.4 pt 1 (1993), pp. 424–430.

[FH73] M. Forker and A. Hammesfahr. “The magnetic hyperfine field at Cd nuclei in the rare earth ferromagnets Gd, Tb, Dy, Ho, Er and Tm”. In: *Zeitschrift für Physik* 263.1 (1973), pp. 33–47.

[Fuj+83] M. Fujioka et al. “Nuclear level-crossing resonance of the 398 keV $\frac{9}{2}^{+}$ state of ^{69}Ge in a Zn single crystal”. In: *Hyperfine Interactions* 15/16 (1983), pp. 1017–1020.

[GE96] G. Y. Guo and H. Ebert. “First-principles study of the magnetic hyperfine field in Fe and Co multilayers.” In: *Physical Review B* 53.5 (1996), pp. 2492–2503.

[Geo01] G. Georgiev. “Magnetic Moments of Isomers and Ground States of Exotic Nuclei Produced by Projectile Fragmentation”. PhD thesis. Katholieke Universiteit Leuven, 2001.

[GMM69] V. Gotthardt, H. S. Miller, and R. L. Mossbauer. “Magnetic Field at ^{119}Sn in Gadolinium”. In: *Physical Letters* 28.7 (1969), pp. 480–481.

[Gum+72] D. F. Gumprecht et al. “A Mossbauer Observation of the Magnetic Moment of the 89 keV Excited State of ^{119}Sn”. In: *Physics Letters* 40 (1972), pp. 297–298.

[Hag+74] U. Hagemann et al. “Observation of isomeric states and band structures in ^{107}Cd”. In: *Nuclear Physics A* 228 (1974), pp. 112–124.

[Ham75] W. D. Hamilton. *The Electromagnetic Interaction in Nuclear Spectroscopy.* North-Holland Publishing Company, 1975.

[Har+01] S. Harissopulos et al. “Picosecond lifetime measurements in ^{109}Cd and ^{110}Cd”. In: *Nuclear Physics A* 683 (2001), pp. 157–181.

[Has+84] M. Hass et al. “Nuclear polarization of high-spin levels and the sign of the quadrupole moment of ^{54}Fe(10^{+})”. In: *Nuclear Physics A* 414 (1984), pp. 316–332.

[Hen+71] R. Hensler et al. “Mean Lifetime and Magnetic Moment of the 2.95-MeV (6^{+}) State of ^{54}Fe”. In: *Physical Review Letters* 27.23 (1971), pp. 1587–1590.

[HLM88] I. Holl, E. Lorenz, and G. Mageras. “Measurement of the Light Yield of Common Inorganic Scintillators.” In: *IEEE Transactions on Nuclear Science* 35.1 (1988).

[Ilt+06] A. Iltis et al. “Lanthanum halide scintillators: Properties and applications”. In: *Nuclear Instruments and Methods in Physics Research A* 563.2 (2006), pp. 359–363.

[Jer+92] D. Jerrestam et al. “Rotational bands in ^{107}Cd”. In: *Nuclear Physics A* 545 (1992), pp. 835–853.

[Juu+94] S. Juutinen et al. “Gamma-ray spectrosopy of ^{110}Cd”. In: *Nuclear Physics A* 573 (1994), pp. 306–332.

[KAK98] L. K. Kostov, W. Andrejtscheff, and L. G. Kostova. “Absolute E1 and E2 transition rates in ^{110}Cd”. In: *The European Physical Journal A* 273 (1998), pp. 269–273.

[KM86] C. Kittel and P. McEuen. *Introduction to solid state physics.* Vol. 8. 1986.

[Kno00] G. F. Knoll. *Radiation Detection and Measurement.* 2000.

[Kra83] K. S. Krane. “Dilute impurity hyperfine fields in Fe, Co, Ni, Gd”. In: *Hyperfine Interactions* 15/16 (1983), pp. 1069–1080.

[Kra88] K. S. Krane. *Introductory Nuclear Physics.* John Wiley and Sons, Inc., 1988.

[Lav+83] M. Laval et al. “Barium fluoride - Inorganic scintillator for subnanosecond timing”. In: *Nuclear Instruments and Methods In Physics Research* 206.1-2 (1983), pp. 169–176.

[Law80] R. D. Lawson. *Theory of the nuclear shell model.* Oxford Studies in Nuclear Physics Series. Clarendon Press, 1980.

[Lee88] C.-S. Lee. “A Study of Spin Density Oscillation of Conduction Electrons in $\mathrm{Fe}_{1-x}\mathrm{Ge}_x$ Alloys using TDPAD Technique”. PhD thesis. Rutgers, The State University of New Jersey, 1988.

[Les+05] J. Leske et al. “Nuclear structure of the first 2^+ state in radioactive ^{68}Ge based on g factor and lifetime measurements”. In: *Physical Review C* 71.4 (2005), p. 044316.

[LM69] N. S. Laulainen and M. N. McDermott. “Spin and Nuclear Moments of 55-min ^{105}Cd and 49-min^{111m}Cd”. In: *Physical Review* 177 (1969), pp. 1615–1623.

[LRR91] C. S. Lee, P. Raghavan, and R. S. Raghavan. “In-beam study of spin density oscillations in ferromagnetic Fe-based alloys using ^{67,69}Ge isomers”. In: *Nuclear Instruments and Methods in Physics Research B* 56/57 (1991), pp. 851–854.

[Lüt+12] R. Lüttke et al. “Collectivity in ^{66}Ge and ^{68}Ge via lifetime measurements”. In: *Physical Review C* 85.1 (2012), p. 017301.

[Mar58] W. Marshall. “Orientation of Nuclei in Ferromagnets”. In: *Physical Review* 110.6 (1958), pp. 1280–1285.

[MBP07] L. C. Mihailescu, C. Borcea, and A. J. M. Plompen. “Data acquisition with a fast digitizer for large volume HPGe detectors”. In: *Nuclear Instruments and Methods in Physics Research A* 578.1 (2007), pp. 298–305.

[Mes66] A. Messiah. *Quantum Mechanics.* North-Holland Publishing Company, 1966.

[Mos+97] M. Moszyński et al. “Absolute light output of scintillators”. In: *IEEE Transactions on Nuclear Science* 44.3 PART 1 (1997), pp. 1052–1061.

[MY76] H. Morinaga and T. Yamazaki. *In-beam gamma-ray spectroscopy.* North-Holland Publishing Company, 1976.

[Nak+78] S. Nakayama et al. “Effective Coupling Constants for M1, M2 and E3 Transitions in f-p Shell Nuclei”. In: *Journal of the Physical Society of Japan* 45.3 (1978), pp. 740–748.

[NBH97] V. Nanal, B. B. Back, and D. J. Hofman. “Temperature dependence of BaF_2 scintillation”. In: *Nuclear Instruments and Methods in Physics Research A* 389 (1997), pp. 369–378.

[Pii+93] M. Piiparinen et al. “Lifetimes of yrast states in ^{110}Cd”. In: *Nuclear Physics A* 565.3 (1993), pp. 671–686.

[PK82] T. Paradellis and C. A. Kalfas. “Excited states in ^{68}Ge and ^{69}Ge studied by the ^{64}Zn (^{7}Li, $pxn\gamma$) reaction”. In: *Physical Review C* 25.1 (1982), pp. 350–357.

[Pra+84] H. Prade et al. “New positive-parity states and the shell-model description of ^{111}Sn”. In: *Nuclear Physics A* 425 (1984), pp. 317–344.

[QMO69] A. A. Quaranta, M. Martini, and G. Ottaviani. “The pulse shape and the timing problem in solid state detectors – a review paper”. In: *IEEE Transactions on Nuclear Science* 16.2 (1969), pp. 35–61.

[Raf+83] M. H. Rafailovich et al. “Magnetic moment of the ^{54}Fe(10^+) level”. In: *Physical Review C* 27.2 (1983), pp. 602–605.

[Rag89] P. Raghavan. “Table of nuclear moments”. In: *Atomic Data and Nuclear Data Tables* 42.2 (1989), pp. 189–291.

[Ros57] M. E. Rose. *Elementary Theory of Angular Momentum.* John Wiley and Sons, Inc., 1957.

[RSA95] P. H. Regan, A. E. Stuchbery, and S. S. Anderssen. “Measurement of the g-factor of the yrast 10^+ state in 110Cd”. In: *Nuclear Physics A* 591.3 (1995), pp. 533–547.

[RSR77] P. Raghavan, M. Senba, and R. S. Raghavan. “Temperature Anomalies of Hyperfine Fields of s-p Impurity Elements in Cobalt”. In: *Physical Review Letters* 24 (1977), pp. 3–6.

[RSR78] P. Raghavan, M. Senba, and R. S. Raghavan. “Hyperfine magnetic fields at ^{67}Ge in Fe, Co, and Ni”. In: *Hyperfine Interactions* 4 (1978), pp. 330–337.

[Sie66] K. Siegbahn. *Alpha-, Beta-, and Gamma-Ray Spectroscopy.* North-Holland Publishing Company, 1966.

[SNY71] H. Saito, T. Nomura, and T. Yamazaki. “The Lifetime of the Lowest 6^+ State in ^{54}Fe and E2 Effective Charge”. In: *Journal of the Physical Society of Japan* 30.5 (1971), pp. 1252–1260.

[SR02] A. E. Stuchbery and M. P. Robinson. “Perturbed γ–γ correlations from oriented nuclei and static moment measurements I : formalism and principles”. In: *Nuclear Instruments and Methods in Physics Research A* 485 (2002), pp. 753–767.

[Sto05] N. J. Stone. “Table of nuclear magnetic dipole and electric quadrupole moments”. In: *Atomic Data and Nuclear Data Tables* 90.1 (2005), pp. 75–176.

[Str+78] D. C. Stromswold et al. “Parity determinations in $^{105-109}$Cd from linearly polarized gamma rays following (^{16}O,xn) reactions”. In: *Physical Review C* 17.1 (1978), pp. 143–154.

[Stu+05] A. E. Stuchbery et al. *Temperature sensitivity of hyperfine fields for terbium and gadolinium hosts.* 2005.

[Til+88] D. R. Tilley et al. “Energy levels of light nuclei, A = 20”. In: *Nuclear Physics A* 848.1–2 (1988), p. 1.

[Val+93] J. D. Valentine et al. “Temperature dependence of CsI(Tl) gamma-ray excited scintillation characteristics”. In: *Nuclear Instruments and Methods in Physics Research A* 325.1-2 (1993), pp. 147–157.

[Yor+13] D. T. Yordanov et al. “Spins, electromagnetic moments, and isomers of Cd$^{107-129}$”. In: *Physical Review Letters* 110 (2013), p. 192501.

[Yor+16] D. T. Yordanov et al. “Simple Nuclear Structure in 111-129Cd from Atomic Isomer Shifts”. In: *Physical Review Letters* 116.3 (2016), pp. 1–5.